Rydberg-Atom Electrometry for DC Field Mapping and Non-Invasive Electron Beam Diagnostics

Robert Behary

Meadow Lands, Pennsylvania

Master of Science, William and Mary, 2022
Bachelor of Science, Duquesne University, 2020

A Dissertation presented to the Graduate Faculty of
The College of William and Mary in Virginia in Candidacy for the Degree of
Doctor of Philosophy

Department of Physics

The College of William and Mary in Virginia
May 2026

APPROVAL PAGE

This Dissertation is submitted in partial fulfillment of
the requirements for the degree of

Doctor of Philosophy

Robert Behary

Approved by the Committee, March 2026

Committee Chair
Dr. Irina Novikova, Professor, Physics
College of William & Mary

Dr. Eugeniy E. Mikhailov, Professor, Physics
College of William & Mary

Dr. Seth Aubin, Associate Professor, Physics
College of William & Mary

Dr. Todd Averett, Professor, Physics
College of William & Mary

Dr. Shukui Zhang, Accelerator Division
Jefferson Lab

ABSTRACT

Rydberg atoms are a rapidly developing platform for rf and dc-electric field sensing. This dissertation focuses on work related to expanding the capability of Rydberg atom-based sensors to measuring spatially varying dc-electric fields and advancing static electric field vector electrometry. Previous field measurements relied on readout of optically prepared two-photon resonances and had limited spatial resolution. We developed transmission and fluorescence-based detection methods to measure spatially varying electric fields. We use these methods to perform non-disruptive, SI-traceable diagnostics of an electron beam. We also performed preliminary experiments for polarization-dependent vector electrometry designed to measure the field distribution of the electron beam. In addition to electron beam experiments, we also explored a novel readout of Rydberg resonances using an all-optical Ramsey interrogation to improve electric field measurement sensitivity.

TABLE OF CONTENTS

ACKNOWLEDGMENTS

I want to start by thanking my amazing advisor Irina Novikova. Thank you so much for everything that you do. From helping me understand things in the lab, creating wonderful outreach events for the community I can only hope I contributed to, and always trusting the five paper plan. You have helped push and shape me into the scientist that I am today, and hope that during my career I can mimic a fraction of your mentoring and scientific ability.

Flashing back, I would like to thank everyone who encouraged along this journey. From the start I would like to acknowledge my high school physics teacher Patrick Campbell, who showed me through example what it means to be encouraging, accepting, and how to create fun collaborative environments, your memory lives on.

Throughout my time, I have also been surrounded by some of the best and most helpful mentors I could ever ask for. Thank you so much for giving me the building blocks for all of this at Duquesne Dr. Benmokhtar, Dr. C, Coop, Daryl, Dr. Huster, and Dr. Frittelli. To my co-advisor Eugeniy, the only person I know laughs more than me, thanks for the help in lab and always laughing at my jokes even if you didn't get them.

Thank you so much to my other committee members; Seth for all the help in many ways especially in the machine shop, Shukui for keeping me tied in my Jlab roots, and Todd for helping during one of the most eventful days during the PhD.

To the lab crew, you all were the best partners I could ever dream of being in the trenches with. You all could be first author on this dissertation. Thank you those who were here at the end Nic, Mish, Nehal, Summrah, Will, Owen, Kalea, Zach, Matt, Bradley, and Ben, and those who were a part of the journey but continued on their amazing career paths Charris, Ziqi, Savannah, Alex, Sophia, Kevin, Jasmine, Jennifer, Jiahui, Paola, Ramisa, Mario, and the builder of my electron beam apparatus Saeed. Also to the greater physics and William & Mary graduate community, thanks especially to the Secret Climbing Club Ben, Noah, Paul, Will, and the Jlab postdocs Pia and Peter for delightful distractions, and sometimes even a little exercise. To Sarah for making an amazing cover page, and all the friends I've made along the way Reg, Randy, Canyon, Connor, and Collin. To my cohort who went through it all during our time here it's been a blast.

Finally thank you so much to my family for all the support throughout my time here. I know I get lost in the work, but thanks for always taking the time to call to say hello, make me laugh, and for the continued support throughout the whole process.

For my parents and Connor.

LIST OF TABLES

LIST OF FIGURES

Chapter 1

Introduction

1.1 Why study electric fields?

Measurements of electric fields and electric potential play a critical role across a wide range of scientific and industrial applications, because they provide direct insight into how charges and currents behave in physical systems. For example, in accelerator science, electromagnetic fields are used to accelerate charged particles (electrons, protons, or ions) to high energies. This process depends on precise control of both the magnitude and spatial distribution of these fields. Devices such as rf cavities and magnetic quadrupoles are designed to generate electromagnetic environments, and their performance requires millimeter-scale precision to ensure stable and accurate beam steering and focusing [5, 6]. At the same time, the particle beams (collections of moving charges) themselves generate electromagnetic fields which can interact with external fields and influence overall system behavior [7, 8].

Similarly, plasma physics investigates systems composed of energetic, ionized particles, in which collective electromagnetic interactions dominate system dynamics [9–11]. Understanding how charges move and organize within a plasma is essential for applications such as controlled nuclear fusion, where maintaining confinement and stability is a major challenge.

These environments are often extreme, in which temperatures are comparable to or exceeding those found on the surface of the sun, which destroy diagnostic tools. As a result, these applications require sensors capable of accurately measuring electric fields under harsh conditions without degrading or perturbing the system [12–15].

Beyond fundamental research applications, electromagnetic field measurements are also critical in industrial contexts. Engineers rely on field probes to monitor circuit performance and characterize the behavior of microwave and radio-frequency antennas [16–18]. These measurements enable optimization of device performance and ensure compliance with design specifications. Underpinning all of these applications is the fundamental principle that Maxwell's equations uniquely connect electric fields to their underlying charge and current distributions to understand complex physical systems [19].

Classical sensors typically infer electric fields rather than measuring them directly. Antennas, which measure oscillating rf fields [20, 21], convert intercepted radiation into current via oscillating charges within the antenna hardware. For static dc fields, Josephson junctions serve as the standard for measuring electric potential to infer the field [22, 23]. Here, the measurable signal is again a current generated within the superconducting junction. Both methods rely on proxy quantities to measure the field. A further drawback involves the electrostatic boundary conditions at the probe surfaces, which perturb the very fields they intend to measure. This interference disrupts the local charge distribution and introduces systematic measurement errors.

These limitations motivate the development of sensors capable of non-invasive, direct electric field measurements. Atomic sensors offer a promising platform because atomic properties are immutable and universal, eliminating the manufacturing variances, calibration, or degradation common in classical probes. These atomic sensors enable high-precision measurements of electric and magnetic fields [24, 25] and form the foundation of this dissertation. We present work utilizing Rydberg states of alkali-metal atoms to directly measure electric fields produced by an electron beam and to characterize dc electric field vectors.

1.2 Properties of Rydberg atoms for electric field sensing

Rydberg states of alkali-metal atoms, such as rubidium and cesium, are excitations in which the valence electron occupies a high principal quantum number state ($n > 10$) [1]. "Rydberg atoms" are named after Johannes Rydberg, who also described the discrete energy levels of hydrogen with the Rydberg formula:

$$E_n = -\frac{hcR_\infty}{n^2} = -\frac{1}{n^2}\frac{m_e e^4}{8\varepsilon_0 h^2}, \tag{1.1}$$

were, E_n is the binding energy, R_∞ is the Rydberg constant, m_e is the electron mass, e is the elementary electron charge, ε_0 is the vacuum permittivity, and h is Plank's constant. Because the orbital radius also scales with principle quantum number as $\langle r \rangle \propto n^2 a_0$ (where a_0 is the Bohr radius), these atoms effectively become micron-scale electric dipoles. This physical size makes them highly sensitive to external perturbations of electric fields.

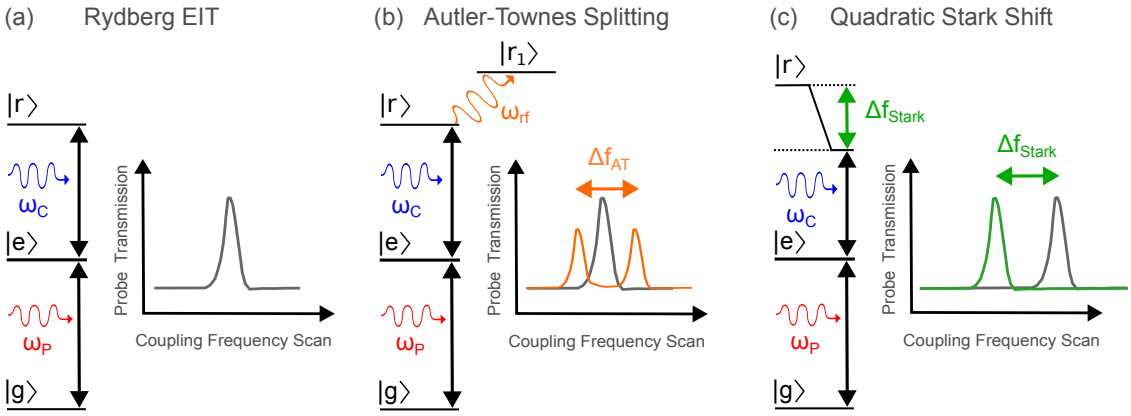

Figure 1.1: Rydberg EIT sensing schemes. In all configurations, the ground state $|g\rangle$ is coupled to an intermediate excited state $|e\rangle$ by a red probe laser. A blue coupling laser then promotes atoms from the intermediate state to a Rydberg state. (a) Basic Rydberg EIT: Holding the probe laser on resonance with the $|g\rangle \leftrightarrow |e\rangle$ transition while scanning the coupling laser frequency generates a transmission peak in the probe laser transmission spectra. This peak appears when both lasers reach resonance, signifying electromagnetically induced transparency. (b) Autler-Townes splitting: Coupling the Rydberg state to a nearby state $|r_1\rangle$ with a resonant rf field splits the EIT peak. The resulting separation between the two peaks directly corresponds to the strength of the applied rf field. (c) Non-resonant Stark shifting: In the presence of an external electric field, the Rydberg energy level shifts due to the Stark effect. This shift moves the EIT transmission peak in frequency, providing a direct measurement of the local electric field strength.

We can control and monitor atoms in these excited states using a coherent two-photon process called electromagnetically induced transparency (EIT) [26–28], which allows us to optically prepare and read out the energy levels of an ensemble of thermal atoms. Fig. 1.1 (a) shows EIT for a three-level ladder system. This spectroscopic transmission peak allows for all optical interrogation and preparation of the Rydberg states of atoms. Chapter 2 provides a detailed derivation of this phenomenon, and Fig. 1.1 (a) provides context for how atomic states are actually measured in experimental settings. A probe laser, with optical frequency ω_P, couples a ground state $|\mathrm{g}\rangle$ and intermediate excited state $|\mathrm{e}\rangle$, while a coupling laser, with frequency ω_C, promotes atoms from $|\mathrm{e}\rangle$ to the Rydberg state $|\mathrm{r}\rangle$. When both lasers are resonant with their respective atomic resonances, the medium exhibits a reduced absorption in the probe laser transmission since the valence electron of the atom occupies a coherent superposition of the ground and Rydberg states. Scanning the frequency of the control laser around this two-photon resonance produces a peak in transmission when the energy of the two lasers match the energy level difference between the ground and Rydberg states $\omega_C + \omega_P = \frac{\Delta E_{rg}}{h} = \frac{E_r - E_g}{h}$.

In Eq. 1.1, we can see that as n increases, the energy level spacing between Rydberg states with different n get closer together and can therefore be coupled by resonant rf electric fields [27, 29–35]. This coupling produces Autler-Townes (AT) splitting of the EIT resonance [36]. The splitting frequency Δf_{AT} depends on the transition dipole moment between the coupled Rydberg states $\mathbf{d}_{MW}$ and the rf electric field magnitude $|\mathcal{E}|$:

$$\Delta f_{AT} = \mathbf{d}_{MW}|\mathcal{E}|/h. \tag{1.2}$$

Fig. 1.1 (b) is a simple picture of how this AT splitting is measured experimentally. In the presence of an applied rf-field, the EIT peak splits in frequency proportional to the strength of the field. While not explored in this dissertation, this is a common method for rf measurements with Rydberg atoms.

Non-resonant electric fields also exploit the big electric dipole moment of Rydberg

states via the quadratic Stark effect, which shifts the atomic energy levels with different total angular momentum quantum numbers m_J by:

$$\Delta f_{Stark} = -\frac{1}{2}\alpha_{(n,l,j,mj)}|\mathcal{E}|^2/h. \tag{1.3}$$

where Δf_{Stark} denotes the frequency shift of the atomic energy level, $\alpha_{(n,l,j,mj)}$ is the atomic state polarizability, and $|\mathcal{E}|$ is again, the magnitude of the applied electric field [37]. This scalar polarizability $\alpha_{(n,l,j,mj)}$, represents the ease of inducing an atomic dipole, scales dramatically as n^7. Fig. 1.1 (c) shows the Stark shift to the Rydberg energy level in the three level diagram. The EIT peak shifts along the frequency axis based on the strength of the quadratic Stark shift. Since the polarizability $\alpha_{(n,l,j,mj)}$ depends on m_J, dc electric fields lift the degeneracy of high-angular-momentum Rydberg states, producing Stark manifolds that reflect both the magnitude and orientation of the applied field [38–40]. This will be discussed more in Chapter 2.

Property	Quantity	Scaling
Binding energy	E_n	n^{-2}
Level spacing	ΔE_n	n^{-3}
Orbital radius expectation value	$\langle$ r $\rangle$	n^2
State lifetime	τ	n^3
Scalar electric polarizability	α	n^7

Table 1.1: Scaling laws of Rydberg states with principle quantum number n adapted from [1–3]

Table 1.1 summarizes the relevant scaling laws that govern Rydberg-atom properties. One property in this table that is not directly related to electric field sensitivity is the atomic state lifetime that scales as n^3. This is particularly useful for spectroscopy measurements because the longer state lifetime ($\tau \sim 100$ μs for $n = 58$) leads to narrower atomic resonances, which in turn leads to more precise measurements of the electric field.

1.3 Brief overview of Rydberg atom based technologies

Rydberg atom technologies are at the core of many applications in both fundamental and applied physics. Ultracold Rydberg states form the basis for neutral-atom quantum information platforms [41, 42]. These systems utilize long-range dipole-dipole interactions between closely trapped atoms to realize the Rydberg blockade effect [43, 44]. In this regime, the excitation of a single atom shifts the energy levels of neighboring atoms, preventing them from resonant optical excitation to the Rydberg state. Researchers leverage this effect to create logical qubits for quantum computers and to develop single-photon sources [45, 46] for number state generation for quantum networks.

Beyond quantum information and computing, Rydberg sensors are in metrology applications. Cold Rydberg ensembles enable traceable thermometry by measuring blackbody radiation [47, 48], relating temperature to measured frequency shifts via selective field ionization. These applications require cold atoms that are confined in a magneto-optical trap (MOT) or optical tweezer arrays, but practical applications involving Rydberg atoms can be done at room temperature in glass vapor cells. These portable cells eliminate the need for large, complex vacuum systems and magnetic confinement coils.

Since atomic-vapor based Rydberg sensors form the basis of the work for this dissertation, so now, we provide a brief overview of electric field metrology developments with Rydberg atoms. Early Rydberg sensors relied on incoherent excitations to the Rydberg state, promoting electrons using intense laser pulses. The plasma physics community used this approach to develop several spatially resolved measurement techniques across various atomic species [49–51]. These laser-induced fluorescence dip (LIF-dip) techniques monitor atomic state populations by detecting fluorescence from excited states. However, this incoherent excitation produces broad resonance linewidths, limiting measurement precision.

Coherent excitations to a Rydberg state via EIT proviedes much narrower linewidths, establishing alkali vapor cells as a rapidly advancing platform for both dc and rf metrology. Initial efforts focused on creating an SI-traceable electric field standard [37]. Because

of the quadratic Stark shift (Eq. 1.3) linking field strength to atomic polarizability and fundamental constants, these sensors provide an intrinsically calibrated electric field probe. A number of research groups have demonstrated dc electric field measurements using vapor cells with embedded electrodes [37, 40, 52] or by inducing charges on cell walls via energetic purple light photons [53, 54]. Nevertheless, dc sensing remains challenging; unlike magnetic fields [55], low-frequency electric fields are screened by a Rb layer on the glass of the vapor cell [35]. So, dc studies often require internal electrodes or specialized surface-charging techniques [56] to even have a field to measure.

The field of Rydberg sensing expanded significantly with the advent of rf electric field receivers [27, 29–35]. High-frequency rf fields penetrate vapor-cell glass, bypassing the dielectric screening that plagues dc measurements. This property has enabled rigorous studies of rf power standards and angle-of-arrival detection [57–60]. These systems can also be adapted for higher frequency terahertz fields for imaging and sensing [38, 61–63]. Both of these field-sensing techniques leverage EIT and Autler-Townes splitting to measure field strengths. Expanding beyond metrology, researchers have demonstrated practical applications with the rf-receivers too, such as streaming audio and video signals and enhancing existing rf ground-based satellites [64–67].

1.4 Sensing capabilities necessary for electron beam diagnostics

The research presented in this dissertation confronts several technical challenges in state-of-the-art Rydberg atomic sensing that must be addressed for implementing electron beam diagnostics. The first challenge involves measuring spatially varying electric fields. Conventional vapor-cell measurements detect laser transmission through the entire cell, which integrates the electric field over the entire atom-light interaction volume. Because of this, the recorded spectrum represents a spatial average rather than a localized measurement. Previous studies have measured electric fields that are uniform in the laser propagation di-

rection but vary transversely across the vapor cell [53, 68]. However, achieving true spatial resolution typically requires miniaturizing vapor cells or translating the interaction volume in space to see where the field is changing. These constraints and methods currently hinder the reconstruction of spatially varying dc field distributions because they are difficult to implement, and can modify the very fields being measured.

A second challenge is the lack of intrinsic directional sensitivity to dc electric fields. Characterizing arbitrary charge distributions requires measuring electric field vectors, but the quadratic nature of the Stark effect is only sensitive to field amplitude. While atomic selection rules and polarization control enable vector measurements in vapor-cell magnetometers [69, 70], extending this capability to dc electric fields is non-trivial [71]. Unlike rf field Rydberg receivers, where polarization selection rules facilitate directional measurements [57], dc fields introduce optical pumping and complex population dynamics that complicate vector extraction. As a result, directional dc electrometry remains largely unexplored.

Finally, the linewidth of the atomic resonance fundamentally limits the sensitivity of Rydberg vapor-cell sensors. In room-temperature vapors, Doppler broadening and transit-time effects restrict the minimum achievable EIT linewidth, which determines the smallest detectable electric field. To reduce this broadening, some groups explore Doppler-free, three-photon excitation schemes that mitigate this broadening and increase electric field sensitivity [33, 72–75]. These approaches reduce the sensing volume, but also lower the signal strength through the reduced sensing volume, making it hard to achieve experimentally. These limitations prevent current vapor-cells from reaching the low-field amplitudes detectable by classical antenna-based methods.

1.5 Outline

This dissertation presents work on addressing all of these technical challenges and demonstrating applications of Rydberg atom electric field sensors. It is organized as follows:

Chapter 2 gives a fundamental theory for EIT resonances involving Rydberg atoms and their modification in the presence of electric fields. We use this theory to construct fitting functions to extract values of electric fields in reported experiments.

Chapter 3 details the electron beam apparatus used in experiments in Chapters 4 and 5. This chapter describes how the apparatus works, and serves as a guide for how to use it.

Chapter 4 describes the fluorescence-based detection method for measuring spatially varying electric fields, and its application to measure the position, size and current of an electron beam.

Chapter 5 provides an alternative e-beam diagnostic, in which to probe the spatially varying fields, we cross the laser beams at an angle and record the transmission of light through the cell.

Chapter 6 expands Rydberg EIT techniques into vector measurements through demonstrating polarization-dependent dc electric field measurements.

Chapter 7 explores a new detection scheme for an all-optical Ramsey interrogation of Rydberg coherences. We theoretically propose a method to reduce the EIT linewidth in room temperature vapor cell experiments through a temporal or spatially separated Ramsey interrogation.

Finally, Chapter 8 summarizes the dissertation and gives an outlook on the many future directions this work can take.

Chapter 2

Atom-light interactions and Stark shift theory

2.1 Three-level model for Rydberg EIT

As discussed in Chapter 1, EIT serves as the backbone for room-temperature Rydberg state measurements. Because the physics governing EIT is well established, we present an overview of atomic interactions with light and external optical and electric fields, and describe some numerical methods for solving such atomic systems [2–4, 76–84].

2.1.1 Interaction Hamiltonian in the rotating wave approximation

Fig. 2.1 shows a three-level ladder system consisting of a ground state $|g\rangle$, an intermediate excited state $|e\rangle$, and a Rydberg state $|r\rangle$. The atomic Hamiltonian can be written as

$$H_0 = \begin{pmatrix} \hbar\omega_g & 0 & 0 \\ 0 & \hbar\omega_e & 0 \\ 0 & 0 & \hbar\omega_r \end{pmatrix}, \tag{2.1}$$

where $\hbar\omega_g$, $\hbar\omega_e$, $\hbar\omega_r$ are the energies of the respective states.

We implement a semi-classical approach in which the atoms are treated quantum mechanically, and the optical fields are treated classically [83, 85, 86]. A probe field of frequency Ω_P drives the $|g\rangle \leftrightarrow |e\rangle$ transition, while a coupling field of frequency Ω_C drives

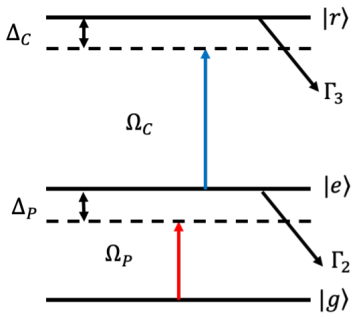

Figure 2.1: Three level ladder system with ground state $|g\rangle$, excited state $|e\rangle$ and Rydberg state $|r\rangle$. Probe laser with coupling Rabi frequency Ω_P couples $|g\rangle$ and $|e\rangle$, while a coupling laser with Rabi frequency Ω_C couples $|e\rangle$ and $|r\rangle$. Δ_P and Δ_C are the detunings of the probe and coupling lasers, respectively.

the $|e\rangle \leftrightarrow |r\rangle$ transition. The optical field produced from the two lasers that interact with this atom is

$$\mathbf{E}(\mathbf{r},t) = \frac{1}{2}E_P\hat{\epsilon}_P e^{i[\mathbf{k}_P\mathbf{r}-\omega_P t]} + \frac{1}{2}E_C\hat{\epsilon}_C e^{i[\mathbf{k}_C\mathbf{r}-\omega_C t]} + c.c., \tag{2.2}$$

where $\hat{\epsilon}_{P,C}$ are the light polarization vectors, $\mathbf{k}_{P,C}$ are the wavevectors, $E_{P,C}$ are the field amplitudes, and *c.c.* is the complex conjugate [2, 80, 83].

Under the dipole approximation (the wavelength of the light is much greater than the size of the atom, $\lambda \gg a_0$), the spatial variation of this field across the atom is neglected. The expression for the electric field then reduces to

$$\mathbf{E}(t) = \frac{1}{2}E_P\hat{\epsilon}_P e^{-i\omega_P t} + \frac{1}{2}E_C\hat{\epsilon}_C e^{-i\omega_C t} + c.c. \tag{2.3}$$

The atom-light field interaction is described by the interaction Hamiltonian

$$H_I = e\mathbf{r}\cdot\mathbf{E}(t). \tag{2.4}$$

where $\mathbf{r}$ is the electron position operator and e is the charge of the electron. In the $\{|g\rangle, |e\rangle, |r\rangle\}$ basis, this interaction Hamiltonian can be written as

$$H_I = \begin{pmatrix} 0 & \frac{\hbar\Omega_P}{2}e^{-i\omega_P t} & 0 \\ \frac{\hbar\Omega_P}{2}e^{-i\omega_P t} & 0 & \frac{\hbar\Omega_C}{2}e^{-i\omega_C t} \\ 0 & \frac{\hbar\Omega_C}{2}e^{-i\omega_C t} & 0 \end{pmatrix} + h.c., \tag{2.5}$$

where h.c. is the Hermitian conjugate of the matrix, and the Rabi frequencies ($\Omega_{P,C}$) are defined as

$$\Omega_P = \frac{eE_P}{\hbar}\langle g|\mathbf{r}\cdot\hat{\epsilon}_P|e\rangle \tag{2.6a}$$

$$\Omega_C = \frac{eE_C}{\hbar}\langle e|\mathbf{r}\cdot\hat{\epsilon}_C|r\rangle. \tag{2.6b}$$

The total Hamiltonian of this atomic system is $H = H_0 + H_I$. To handle time dynamics of the system into the Hamiltonian and the state vector, we transform to the interaction picture (i.e. rotating frame) using the unitary operator

$$\mathcal{U} = \begin{pmatrix} e^{i\omega_g t} & 0 & 0 \\ 0 & e^{i(\omega_g+\omega_P)t} & 0 \\ 0 & 0 & e^{i(\omega_g+\omega_P+\omega_C)t} \end{pmatrix}. \tag{2.7}$$

The Hamiltonian and state vector $|\psi\rangle$ transform as

$$|\psi\rangle \rightarrow |\psi\rangle' = \mathcal{U}|\psi\rangle, \tag{2.8a}$$

$$H \rightarrow H' = \mathcal{U}H\mathcal{U}^\dagger - i\hbar\dot{\mathcal{U}}\mathcal{U}^\dagger, \tag{2.8b}$$

where $\mathcal{U}^\dagger$ is the Hermitian conjugate, and $\dot{\mathcal{U}}$ is a time derivative of the transformation operator. Neglecting rapidly oscillating terms such as $\omega_P + \omega_C$, $2\omega_P$ and $2\omega_C$ (rotating wave approximation), the Hamiltonian reduces to

$$H' = \begin{pmatrix} 0 & \frac{\hbar\Omega_P^*}{2} & 0 \\ \frac{\hbar\Omega_P}{2} & -\hbar\Delta_P & \frac{\hbar\Omega_C^*}{2} \\ 0 & \frac{\hbar\Omega_C}{2} & -\hbar(\Delta_P + \Delta_C) \end{pmatrix}. \tag{2.9}$$

Here, the detunings, or deviations from atomic energy levels, are defined as

$$\Delta_P = \omega_P - (\omega_e - \omega_g) \tag{2.10a}$$

$$\Delta_C = \omega_C - (\omega_r - \omega_e) \tag{2.10b}$$

This Hamiltonian forms the basis for the EIT transmission model developed in the following sections.

2.1.2 Optical Bloch equations

Time evolution of atomic states may in principle be described using the time-dependent Schrödinger equation. However, this approach does not account for dissipative processes such as spontaneous emission or laser-induced dephasing. To incorporate these effects, we employ a density matrix formalism, which allows us to treat both coherent and incoherent decay dynamics consistently.

The density operator for pure states is defined as

$$\rho(t) = |\psi\rangle\langle\psi| = \begin{pmatrix} \rho_{gg} & \rho_{ge} & \rho_{gr} \\ \rho_{eg} & \rho_{ee} & \rho_{er} \\ \rho_{rg} & \rho_{re} & \rho_{rr} \end{pmatrix}, \tag{2.11}$$

where the diagonal terms represent populations of the atomic states, and the off-diagonal terms represent coherences between states.

The time evolution of the density matrix is governed by the Lindblad master equation,

$$\frac{\partial \rho(t)}{\partial t} = \frac{-i}{\hbar}[H, \rho(t)] + \sum_i \mathcal{L}(\rho, \sigma_i), \tag{2.12}$$

where H is the system Hamiltonian given by (Eq. 2.9), and $\mathcal{L}$ is the Lindblad superoperator defined by

$$\mathcal{L}(\rho, \sigma_i) = \sum_i \sigma_i \rho \sigma_i^\dagger - (\sigma_i^\dagger \sigma_i \rho + \rho \sigma_i^\dagger \sigma_i)/2, \tag{2.13}$$

with σ_i representing collapse operators that describe dissipative processes.

We consider two primary classes of collapse operators. The first describes spontaneous decay of atomic populations, determined by the natural lifetimes of the states. The excited state decays only to the ground state with a state lifetime Γ_2, and the Rydberg state decays to the intermediate excited state with a state lifetime Γ_3.

$$\sigma_{ge} = \begin{pmatrix} 0 & \sqrt{\Gamma_2} & 0 \\ 0 & 0 & 0 \\ 0 & 0 & 0 \end{pmatrix}, \quad \sigma_{er} = \begin{pmatrix} 0 & 0 & 0 \\ 0 & 0 & \sqrt{\Gamma_3} \\ 0 & 0 & 0 \end{pmatrix}. \tag{2.14}$$

There are no decays from the Rydberg state directly to the ground state due to selection rules. The second class captures additional dephasing arising from finite probe and coupling laser linewidths ($\gamma_{P,C}$ respectively). Three operators are introduced to construct a Lindblad superoperator consistent with [80]:

$$\sigma_{lw_1} = \begin{pmatrix} \sqrt{-\gamma_C + \gamma_P + (\gamma_P + \gamma_C)} & 0 & 0 \\ 0 & 0 & 0 \\ 0 & 0 & 0 \end{pmatrix}, \quad \sigma_{lw_2} = \begin{pmatrix} 0 & 0 & 0 \\ 0 & \sqrt{\gamma_C + \gamma_P - (\gamma_P + \gamma_C)} & 0 \\ 0 & 0 & 0 \end{pmatrix},$$
$$\sigma_{lw_3} = \begin{pmatrix} 0 & 0 & 0 \\ 0 & 0 & 0 \\ 0 & 0 & \sqrt{\gamma_C - \gamma_P + (\gamma_P + \gamma_C)} \end{pmatrix}. \tag{2.15}$$

From these collapse operators, the Lindblad superoperators for spontaneous decay and laser-induced dephasing are

$$\mathcal{L}_D = \begin{pmatrix} \Gamma_2\rho_{ee} & -\frac{\Gamma_2}{2}\rho_{ge} & -\frac{\Gamma_3}{2}\rho_{gr} \\ -\frac{\Gamma_2}{2}\rho_{eg} & -\Gamma_2\rho_{ee} + \Gamma_3\rho_{rr} & -\frac{\Gamma_2+\Gamma_3}{2}\rho_{er} \\ -\frac{\Gamma_3}{2}\rho_{rg} & -\frac{\Gamma_2+\Gamma_3}{2}\rho_{re} & \Gamma_3\rho_{rr} \end{pmatrix}, \tag{2.16a}$$

$$\mathcal{L}_{lw} = \begin{pmatrix} 0 & -\gamma_P\rho_{ge} & -(\gamma_P + \gamma_C)\rho_{gr} \\ -\gamma_P\rho_{eg} & 0 & -\gamma_C\rho_{er} \\ -(\gamma_P + \gamma_C)\rho_{rg} & -\gamma_C\rho_{re} & 0 \end{pmatrix}. \tag{2.16b}$$

Together with the system Hamiltonian and the trace condition $\rho_{gg}+\rho_{ee}+\rho_{rr} = 1$, these equations fully determine the optical Bloch equations. For time-independent (or steady-state) interactions, we can set the left side of Eq. 2.12 to zero, and find density matrix elements for both state populations and coherences. Later, in Chapter 7, when we need

to investigate temporal behavior, we will use numerical methods to accurately capture the time evolution of atomic states.

For the steady state case, we can write an analytical form of the coherence between the ground and excited state ρ_{ge}:

$$\rho_{ge} = \frac{i\Omega_P^*}{2}\left[i\Delta_P + \frac{\Gamma_2}{2} + \gamma_P + \frac{|\Omega_C|^2/4}{i(\Delta_C + \Delta_P) + \Gamma_3/2 + \gamma_P + \gamma_C}\right]^{-1}, \tag{2.17}$$

This coherence is related to atomic susceptibility χ which dictates the absorption coefficient α and refractive index of the medium n_R,

$$\chi(\Delta_P, \Delta_C) = -\frac{2\mathcal{N}|\mathbf{d}_{ge}|^2}{\hbar\epsilon_0\Omega_P}\rho_{eg} \tag{2.18a}$$

$$\alpha = k_P Im\left[\chi\right] \tag{2.18b}$$

$$n_R = 1 + Re\left[\chi\right]/2, \tag{2.18c}$$

where $\mathcal{N}$ is the number density of the ensemble of atoms, $\mathbf{d}_{ge}$ is the dipole moment between the ground and excited state, and $\rho_{eg} = \rho_{ge}^*$.

While Eq. 2.17 is the full steady state solution of the atomic coherence term, there are a lot of terms in the equation which obscures why EIT is so beneficial for spectroscopic sensing. In the case where $\Delta_P = 0$ and $\gamma_{P,C} = 0$ Eq. 2.17 simplifies to

$$\rho_{ge} = i\Omega_P^*\left[\frac{2i\Delta_C + \Gamma_3}{2|\Omega_C|^2 + 2\Gamma_2\Gamma_3 + \frac{i\Gamma_2}{2}\Delta_C}\right]. \tag{2.19}$$

Here its a little easier to see the benefits of EIT. For increasing coupling power, $|\Omega_C| \to \infty$ $\rho_{ge} \to 0$. If $\rho_{ge} \to 0$, then the absorption coefficient is also zero, so there is a completely transmissive window. Also, ρ_{ge} depends on the lifetime of the Rydberg state Γ_3. For Rydberg states $\Gamma_3 \gg \Gamma_2$, and therefore, this non-linear effect can produce spectroscopic features that are much narrower than the lifetime of the intermediate excited state.

Fig. 2.2 shows these benefits by plotting the transmission, T, of probe light through the atomic medium, where $T = e^{-\alpha L}$, where L is the length of the atomic interaction region. The figure demonstrates two different scenarios. In Fig. 2.2 (a), the coupling laser is held on resonance ($\Delta_C = 0$) while the probe laser sweeps across the atomic transition. Without the coupling laser, the atomic response is an absorption profile governed by the intermediate excited state lifetime, corresponding to the ($i\Delta_P + \frac{\Gamma_2}{2}$) term in Eq. 2.17. Activating the coupling field creates a transmissive peak when the combined laser frequencies satisfy the two-photon resonance condition ($\Delta_C + \Delta_P = \frac{\Delta E_{rg}}{h} = \frac{E_r - E_g}{h}$) where E_r and E_g are the energy of the Rydberg and ground state respectively [26, 83, 85]. This quantum interference in the atomic coherence provides the primary advantage of EIT for high-precision spectroscopy. Fig. 2.2 (b) shows another configuration where now the probe laser remains fixed ($\Delta_P = 0$) while the coupling laser detuning is swept. In this configuration, the transmissive peak is the only atomic response on top of a constant background. Due to the dependence on the excited state lifetime, EIT yields a spectral linewidth much narrower than the intermediate excited state.

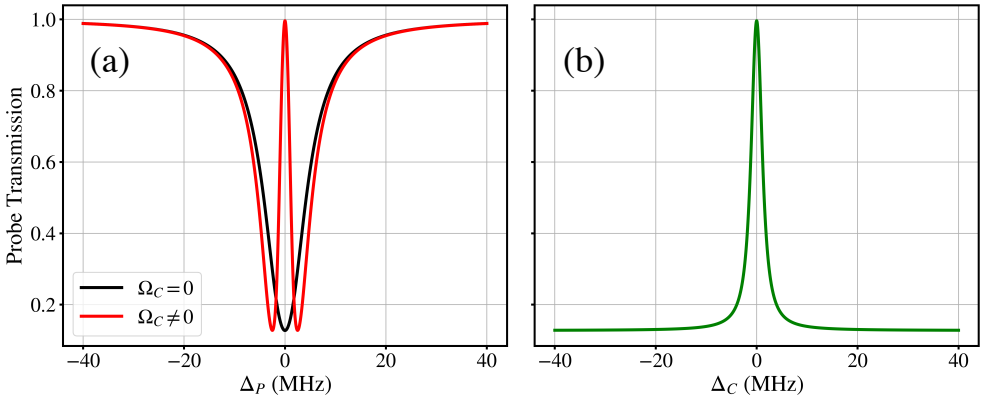

Figure 2.2: Steady state EIT model from coherence. (a) Sweep of the probe laser detuning with $\Delta_C = 0$, $\Gamma_2 = 6$ MHz $\times 2\pi$, $\Gamma_3 = 8$kHz $\times 2\pi$, $\Omega_C = 0.5\Gamma_2$, $\Omega_P = 0.1\Gamma_2$, $\mathcal{N} \sim 10^{15}\ m^{-3}$, and $\mathbf{d}_{ge} = 3 \times 10^{-29}$ C·m. This is a stationary atom steady state EIT absorption curve with no laser linewidths. (b) Sweep of coupling laser detuning with $\Delta_P = 0$ and all other parameters the same. Sweeping the coupling laser removes the two-photon background signal.

Alternatively, instead of the coherence between the ground and excited state, we can also monitor the population of the intermediate excited state through fluorescence mea-

surements which is of interest in Chapter 4. To model this, we numerically solve the Lindblad master equation with QuTip [76] and extract the steady state ρ_{ee} density matrix element. Fig. 2.3 shows the excited state population as a function of the coupling laser detuning. The important thing to note about this graph is that at the two-photon resonance condition, there is a depletion of the excited state population. So, just like monitoring the coherence ρ_{eg} that correlates to transmission of light through the cell, now we can monitor the fluorescence of the intermediate excited state and see similar behavior as the narrow spectroscopic EIT peak. However, it is easier to observe spatial variations of the fluorescence along the probe laser path.

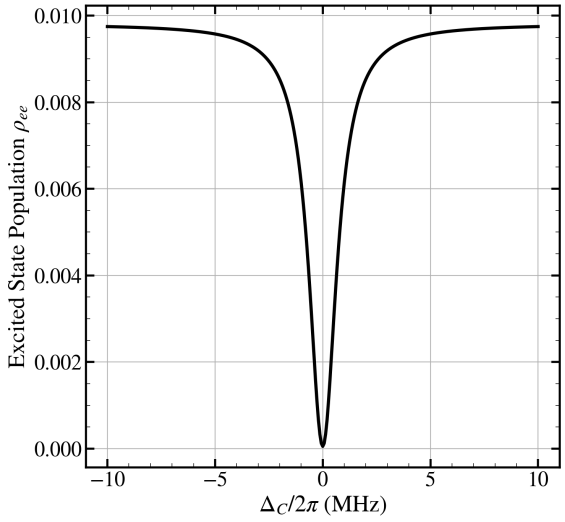

Figure 2.3: Steady state population as a function of coupling laser detuning using the same atomic parameters as in Fig. 2.2. When both lasers are on resonance with the EIT transition, there is a dip in the population of the excited state ρ_{ee}. The dip in the excited state population is what we use for fluorescence imaging in later sections.

2.2 Doppler effect in thermal vapors

While the steady-state solution of the Lindblad equation captures the coherent and dissipative dynamics of stationary atoms, it does not account for atomic motion. The formalism described previously is valid for stationary atoms where Doppler shifts due to atomic mo-

tion do not play any role, but in our experiments, the atoms are in a thermal vapor inside a glass cell. To account for the effects of atomic motion at fixed temperatures, we must incorporate Doppler shifts arising from the velocity distribution of the atoms along the direction of laser propagation.

The atomic motion is assumed to follow a thermal Maxwell-Boltzmann velocity distribution. In one dimension along the laser propagation axis, this is expressed as

$$\mathcal{P}(u) = \frac{1}{\sqrt{\pi}} \int_{-\infty}^{\infty} e^{-u^2} du, \tag{2.20}$$

where $\mathcal{P}(u)$ is the probability of atoms having atomic velocity u, $u \equiv v_z/\sigma_v$ is the dimensionless velocity, $\sigma_v \equiv \sqrt{2k_BT/m}$ is the root-mean-square velocity for atoms of mass m at temperature T, v_z is the velocity along the optical axis, and k_B is the Boltzmann constant.

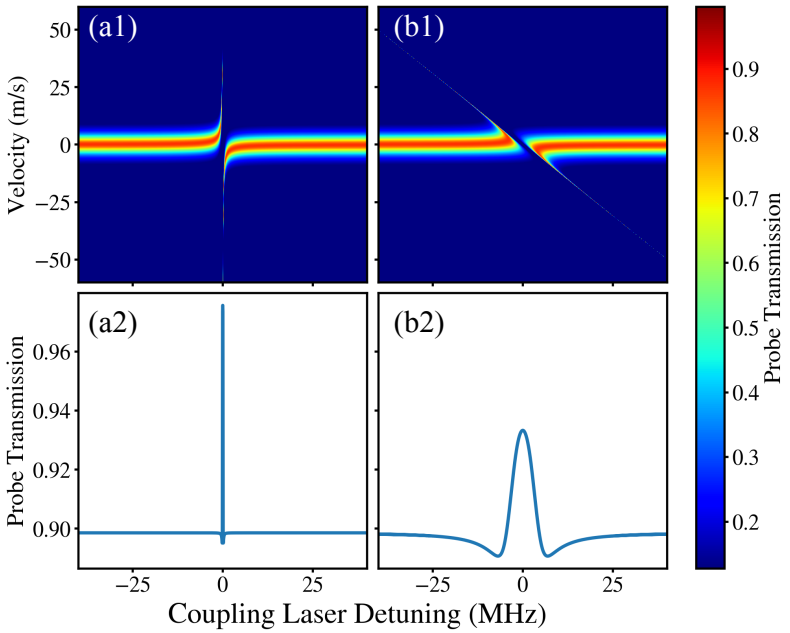

Figure 2.4: Adapted from [2]. Wavelength dependence of Doppler averaging in EIT. Top: transmission of individually shifted spectra per velocity class for (a1) $\lambda_P = \lambda_C = 780$ nm (b1) $\lambda_P = 780$ nm and $\lambda_P = 480$ nm. Bottom: Doppler-averaged probe laser transmission signals corresponding to (a1) and (b1).

In the rest frame of the atoms, they "see" the light at slightly different frequencies thereby modifying the two-photon resonance condition. The Doppler shift modifies the

effective detunings of the probe and coupling lasers for each velocity class v_z as

$$\Delta'_P(v_z) = \Delta_P + \frac{2\pi}{\lambda_P} v_z, \tag{2.21a}$$

$$\Delta'_C(v_z) = \Delta_C - \frac{2\pi}{\lambda_C} v_z, \tag{2.21b}$$

where $\lambda_{P,C}$ are the wavelengths of the probe and coupling fields. The susceptibility becomes velocity-dependent such that $\chi(\Delta'_P, \Delta'_C) \equiv \chi(v_z)$. For effective cancellation of the Doppler shift, because the wavelength of the probe and coupling lasers are significantly different, most experiments employ a counter propagating geometry of the probe and coupling laser [77, 78, 87].

Fig. 2.4 (a1 - b1) show the velocity dependent shift of the EIT resonance when the wavelength of the probe and coupling laser are the same, and when $\lambda_P = 780$ nm and $\lambda_C = 480$ nm. In these heat maps, the bright red colors show the location of the two-photon EIT peak. For the case when the wavelengths are the same, there is very little spread across the frequency axis. This is because the Doppler mismatch of the two laser fields is zero. In contrast for our mismatched wavelength case, there is a sharp spread of the red line along the frequency axis. This highlights the challenge of why there is a "residual Doppler broadening" of the atomic resonance. Another consequence of these mismatched wavelengths is that the scaling between atomic resonances changes based on the laser being frequency scanned. Appendix A discusses the frequency scaling in the frequency mismatched ladder system more.

The Doppler-averaged susceptibility is obtained by integrating over the thermal distribution of longitudinal velocities

$$\chi^{avg} = \frac{1}{\sqrt{\pi}} \int_{-\infty}^{\infty} e^{-u^2} \chi(v_z) dv_z. \tag{2.22}$$

We use this Doppler-averaged susceptibility for accurate modeling of the EIT lineshape

in thermal vapor. Fig. 2.4 (a2 - b2) show the averaged response of all shifted velocity classes. In these plots, again for the case where the wavelengths are the same, there is a narrow peak, but in the mismatched wavelength case, there is a reduction in amplitude and substantially broader resonance. To avoid excessive calculations of atomic spectra, it is useful to understand the lineshape of this Doppler broadened resonance to use in primitive simulations.

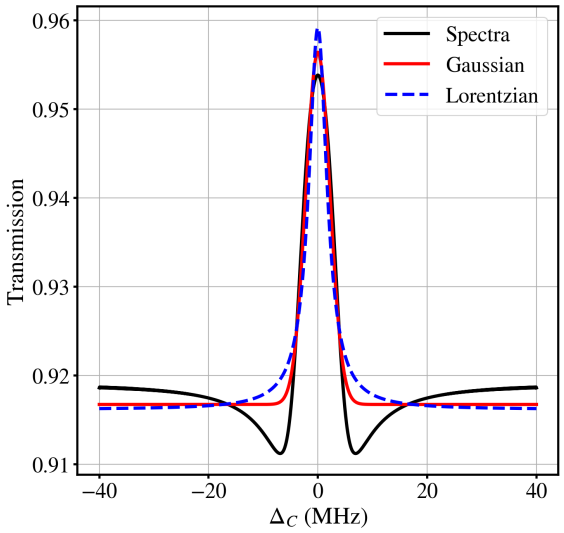

Figure 2.5: Fitting Doppler broadened EIT spectra with different Lorentzian and Gaussian functions. The fit shows that the Gaussian profile captures the central peak better than the Lorentzian function because the longer tails of the Lorentzian function do not fit generated spectra.

Fig. 2.5 shows a comparison of a Gaussian and Lorentzian lineshape used to fit the atomic spectra. In the simulated spectra, there is more nonlinearity away from the central peak that is not described by either function. In experimental spectra, this nonlinearity is washed away due to power broadening, misalignment broadening, or other broadening mechanisms not accounted for in the simple Doppler broadening case, but is has been observed with strong enough laser power and is known as electromagnetically enhanced absorption [87, 88]. However, it is apparent that the tails of the Lorentzian function fall away from the spectra near ± 5 MHz. Doing a reduced χ^2 analysis between these two fits, neither model really captures the behavior of this data, but the Gaussian fit has a value

closer to one and therefore is used to model EIT resonances for future analysis. As such in Chapters 4 and 6, we model the EIT signal S as Gaussian with the form

$$S(\Delta_C) = \exp(-\frac{[\Delta_C - \Delta f_{Stark}(E)]^2}{2\gamma_{EIT}^2}), \tag{2.23}$$

where $\Delta f_{Stark}(E)$ is the Stark shifts of the atomic energy levels using methods described in the next section and γ_{EIT} is an empirically set linewidth of the EIT resonance that captures the Doppler broadening of experimental spectra.

2.3 Static electric fields and Stark Effects

We now consider the interaction of Rydberg atoms with static dc electric fields. In the presence of an external dc electric field $\vec{\mathcal{E}}$, a neutral atom with electric dipole operator $e\mathbf{r}$ experiences the following interaction energy:

$$U_e = e\mathbf{r} \cdot \vec{\mathcal{E}}. \tag{2.24}$$

This interaction is treated with time-independent perturbation theory and gives rise to shifts of the atomic energy levels known as the Stark effect. For states with low angular momentum (ℓ), the first-order (linear) Stark shift vanishes, and the leading contribution is the second order term. The quadratic Stark shift is given by

$$\Delta E_{Stark}^{(2)} = \sum_{n',\ell',j',m_j'} \frac{|\langle n',\ell',j',m_j'|e\mathbf{r}\cdot\vec{\mathcal{E}}|n,\ell,j,m_j\rangle|^2}{E_{n,\ell,j,m_j}^{(0)} - E_{n.,\ell',j',m_j'}^{(0)}}. \tag{2.25}$$

Here, $E^{(0)}$ denotes the unperturbed atomic energies, and the unperturbed eigenstates are written as

$$|n,\ell,j,m_j\rangle = \frac{\rho_*(r)}{r}\mathcal{Y}_{j,m_j,\ell}(\theta,\phi), \tag{2.26}$$

where $\rho_*(r)$ is the reduced radial wavefunction and $\mathcal{Y}_{j,m_j,\ell}(\theta,\phi)$ are the generalized spherical harmonics [2, 19, 83]. In the case where the electric dipole moment is directed along $\vec{\mathcal{E}}$, the induced Stark effect in terms of a state-dependent polarizability is

$$\Delta E^{(2)}_{Stark} = -\frac{1}{2}\alpha_{(n,l,j,m_j)}E^2. \tag{2.27}$$

where E is the magnitude of the electric field and is the same as in Eq. 1.3. The polarizability $\alpha_{(n,l,j,m_j)}$ has scalar and tensor components:

$$\alpha_{(n,l,j,m_j)} = \alpha^S_{(n,l,j,m_j)} + \alpha^T_{(n,l,j,m_j)}\frac{3m_j^2 - j(j+1)}{j(2j-1)}. \tag{2.28}$$

The scalar term α^S is independent of the total angular momentum sublevels, while the tensor term α^T introduces differential shifts between m_j states depending on the projection of the electric field onto the quantization axis.

This perturbative formulation is exact for hydrogen. Although alkali-metal Rydberg states are hydrogen-like at large principal quantum numbers, they deviate from hydrogenic behavior due to the finite ionic core and associated quantum defects. To account for this discrepancy, accurate Stark shifts are obtained by numerically diagonalizing the full Stark Hamiltonian in a sufficiently large basis of unperturbed Rydberg states to account for core-induced mixing and level interactions. ARC and the full numerical solution of the Stark Hamiltonian process is a tool for us, and an complete derivation of this numerical method can be found in these sources [1–3, 84].

Fig. 2.6 shows experimentally measured Stark-shifted Rydberg energy levels for the 36D state compared with the numerical calculations obtained using the Alkali-Rydberg Calculator (ARC) [4]. In the plot there are two degenerate fine structure states that are split into three resonances for $j = 5/2$ and two resonances for $j = 3/2$. This is because the Stark effect lifts the degeneracy of the m_j states and because it is quadratic the $\pm m_j$ states will shift the same. For the $j = 5/2$ peaks, the $|m_j| = 5/2$ peak shifts in frequency the most because it is the state with the largest dipole moment. Also notice that while

the $|m_j| = 5/2, 3/2$ peaks go down in energy, the $|m_j| = 1/2$ peak actually shifts the other direction. In the $j = 3/2$ state, both peaks shift the same direction, but at different rates. We expect that at small electric fields compared to the sensitivity of the Rydberg state, the Stark shifts will be nearly quadratic following Eq. 1.3, and for the electric field range sampled in Fig. 2.6, all shifts are nearly quadratic with no dramatic shifts.

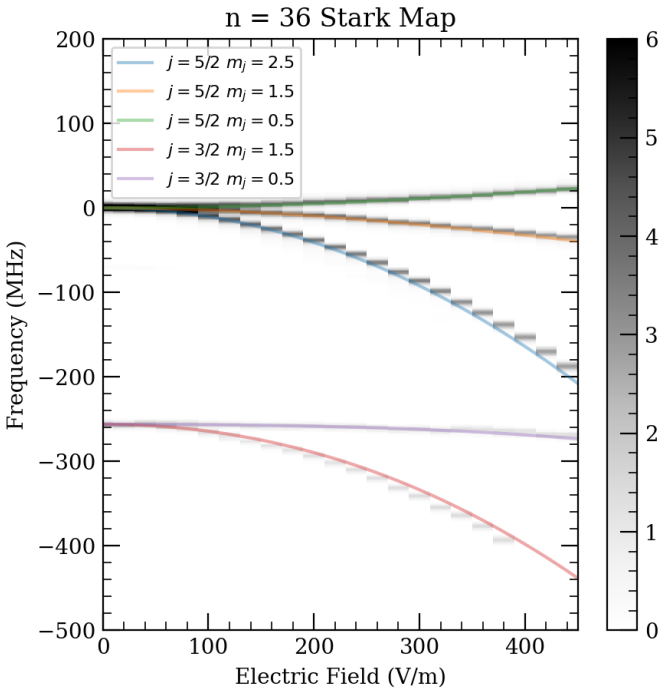

Figure 2.6: Stark map of 36D Rydberg spectra. The heat map is the measured atomic spectra, and the overlaid lines correspond to the Stark shifted sublevels obtained through ARC [4].

In contrast in Fig. 2.7, we see the deviation of simple quadratic shifts of the Stark effect that arises from quantum defects of the finite core of alkali-atoms. For this numerically solved Stark map, we now consider the $n = 58$D Rydberg state which is far more sensitive to electric fields, and closer to other Rydberg energy levels. Note that the axis in Fig. 2.7 covers a much smaller range of electric field than that in Fig. 2.6. While the energy level degeneracy of the fine structure levels is the same as in Fig. 2.6, the difference is that there is less of a quadratic response of the $j = 5/2$ $|m_j| = 1/2$ peak for the $n = 58$D state. It follows the quadratic rise until ~ 80 V/m, but then turns back on itself. Because of this

non-linearity present in the Rydberg atom response to electric fields, instead of using the simple quadratic Stark shift like in Eq. 2.27, in Chapters 4, and 6, we use an interpolation of the numerically calculated Stark maps to reconstruct electric field values from measured spectra.

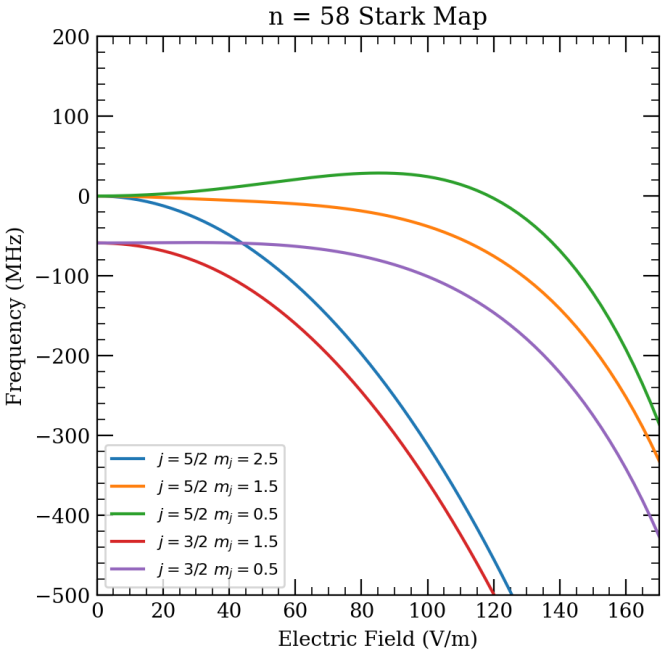

Figure 2.7: Stark map of 58D Rydberg spectra using ARC [4]. This state is more sensitive to electric fields and closer to neighboring Rydberg states, so there is greater non-linearity in the state shifts.

2.4 Summary

The framework developed in this chapter connects static electric fields to experimentally measured Rydberg EIT transmission spectra. Electric fields shift Rydberg energy levels through the Stark effect; these shifts modify the two-photon detuning in the three-level Hamiltonian; the steady-state coherence determines the optical susceptibility; and Doppler averaging produces the transmission profile observed in thermal vapor. In the following Chapters, this model is applied to extract quantitative electric field values from measured spectra and solve for the time dynamics of the interaction Hamiltonian.

Chapter 3

Experimental Apparatus

The experiments described in Chapters 4 and 5 investigate non-invasive diagnostics for an electron beam (e-beam). This Chapter provides a description of the e-beam apparatus. Technical descriptions of the key components are based on STAIB instrument documentation for the electron gun and related hardware.

Fig. 3.1 shows an overview of the vacuum system used for these experiments. The electrons follow a path through the chamber known as the beamline. This beamline originates at the electron emission filament source, where a high current flows through a wire to produce a continuous wave (CW) source of electrons that are accelerated and focused into a collimated beam. For pulsed control of this CW beam, the electrons pass through a pulsing unit designed to quickly turn the beam on and off at a rate up to 1 MHz.

As the beam propagates further, it enters a four-way cross that houses a movable optical transition radiation (OTR) screen. By intercepting the beam with this piece of copper, we can monitor the two-dimensional profile of the beam along the propagation axis at this specific location. Beyond this cross, the e-beam traverses a Rb chamber containing rubidium vapor. This component serves as the primary science interaction region, enabling non-invasive coherent sensing of electric fields via EIT and incoherent impact fluorescence measurements of the e-beam. Finally, the beam terminates at a Faraday cup, which also serves as a beam dump. This diagnostic tool captures the total electron flux, providing a

real-time monitor of the relative e-beam current.

The whole vacuum chamber is maintained at a base pressure of approximately 5×10^{-8} Torr using a PFeiffer HiCUBE 300 ECO turbo pump. Pressure is monitored with a Kurt J. Lesker cold cathode/Pirani combination gauge mounted on the top port of the four-way cross that houses the OTR screen.

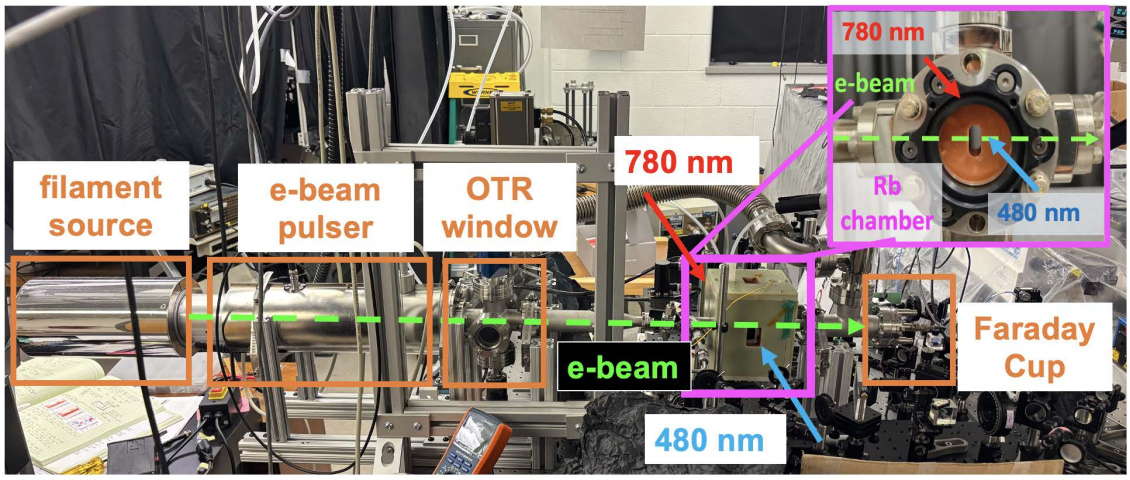

Figure 3.1: Image of the experimental apparatus. Components related to the electron beam are labeled in orange text. The green dashed line indicates the e-beam path, and the Rb chamber is highlighted in the magenta box.

3.1 Functional beamline components

3.1.1 Electron beam source

The electron source in our apparatus is a STAIB Instruments EH-30 thermionic emission electron gun. Fig. 3.2 (a) shows the source installed on the vacuum chamber, along with schematic diagrams of its internals, Fig. 3.2 (b). These diagrams shows what this component looks like, and the simplified diagram of the internals illustrates the working principle of the device and different stages of control within the emission source.

Thermionic emission sources generate electrons by heating a metallic cathode "hairpin" filament to high temperatures by running current through the wire. The applied heating

current of 3.25 A raises the filament temperature sufficiently for electrons to overcome the material work function, resulting in continuous electron emission [89].

The source is designed for operation in the 10 - 30 keV energy range. Beam energy, emission current, focusing, and steering are controlled electronically through a rack-mountable box. Fig. 3.3 shows the electron gun controller and the 20 keV high-voltage power supply used to accelerate the emitted electrons. For safe operation, the controller is connected to the lab door interlock system. If the interlock is triggered, power to the electron gun controller is disabled, and a system reboot is required.

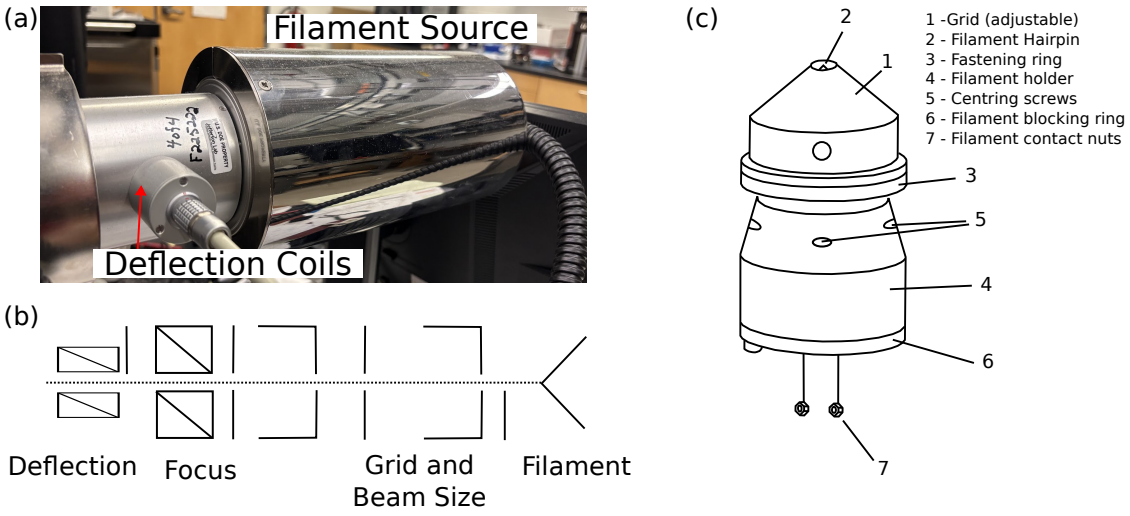

Figure 3.2: Electron beam emission source. (a) Image of filament source installed on the vacuum chamber. (b) Schematic diagram of the internals of the emission source. (c) Diagram of the filament source with relevant components numbered (figure from [Staib Instruments Manual]).

The parameters on the control units are: (1) the filament heating current, which controls the amount of current flowing through the cathode filament and determines the maximum emission current (current of the emitted e-beam); (2) the grid voltage, which controls the amount of electrons accelerated from the filament and therefore sets the working emission current; and (3) the focus voltage, which controls beam divergence and focal position. In our apparatus, a filament current of 3.25 A should provide emission currents up to approximately 1 mA, according to the manufacturing datasheet. In reality, the most I have seen is 500 μA reported by the gun controller before installation of the pulser unit.

Increasing the filament heating and current more than 3.25 A can provide more emission current, but greatly reduces the lifetime of the filament.

During approximately two years of regular operation of running the cathode at 3.25 A, the filament burned out once. Fig. 3.2 (c) is a diagram of the source assembly that is in the metallic shielding, and points to where the filament sits within this component. The filament is easily broken during handling, so use extreme caution when handling. A detailed procedure is in the user manual of the electron source, so refer to this if you ever need to change it. Although the filament replacement can be performed in-house, the people at the STAIB office can also do it if you need to order a new filament, so sometimes it is easier to transport the source to them so they can do it.

Figure 3.3: Electron beam controllers. (a) Filament source controller for energy, emission current, and steering. (b) Voltage source.

Beam position is controlled using magnetic deflection coils located downstream of the focusing element within the emission source. Independent potentiometers control the X and Y steering currents supplied to these coils. In the construction of our apparatus, these deflection coils are used primarily to align the beam with the pulser aperture (discussed in the following section). When the pulser is not in use, these coils provide the only means of beam position adjustment.

The controller also provides a beam blanking function. This feature allows low-frequency modulation of the beam ($\sim$ 10 Hz) or temporary beam shutdown when not actively collecting data. This method is preferable for short periods of inactivity ($\sim$ 1 hr), when the beam can be blanked and quickly brought back, as an alternative to shutting down the system. Documentation of the blanking mechanism is limited; however, discussion with STAIB staff indicates that blanking is achieved by defocusing the beam at the source, thereby preventing downstream transmission.

For measurements reported in this work, the optimal operating parameters were: grid setting 2.80, focus setting 3.04, filament current 3.25 A, and beam energy 20 keV. To ensure proper transmission through the pulser and alignment with the Faraday cup, the X and Y deflection coil settings were 5.14 and 5.12 divisions, respectively. Table 3.1 is a reference for these values that can easily be found for later use. These values, once set, will be roughly the same day to day, and do not need changed. However, if the environment around the beam is disturbed by adding magnets or moving equipment, this may slightly deflect the beam, and you would need to find a new baseline for coupling into the Faraday cup. A detailed operating procedure and factory-recommended filament settings are provided in Appendix B.

Energy [kV]	Filament Current [A]	Focus [div.]	X-deflection [div.]	Y-deflection [div]
20.0	3.25	3.04	5.14	5.12

Table 3.1: Normal operating parameters of electron beam.

3.1.2 Electron beam pulser

The electron source described above provides a CW beam that can be modulated by blanking at repetition rates $<$ 10 Hz. The e-beam pulser enables faster modulation (up to 1 MHz) enabling lock-in detection, and was installed onto the vacuum system to improve e-beam measurements in the presence of charging of the chamber.

The pulser is a commercial component manufactured by STAIB Instruments. Fig. 3.4

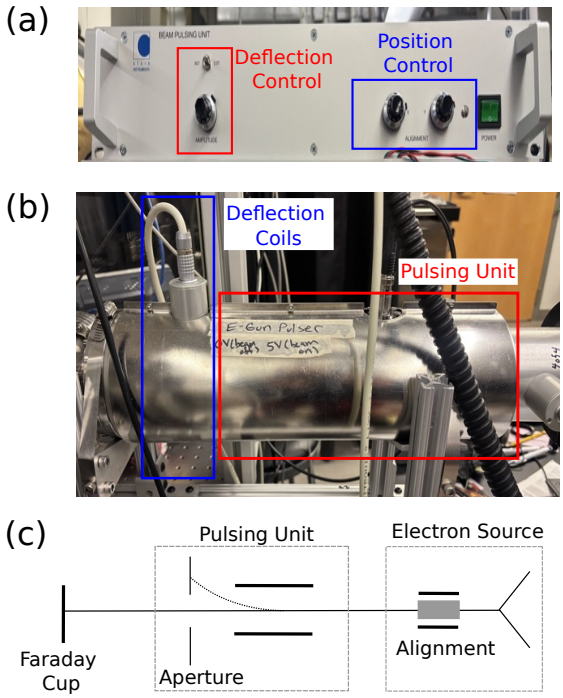

Figure 3.4: Overview of electron beam pulser. (a) Pulser control box. (b) Pulser unit installed on beamline. (c) Diagram of how the pulser works to quickly modulate the electron beam.

(a-b) shows the rack-mountable control box and the pulsing unit installed on the beamline, respectively. The device is designed to produce short, uniform electron pulses from the continuous beam generated by the source. Pulses are controlled by an external function generator connected to the pulser unit with a BNC cable, with 0 V corresponding to the beam-off state and 5 V corresponding to the beam-on state.

Fig. 3.4 (c) shows the operating principle of the pulser. In the absence of an applied voltage, the internal deflection elements steer the e-beam into an aperture, preventing transmission down the beamline. When a 5 V signal is applied, the beam is allowed to pass through the aperture. The maximum beam deflection is controlled by the amplitude setting on the pulser control unit. Increasing the amplitude increases the displacement of the beam into the blocking aperture. However, larger deflection amplitudes reduce the maximum achievable pulsing frequency. Conversely, lower amplitude settings reduce the beam displacement and may result in incomplete beam extinction, and can be tuned

to gain faster pulsing speeds of the e-beam. In our experiments, we used the maximum deflection to get full beam suppression.

During operation of the pulser, we found that using minimal deflection can lead to the beam still being present in the Rb chamber when it is supposed to be blocked by the aperture. Deflection coils after the pulsing aperture allow us to steer the beam. We found that we still have a "phantom beam" that persists for some values of e-beam amplitude deflection as shown in Fig. 3.5. Here, the plots in Fig. 3.5 (a) are output voltages produced by the Faraday cup, and Fig. 3.5 (b) is the signal sent to the pulser to modulate the beam. When the e-beam is in the cup, the voltage is non-zero, and when the beam is blocked, the voltage is at zero. In this plot, the orange curve shows how the pulser should operate. When 5 V is applied to the pulser, the beam enters the Faraday cup; however, we see that in the green curve, the behavior is the exact opposite. This is because we were using minimal deflection amplitude parameters on the pulser, so if the beam was steered using the deflection coils, we could still see the beam that should have been extinguished. For a full procedure of how the pulser alignment and operation are performed, see Appendix C.

According to the manufacturer's specifications, the pulser supports modulation frequencies up to 1 MHz. In our setup, the highest observed pulsing frequency is on the order of ~ 100 kHz when measured at the Faraday cup. This limitation arises from suboptimal coupling to the Faraday cup, which needs high gain on the current preamplifier used to measure the beam current and, therefore, a slower response to modulations of the signal.

3.1.3 Rb vacuum cell

The most unique component of the beamline is a vacuum cell that contains a dilute Rb vapor.

Fig. 3.6 shows (a) a photograph of the chamber, (b) a CAD rendering illustrating the e-beam trajectory relative to probing laser paths, and (c) a cross-sectional schematic with relevant internal dimensions. The cell body is a Kimball Physics 4-way cross that mounts directly into the beamline. To avoid loss of Rb, this is attached with differential pumping

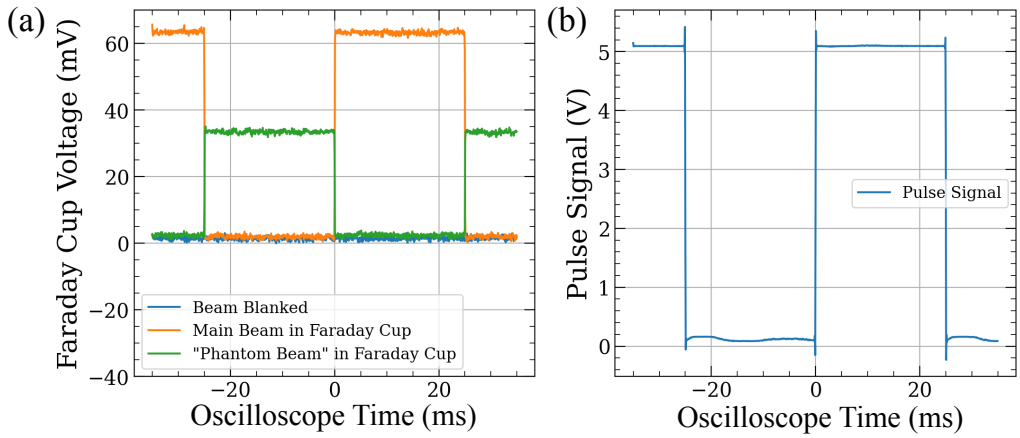

Figure 3.5: Demonstration of "phantom beam" when using the pulser. (a) Faraday cup signal of recorded voltage for when the beam is off (blue line). When the beam is in the Faraday cup (orange curve). At 5 V, the beam is allowed to pass into the Faraday cup, so the signal is high, showing that there is beam hitting the cup, and at 0 V, the beam is extinguished on top of the blue line. When the steering is large enough to see the "phantom beam" (green curve). Here, the signal is opposite to good pulser operation, where the beam enters the cup when it should not. (b) Input signal to the pulser. 5 V beam on 0 V beam off to compare what should be happening at the oscilloscope.

connectors that go from 2.7 in ConFlat (CF) flange to a 1.33 in CF flange. We found out later that Rb tends to coat the inside of the vacuum chamber and not move along the beamline, so this is not really needed, but it was part of the original design. The chamber also has two gate valves, one before the chamber controlled with compressed air, and another after that is manually turned so the Rb chamber can be isolated from the rest of the vacuum system. This isolation provided protection to the Rb during power outages, where these valves should be shut, and isolation for operations to other vacuum components without compromising the Rb in the chamber. If the Rb is exposed to air, it will completely oxidize, rendering it useless for experiments.

Two large viewports provide primary optical access to the inside of the chamber. We mount Thorlabs high-vacuum flange windows to these viewports, allowing for the transmission of interrogating laser beams. The windows are coated to minimize loss near 480 nm light. We use non-magnetic hardware (brass screws) near the beam to limit stray magnetic fields that may steer the beam, and rubber gaskets for vacuum sealing.

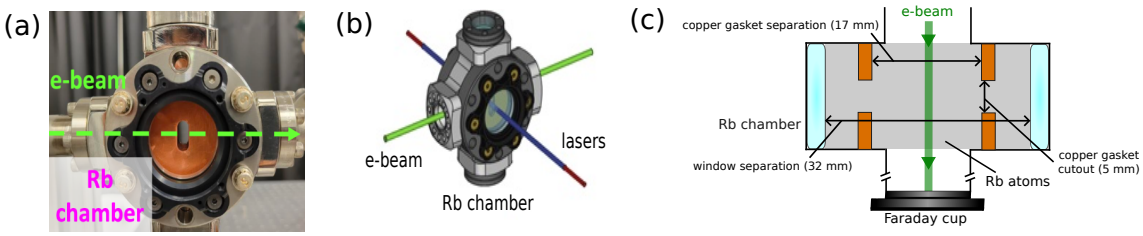

Figure 3.6: Rb vacuum chamber. (a) Image of the Rb chamber on the beamline. (b) CAD rendering of Rb chamber to show path of electron beam and optical laser path. (c) Cross-section of Rb chamber to give dimensions.

Rb is supplied by a 1 g ampule placed at the bottom of the chamber. We control the Rb vapor density by heating the chamber in a plastic-insulated enclosure (i.e. oven) with hot airflow. Air from the building is at 100 psi, so a pressure regulator takes this down to ∼60 psi. Fig. 3.7 (a) shows the heating contraption that takes this lower-pressure air to deliver heat to the Rb chamber. The air passes through a flow controller, producing a constant stream of low-flow rate air. This low-flow rate air then passes through a metal bar that is wrapped with heating tape connected to a variable voltage power supply (Variac) to make it hot. Once the Rb pressure is set, and the chamber is at a desired temperature, you basically never touch this. Fig. 3.7 (b) shows the oven. The connector for the hot air flow is made of a plastic that does not melt at high temperatures, and there is a magnetic shield of mu metal within the walls cut to fit on the inside.

The design of this cell was guided by two major factors. First, the sensing volume, the region where the lasers overlap with the electron beam, was designed to be as compact as possible to maximize the signal that the electron beam contributes to the overall laser transmission (to minimize the area where the lasers do not interact with the e-beam). We found later that this was not necessary for the fluorescence based detection, but this was the consideration before we started doing fluorescence measurements. Second, we aimed to reduce stray electric fields and charging effects that were significant in an earlier all-glass version of the cell.

To mitigate charging in this design, we added blank copper gaskets in front of the windows, with small apertures for laser access. The intent was for the copper to act as a

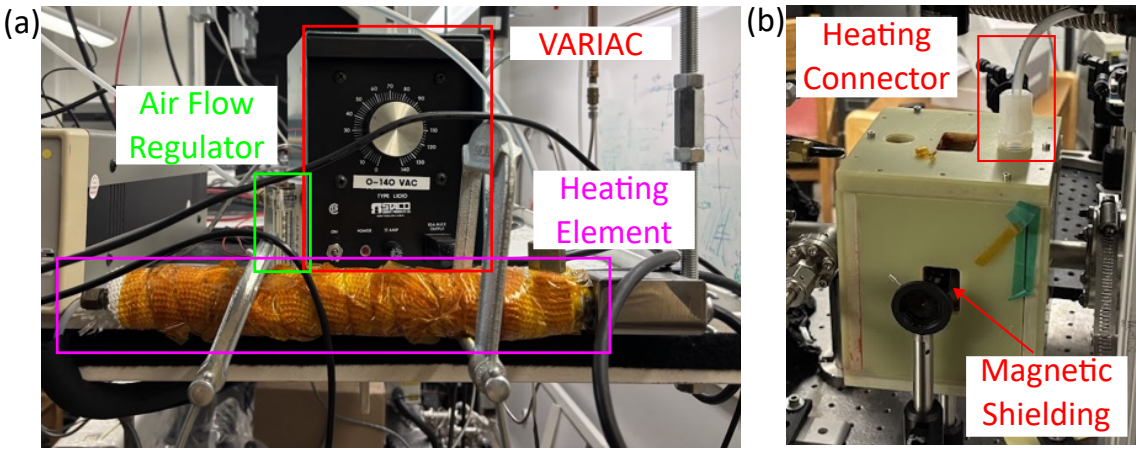

Figure 3.7: Heating elements for Rb chamber. (a) Heat delivery mechanism. The air flow regulator sets how much air can flow through the tube. The heating element is a metal pipe wrapped in heating tape controlled by the variac power supply. Once the desired air flow and heat are set, you never really have to touch this setup. (b) Heater box placed around the Rb Chamber. The heating connector takes output from the heating delivery mechanism. Inside the plastic box/oven, there is a metallic shielding against magnetic fields.

local electrostatic shield; however, in practice, this did not fully eliminate spurious charging. As we will discuss later, the blue laser involved in EIT excitation contributes to photo-charging of the glass. A more robust charge mitigation strategy is to place windows farther from the sensing volume and use ITO-coated, electrically conductive windows that can be grounded. After the e-beam experiments reported in this dissertation, I upgraded the chamber to incorporate both of these changes. This reduced the effect of stray charging that we were seeing in fluorescence measurements, and we will discuss this more in Chapter 4.2 when we describe fluorescence measurements of electric fields.

3.2 Electron beam diagnostics

Accurate characterization of the e-beam in our experimental apparatus requires both diagnostics of the beam profile and current. A wide range of diagnostic techniques have been developed for accelerator-based experiments, and in this work, we employ some of these methods to monitor the relevant beam parameters. The beam profile is measured using optical transition radiation (OTR) [90, 91] and incoherent electron-induced impact

fluorescence imaging [92, 93]. The relative beam current is measured at the beam dump using a Faraday cup and along the beamline using an integrated current transformer. Although these diagnostic techniques are well established, a detailed understanding of their implementation and limitations in our apparatus is essential. In particular, the measurement approach directly influences the interpretations of systematic effects and informs the experimental uncertainties discussed in subsequent chapters.

3.2.1 Optical Transition Radiation (OTR)

Optical transition radiation (OTR) is a method for monitoring beam shape by looking at the emitted radiation when the beam strikes a metallic screen. OTR beam diagnostics are well established for both relativistic and non-relativistic charged particle beams in accelerators. When implemented with properly calibrated materials and well-defined observation angles, OTR can provide two-dimensional beam imaging and serve as an indirect beam current monitor [91].

OTR works by a charged particle beam striking a screen (typically a metallic surface). The beam generates electromagnetic fields because it is a moving stream of charged particles. When it comes close to the metallic surface, the electrostatic boundary condition between the beam and metal must be satisfied. The only way this can happen is that there is a generated field in the optical frequency range which is monitored by a camera [94].

Our apparatus employs OTR solely as a two-dimensional beam imaging diagnostic. Fig. 3.8 (a) shows the OTR setup along the beamline. The OTR screen is housed in a four-way cross with optical access, positioned downstream of the pulser deflection coils. The OTR screen itself is a piece of copper mounted on a rotatable vacuum flange. The plate has a known horizontal length of 1.5 cm, and alignment markers (a “+" sign and a circle) etched onto its surface to assist with camera focusing at the plane of the screen. During operation, the plate is rotated into the beam path such that it is visible through the window on the four-way cross. The camera observes the screen through leaded glass, which provides radiation shielding while maintaining optical access.

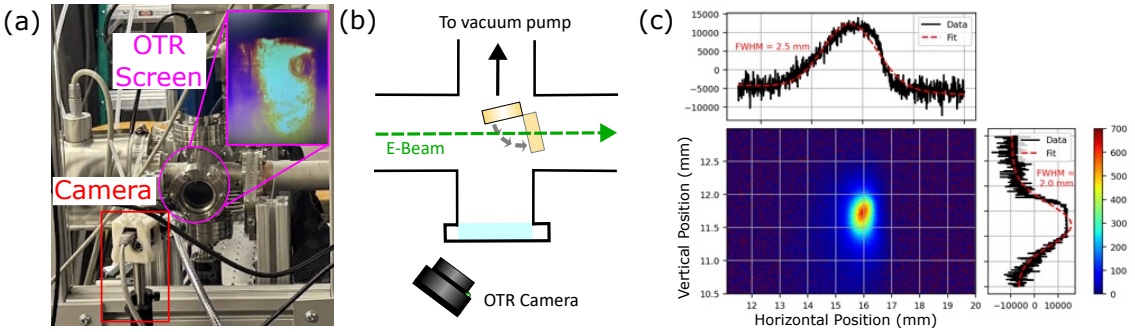

Figure 3.8: OTR overview. (a) Camera setup for monitoring the OTR screen in the vacuum setup. (b) Diagram of how the camera looks into the four-way cross. The OTR screen is recessed from the center of the cross, so to view the screen, the camera has to be at an angle to see where the beam hits the screen. (c) E-beam OTR plot. The heatmap plot shows the two-dimensional beam profile, and black lines are the sum in horizontal and vertical dimensions. Fit lines are a Gaussian fit to extract the full-width at half-maximum for each direction.

For optimal OTR collection, the screen is typically oriented at 45 degrees with respect to the e-beam propagation axis. However, as seen in Fig. 3.8 (b), in our setup, the screen is offset from the center of the flange to accommodate a larger beam steering range. Consequently, the camera cannot view the screen directly when it is along the central axis of the window. Instead, the plate is tilted to intercept the beam while remaining fully visible to the camera at an angle. The known horizontal dimension of the plate is used to calibrate the spatial scale in the horizontal direction and determine the screen angle.

Fig. 3.8 (c) shows a representative OTR image. The heatmap corresponds to the two-dimensional beam intensity distribution recorded by the camera. To estimate the beam size, the image is projected onto the horizontal and vertical axes, producing one-dimensional intensity profiles. Each profile is fit with a Gaussian to extract the full width at half maximum (FWHM) in both directions. Using this diagnostic, we calibrated the vertical and horizontal deflection response of the pulser coils and identified optimal beam-shaping parameters for a given emission current.

Focusing the beam on the OTR screen follows this procedure. First, set the desired filament heating current. This sets the limit on the maximum achievable emission current, and should always be at the maximum 3.25 A. Next, adjust the grid voltage for the target

emission current. For any emission current, there is an optimal grid voltage and focus for minimal beam size. Fig. 3.9 shows the effects of different grid voltage and focusing parameters on beam shape. For illustrative purposes, it shows three different grid voltages (A, B, and C), which correspond to different emission currents from the e-beam controller. These do not correspond to any particular grid voltage settings, but serve as some illustrative regimes.

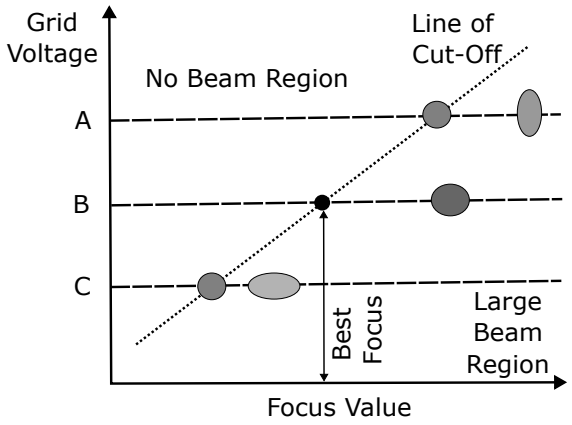

Figure 3.9: Graph demonstrating the relationship between focus value and grid voltage with electron source controller. There will be combinations of these parameters that do not allow for an electron beam to form, and for each grid voltage set (A, B, C), there is an optimal focus value for beam size.

In all cases, there is a region where there is no beam for low focus values. Much like the beam blanking options, the beam will become so de-focused that it does not travel down the vacuum chamber. As the focus value increases, there is a beam threshold that is marked by the cut-off line. In cases A and C, increasing the focus value beyond this cutoff for sub-optimal grid voltages will elongate the beam in one direction. In case B, there is a minimum achievable spot size marked by the black dot. At this optimal grid voltage, for increasing focus parameters, it will make the beam larger in all directions, and not elongate the beam like in other sub-optimal grid configurations. The minimal spot size of the e-beam is the goal of focusing on the OTR screen, and this shows that it is a balance of all parameters from filament current, grid voltage, and focus control.

The emission source is designed for an operational working distance of 445 mm, yielding

a nominal beam spot size of approximately 1 mm at the focal region. It is important to note that this OTR screen is not where we do our measurements. Therefore, OTR is useful for initially shaping and monitoring the beam, but it does not give us an in-situ beam profile.

3.2.2 Incoherent Rb impact fluorescence

As a second method to monitor beam shape, we image incoherent electron impact-induced fluorescence of Rb vapor. In this approach, electrons collide with Rb atoms, which are excited and then decay, producing broadband fluorescence that can be collected with a camera.

Impact fluorescence profiling is more commonly performed by introducing a high density of gas, such as helium, into the vacuum chamber that boosts the impact fluorescence signal through increased interactions. In our apparatus, the Rb density is sufficient that with a high quantum efficiency camera and long exposure time, we can resolve the e-beam's one-dimensional intensity profile through the viewport at the top of the Rb chamber. Specifically, we use a 10 s exposure time and average over 5 frames with a high quantum efficiency camera. This long exposure time means that there are not a lot of impacted Rb atoms, and doing this measurement with lower quantum efficiency camera needed collection of light for $\sim$ 15 mins.

Fig. 3.10 (a) shows the imaging setup. A PIXIS 1024 camera is placed above the vacuum chamber with a 50 mm focal length lens to image the plane of the 780 nm probe laser fluorescence in the Rb chamber. Because the camera sensor is sensitive to background light in the room, we add an IR filter and surround the camera with light-tight foil. We then align the e-beam to the lasers by monitoring the non-linear magneto-optical rotation signal of the 780 nm transmission with a photodiode [95]. Once the imaging system is in focus and the e-beam is aligned through the system, we record impact fluorescence images as shown in Fig. 3.10 (b). The bright red column corresponds to the e-beam trajectory through the vapor. Compared with OTR imaging (a spot on a single plane), impact

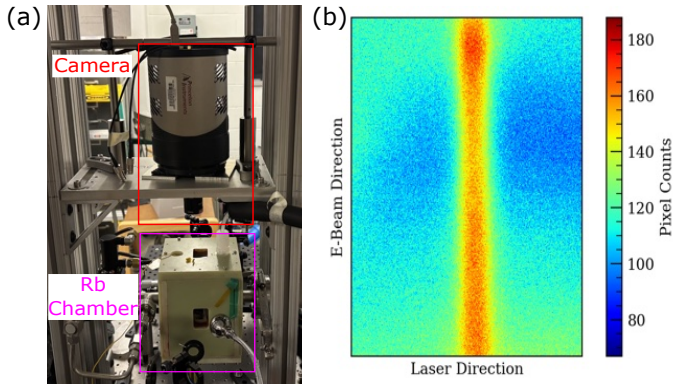

Figure 3.10: Overview of impact fluorescence measurements. (a) Experimental setup of the camera looking at the impact fluorescence region in the Rb chamber. (b) Recorded impact fluorescence measurement of the electron beam.

fluorescence is useful for visualizing the beam along its propagation axis and at the right location.

3.2.3 E-Beam current diagnostics

The Faraday cup in our system is a Kimball Physics FC-73, and is the main beam current diagnostic for our system. A major drawback of our apparatus is that we cannot measure the current at the location of the Rb chamber. As such, the post-chamber Faraday cup is our best way to measure the current compared to the emission current reading on the e-beam controller. This makes us rely mostly on "remote" measurements of beam current.

The operating principle of a Faraday cup is that electrons are collected by a conductive cup, and the resulting charge flow is measured as a current proportional to the incident electron flux. The Faraday cup has a 5 mm aperture. The cup current is amplified with a Stanford Research Systems SR570 low-noise current preamplifier, converting current to a voltage that is monitored on an oscilloscope. Fig. 3.11 (a) shows the installed cup and the electrical feedthrough used for readout. The Faraday cup assembly also includes bias grids intended to suppress secondary electron emission and improve charge collection. We do not use these grids in our experiments to avoid introducing additional charged surfaces and stray fields near the laser-interaction region.

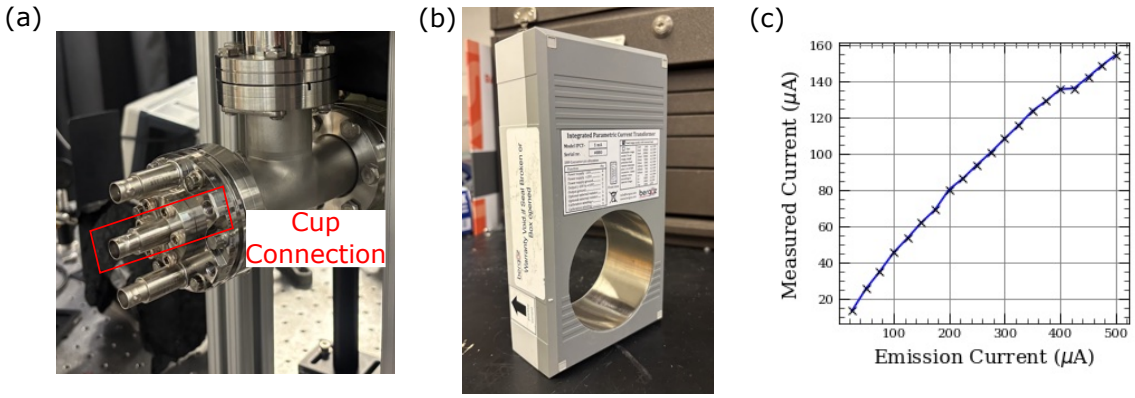

Figure 3.11: Current sensing devices and measured currents. (a) Faraday cup installed on the vacuum system with a highlighted connector for readout. (b) IPCT current monitor device. (c) Measured e-beam current vs. emission current. These measurements are from the Faraday cup, but both devices deliver the same current.

In our system, the Faraday cup current is consistently lower than the emission current reported by the electron gun controller. Fig. 3.11 (c) quantifies this discrepancy. Although the measured current increases linearly with the reported emission current, only about $\sim 30\%$ of the emission current is collected at the Faraday cup.

As a secondary current diagnostic, we use an integrated parametric current transformer (IPCT) to measure the beam current along the beamline [Fig. 3.11 (b)]. The IPCT is placed around the vacuum tube and works based on dc current transformer technology developed at CERN [96]. This fluxgate sensor detects the magnetic field produced by the beam current through electronic compensation coils that null the flux through the sensor. The corresponding output signal is proportional to the current passed through the IPCT opening.

When installed on this apparatus near the Faraday cup, the IPCT agrees with the Faraday cup readout. However, when the IPCT was installed closer to the electron emission source (on another e-beam apparatus), it instead agreed more closely with the emission current output of the controller. These measurements support the conclusion that the beam in our apparatus is clipped along the beamline before it makes it to the Faraday cup. It is still a question if this is due to clipping along the beamline, poor coupling

into the Faraday cup, or clipping at the pulser aperture. For future vacuum chamber constructions, it is important to know that the beam can be clipped along the beam path, and it should be as open as possible so this does not happen.

In addition to these quantitative diagnostics, both impact fluorescence and OTR depend on beam current. In principle, this allows the image brightness to be calibrated against the e-beam emission current readout on the controller. This provides a quantitative proxy for current, in addition to imaging beam size. Fig. 3.12 shows the change in signal for both methods as the emission current is varied. For the OTR images Fig. 3.12 (a), all the spot sizes look exactly the same, meaning that we are at an optimal focusing point, but the cross-sectional graph shows a Gaussian profile increasing in amplitude for increasing emission current. The same holds true for the impact fluorescence measurements in Fig. 3.12 (b). These measurements were taken with a lower quantum efficiency camera, so the counts are a lot lower than the PIXIS, but the cross-section still shows the trend of increasing amplitude Gaussian profile for increasing emission current.

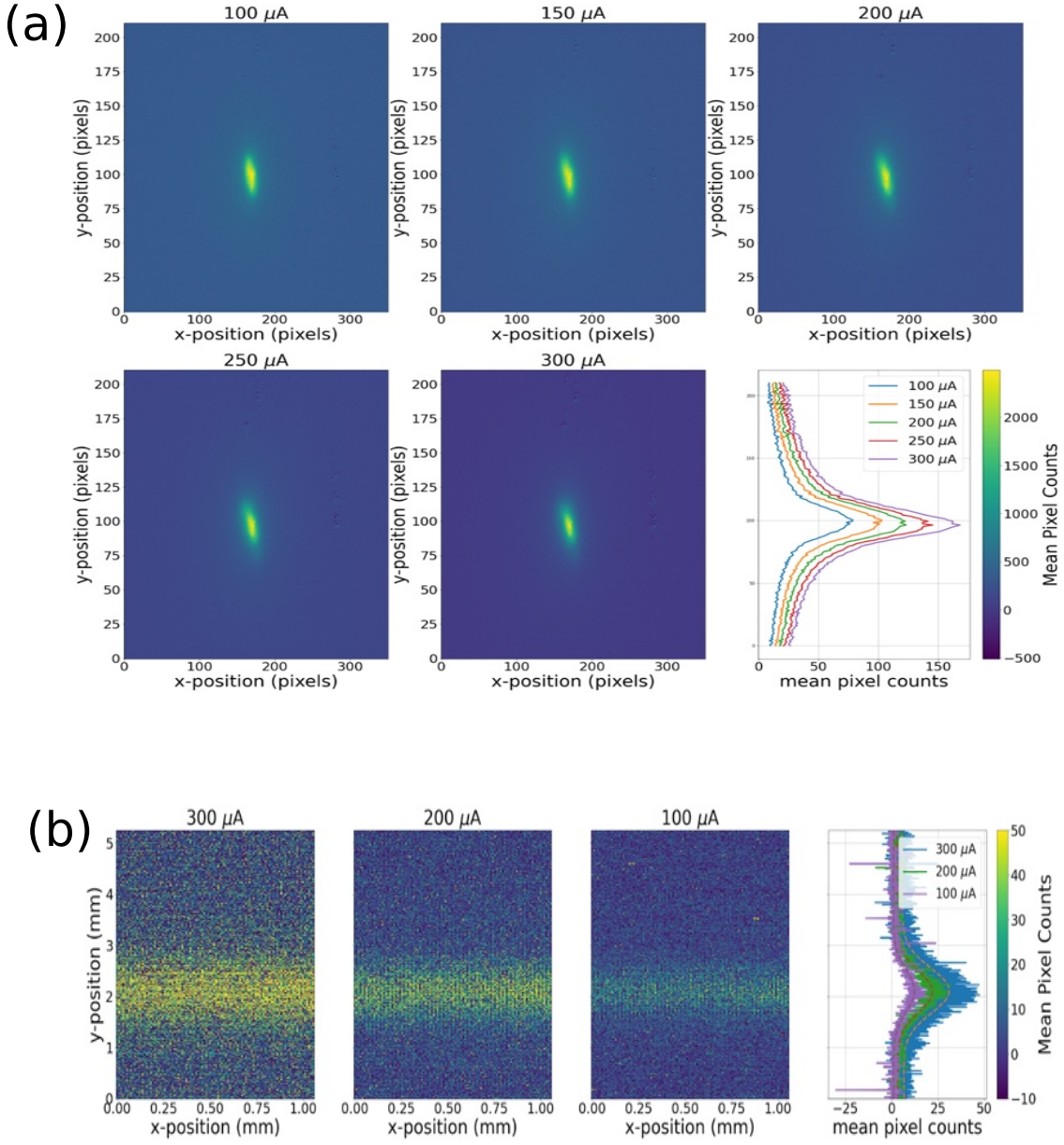

Figure 3.12: Effect of changing current on OTR and impact fluorescence measurements. (a) OTR beam spot for increasing emission current and the associated one-dimensional beam profile to show height changes with increasing current. (b) Impact fluorescence signal for decreasing emission current, and associated one-dimensional beam profile.

Chapter 4

Fluorescence-based electron beam measurements

4.1 Introduction

Electron beams are broadly used across science, industry, and medicine for imaging, microscopy, materials processing, welding, lithography, radiation generation, and high-energy particle acceleration, thanks to their ability to deliver precisely controlled, high-energy streams of electrons. As a result, there has been an increasing demand for more robust non-invasive beam property diagnostics.

A variety of diagnostic techniques have been developed to measure beam profiles and currents. Optical and imaging methods based on signals such as impact fluorescence (IF) [92, 93], synchrotron radiation [97], and X-rays generated by moving particles [90] have played an essential role in accelerator research and beam operations. However, each of these beam diagnostics also bears some intrinsic drawbacks, and their applicability is often limited by factors such as sensitivity and system complexity. For example, synchrotron radiation only exists near particle trajectory-bending components [97, 98], Compton scattering laser wire requires high laser intensity and slow scanning between particle and laser beams [99, 100], and the gas-ionization-based 2D gas curtain devices rely on complex

mechanical systems and have low sensitivity [101, 102].

In this Chapter, we describe a proof-of-principle experiment demonstrating an atom-based, minimally invasive method for measuring an e-beam's width, centroid position, and current in a single measurement of the e-beam's electric field. Sections from this Chapter are adapted from previously published work [103, 104].

4.2 Fluorescence measurements of electric fields

Our detection scheme relies on fluorescence measurements of atomic populations in Rb. The method combines LIF-dip used to observe electric fields in plasmas [49, 71, 105–107] with EIT [1, 26–28, 31, 83, 108].

In this experiment, the Rb atoms are excited to a coherent superposition of the ground and Rydberg state using two laser fields: a near-infrared probe field, resonant with the $5S_{1/2} \rightarrow 5P_{3/2}$ optical transition (wavelength 780 nm 5 μW), and a 480 nm blue control field (70 mW) that couples the intermediate $5P_{3/2}$ state with the desired Rydberg state (in this experiment $58D_{5/2}$). The probe and control field are collimated to similar beam waists (0.33 mm full width at half maximum (FWHM)) and have the same linear polarization.

Recall that in Chapter 2, we describe the interaction of light fields with atoms. Specifically, in Fig. 2.3 the excited state population diminishes when the sum of the laser frequencies matches the frequency difference between the ground and Rydberg states. Monitoring the probe laser transmission has been done to spatially map electric fields in the past [35, 109], but this coherent fluorescence-based imaging technique [56, 103, 110] provides finer spatial resolution across the atomic sensing volume.

Fig. 4.1 illustrates the main concept of the fluorescence-based detection scheme. A camera monitors the fluorescence of the atoms decaying from the $5P_{3/2}$ state. We collect images at a fixed frame rate while the coupling laser sweeps across the Rydberg atomic resonance. These images are then used to create spectroscopy curves for position along the Δz laser position axis. As the electric field changes, the recorded spectra have resolved

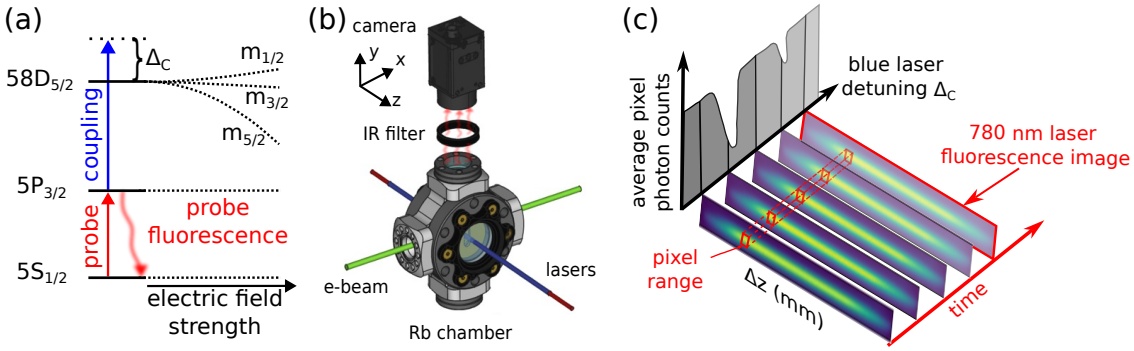

Figure 4.1: (a) Three level atomic system with relevant atomic transitions, and illustrating probe laser fluorescence of the $5P_{3/2}$ state. (b) Experimental setup of the camera monitoring the probe laser fluorescence in the Rb chamber. (c) Fluorescence detection method. The 780 nm probe laser excites Rb atoms in the Rb chamber which fluoresce and are imaged by a camera. The 480 nm coupling laser is frequency scanned around the Rydberg atomic resonance, and we capture images of the probe laser fluorescence in time. The pixels that contain the probe laser are averaged and an average pixel photon count is extracted for each point in time and position along the Δz position axis. At each position, the measured atomic spectra will be different depending on the strength of the electric field in space.

peaks where the frequency separation of the peaks is related to the strength of the electric field.

For our specific experiment, we use the same PIXIS 1024 camera with a 50 mm lens focused on the probe laser as described in Chapter 3.2.2. We collect images with 60 ms exposure time for 600 frames while the coupling laser sweeps across the 58D Rydberg state for 300 s and is triggered to the sweep of the blue laser. We use the known frequency separation of the $58D_{5/2}$ and $58D_{3/2}$ Rydberg states [4] to calibrate the frequency axis from the acquired frames.

For a demonstration of how this works, we measure electric fields generated by the blue laser on the windows of the Rb chamber. Fig. 4.2 (a) shows recorded spectra at different spatial locations along the interaction volume in the Rb chamber. In each of these locations, the electric field is different, and therefore, the shape of the recorded resonance changes. Fig. 4.2 (b) shows stacks these atomic spectra spatially to show the corresponding change of electric field over the interaction volume displacement. Recall that in the construction of our Rb chamber in Fig. 3.6 (c), there are grounded copper gaskets

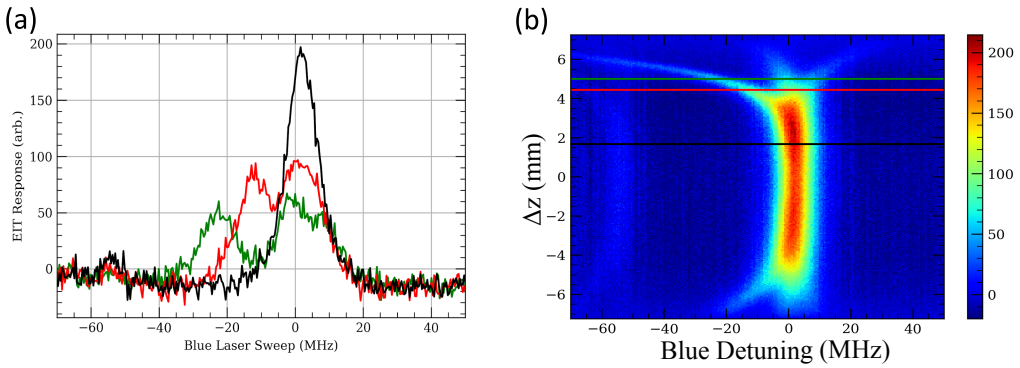

Figure 4.2: Fluorescence spectra with no e-beam. (a) Reconstructed spectra at three locations along the cell position. One near the window where the resonances are clearly split (green), one closer to the center showing the change in electric field (red), and finally one near the center of the cell where the electric field is near zero (black). (b) Fluorescence heat map. Recorded spectra plotted along the cell positions.

whose role is to attenuate possible electric charge buildup on the fused silica chamber windows from scattered electrons or photoelectrons produced by the blue laser [56, 109]. The absence of stray charging should manifest itself as narrow EIT peaks along the entire interaction volume. However, in Fig. 4.2 (b), we observe a large splitting of the EIT peak near the windows at the ± 6 mm Δz positions (positions along the laser propagation axis direction where $\Delta z = 0$ mm is the center of the observed volume), indicative of residual spurious charging. We can clearly see that our charge mitigation did not work, and there is charging along the interaction volume.

To mitigate this charging, after experiments presented here concluded, we installed indium tin oxide (ITO), a transparent electrically conductive coating, on the Rb chamber and moved the window surfaces further from the center of the cross with vacuum spacers as mentioned at the end of Chapter 3.1.3. Fig. 4.3 (a) is the recorded fluorescence spectra before the installation of ITO coated windows and Fig. 4.3 (b) is the recorded spectra after they were installed. ITO windows mitigate charging near the 6 mm cell position mark as indicated by a narrow fluorescence peak at that location. This creates a cleaner electrostatic environment for measurements and increases the effective sensing volume that is useful for e-beam measurements.

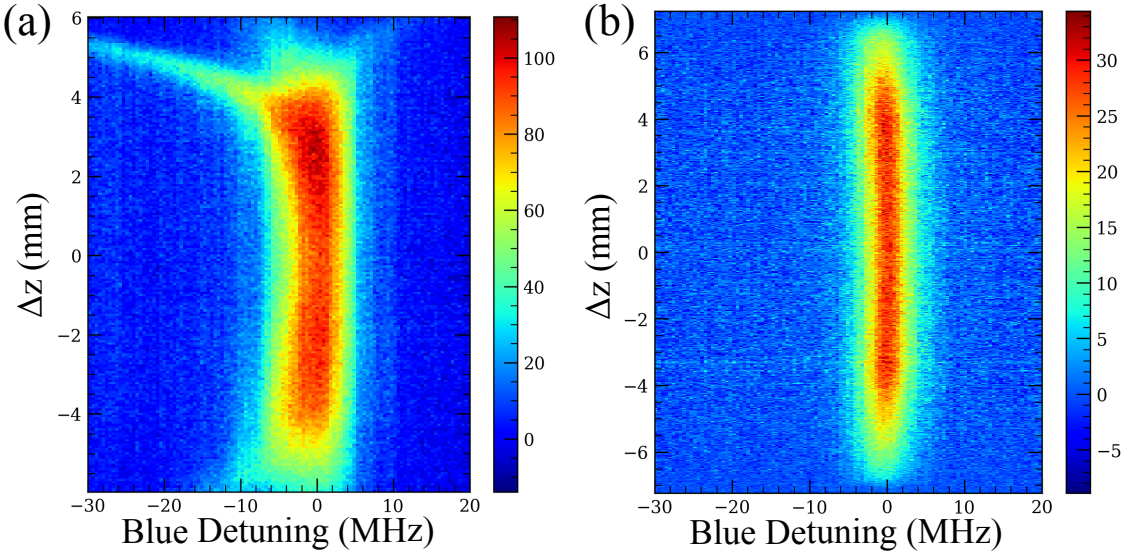

Figure 4.3: Effect of ITO coating on windows for cell charging. (a) Recorded fluorescence spectra in Rb chamber with copper plates. There is a clear splitting of EIT resonances around the 6 mm cell position. (b) Recorded fluorescence spectra in Rb chamber with ITO coated windows and charged surfaces moved further away. There is a narrow EIT line with no splitting along the entire cell position path.

4.3 Theoretical modeling of expected electric field produced by the electron beam

With this parasitic background signal in mind, it is important to have an estimate of what the electric field produced by the electron beam should be, so we can see characteristic behavior in the recorded spectra. Fig. 4.4 (a) shows a radially symmetric electric field distribution, produced by an e-beam assuming a Gaussian beam profile. The charge distribution $\rho(r)$ of electrons assuming this form is:

$$\rho(r) = \frac{I}{v_e \pi \sigma^2} e^{-\frac{r}{\sigma^2}}, \tag{4.1}$$

where I is the beam current, v_e is the electron speed that is related to the beam energy V, mass of the electron m_e and electron charge e as $v_e = \sqrt{\frac{2eV}{m_e}}$, and σ is related to the width of the beam as FWHM $= 2\sigma\sqrt{\ln(2)}$. We define r, the radial position away from the e-beam

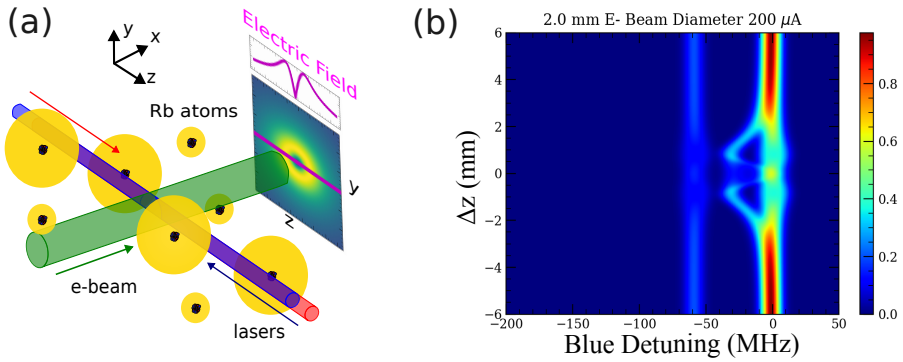

Figure 4.4: Electric field produced by an electron beam. (a) Overview of experiment. A charged particle beam produces an electric field and passes through a cloud of Rb atoms shown as a nucleus with a yellow electron cloud. We use lasers to excite these atoms to a Rydberg state (shown as atoms with a larger electron cloud) to probe the electric field. We assume the beam produces a radially symmetric Gaussian electric field distribution described by Eq.(4.3). (b) Expected fluorescence spectra of e-beam for given parameters simulated from Gaussian distribution e-beam and simple shifted peaks.

center as, $r = \sqrt{(\Delta z - z_0)^2 + (\Delta y - y_0)^2}$ where z_0 and y_0 are the displacement along the z- and y-direction, respectively. Using this radially dependent charge distribution, we can solve for an enclosed charge (q_{enc}):

$$q_{enc} = \int_0^{r'} \int_0^{2\pi} \int_0^{l} \rho(r) r dr d\phi dl = \frac{lI}{v_e}(1 - e^{-r^2/\sigma^2}). \tag{4.2}$$

Where l is the dimensional length of a cylindrical Gaussian surface around the e-beam. Then, using Gauss's law, we can solve for a radially dependent electric field

$$E(r)A(r) = \frac{q_{enc}}{\varepsilon_0} \tag{4.3a}$$

$$E(r) = \frac{\frac{lI}{v_e}(1 - e^{-r^2/\sigma^2})}{\varepsilon_0 2\pi r l} = \frac{I}{2\pi\varepsilon_0 v_e}\frac{1}{r}(1 - e^{-r^2/\sigma^2}). \tag{4.3b}$$

Here $A(r)$ is a Gaussian surface of a cylinder enclosing charge, and ε_0 is the permittivity of free space constant.

Now using this expression for electric field, we can simulate shifts to atomic spectra for specific beam sizes and shapes to understand what the recorded spectra should look like

as seen in Fig. 4.4 (b). This heat map shows the shifted EIT spectra for a 2 mm diameter e-beam with 200 μA current. The picture is symmetric and has a distinct two-lobe feature that corresponds to a rise, drop, and rise again in the electric field cross-section of the e-beam the lasers sample.

Recall in Chapter 2, we simplified the shape of EIT resonances to be nearly Gaussian, but shifted by values of applied electric fields Eq. 2.23. Now we extend this form to account for all sublevels in the Rydberg fine structure states, so the total EIT fluorescence spectra $\mathcal{F}$ is modeled as a combination of three Gaussian resonances:

$$\mathcal{F} = A \sum_{|m_j|} w_{|m_j|} \exp\left[\frac{-[\Delta_C - \Delta f_{|m_j|}(E)]^2}{2\gamma_{EIT}^2}\right]. \tag{4.4}$$

Here, $w_{|m_j|}$ are amplitudes for each $|m_j|$ level of the Rydberg state empirically set and constant for all fits The relative orientation of the electric field laser wave vector and polarization certainly changes the relative amplitude of various m_J resonances, in the reported experiments we used the configuration in which the resonance amplitudes were relatively insensitive to changes in the E-field direction, so it was possible to not include their variations in the fit. The dependence of polarization on different EIT sublevels will be discussed in Chapter 6. Δ_C is the coupling laser frequency detuning, γ_{EIT} is the linewidth of the EIT resonance set constant for all peaks, and $\Delta f_{|m_j|}(E)$ is the frequency shift of the Rydberg energy level described by numerically solving the Stark shift with ARC [4]. While the EIT lineshape should be Lorentzian, due to broadening of the resonances Gaussian curves describe the data well.

4.4 Electron beam measurement results

Fig. 4.5 shows an example of the recorded fluorescence spectra and resulting e-beam profile analysis. Fig. 4.5(a) shows three samples of the EIT fluorescence spectra for different positions along the laser beam path [Fig. 4.5(b)]: (1) at the region of minimal electric

field; (2) at the edge of the e-beam where its electric field is the highest; (3) near the surface of the copper blank gasket where residual charging produces a relatively strong electric field. To extract the value of the electric field at each point, we fit the recorded spectra with (4.4), where the only free parameters are the total amplitude of the EIT profile, A, and the value of electric field magnitude, E.

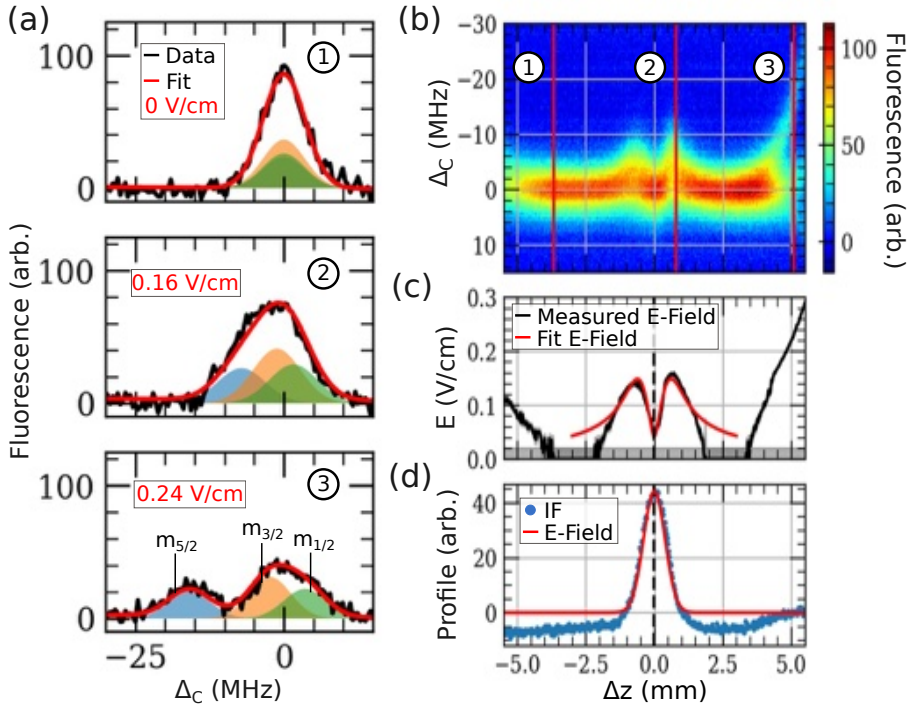

Figure 4.5: Demonstration of fluorescence based measurements of the electric field of an e-beam. (a) The EIT spectra that constitute the heat map in (b). The spectra are fit with Eq. (4.4) to determine the electric field value shown as the shaded regions in each plot. (b) The measured spectra of the $58D_{5/2}$ Rydberg EIT peak for each position along the laser beam fluorescence. The numbers correspond to the shown single spectra in (a). (c) The reconstructed electric field value along the Rb chamber. The measured field is fit with a function described by Eq. (4.3). The minimum detectable field is shown as a grey strip along the bottom of the plot, and error bars on the fit are also shown in grey. (d) E-beam profile. Impact fluorescence (IF) shows a detection method to verify where the e-beam is inside the Rb chamber, and the reconstructed profile from the E-Field measurement is plotted on top of the IF profile.

The reconstructed electric field distribution is shown in Fig. 4.5 (c). In the center, one can clearly see the characteristic two-lobed feature, expected when the laser beams go through the center of the e-beam, as shown in Fig.4.4 (a). The position and width of this feature matches well with the IF signal, shown in Fig. 4.5 (d). As discussed earlier in this

chapter, the background electric field near the edges is not directly related to the e-beam, but caused by residual charging of the cell windows and walls.

To extract the e-beam parameters, we fit the reconstructed curve with the analytical form of the radially dependent electric field in (4.3). The fit also accounts for the finite width of the laser beam and the y-deflection from the center of the e-beam. The free parameters in this fit are the e-beam width σ, e-beam current I, and the z_0 and y_0-displacement of the electron and laser beams respectively. We only fit the region of the reconstructed electric field where $|\Delta z| \leq 3$ mm because it avoids the large parasitic background field, and we found that varying this range has little effect on the reconstructed width, current and centroid position.

The reconstructed e-beam cross section is plotted on top of the IF measurement in Fig. 4.5 (d), showing excellent agreement between the two measurement methods. The e-beam FWHM is measured to be 1.07 ± 0.06 mm with the IF method and 1.1 ± 0.1 mm with the Rydberg electric field reconstruction method. The value of the width is measured from five repeated measurements with a fixed Faraday cup current of 35 μA. The uncertainty of the width measurement is the standard deviation of the reconstructed beam width and is 100 μm.

Further diagnostics of the e-beam position and current are shown in Fig. 4.6. For these measurements we either moved the e-beam [Fig. 4.6(a)] or changed its current [Fig. 4.6 (b)] and tracked the variations in the reconstructed electric field distribution. For example, if the beam position changes, the two lobes shift by the corresponding amount. To verify the accuracy of our method, we fit the reconstructed electric field with a functional form, as described above. Fig. 4.6(c) shows excellent agreement between the reconstructed beam position with that measured using the IF method.

To estimate the uncertainty of the beam position, we use the uncertainty of the fit of the electric field with Eq. 4.3. A free parameter in this equation is the centroid position of the beam, and while this might not correspond to the true center of mass of the e-beam, it gives us a metric for position. In the region of fit, there are ~ 220 points with 20 μm

spacing. If you only consider this point-like uncertainty for the beam position, this would be the associated uncertainty, but we fit the measured electric field, so the uncertainty of the center position is much smaller than the precision of the camera position. The shown uncertainties for the Rydberg EIT methods are from the error of the fit parameters, and the centroid position is known within 8 μm. Again, this is due to the amount of points in the region of interest for the e-beam position and the sharp features around the center dip in Fig. 4.5(c).

Changing the emission current seems to also slightly deform and shift the e-beam due to electron repulsion or focusing effects that we see in both electric field reconstruction [Fig. 4.6(b)] and IF measurements. Both profiles show an asymmetry that may be due to the background field present within the Rb chamber visible near the edges. Fig. 4.6(d) shows a clear linear correlation between the recorded Faraday cup current and the current values reconstructed from the electric field. The reconstructed current values are about twice larger than the measured Faraday cup current, possibly due to the e-beam clipping somewhere in the beamline before the Faraday cup. Further verification requires accurate *in situ* e-beam current measurements using, e.g., a co-located harp scanner.

In this experiment, the smallest measurable electric field value is limited by the smallest detectable shift. We can estimate it as $\simeq \gamma_{EIT}/(SNR\sqrt{n}) = 0.1$ MHz [111, 112], where $SNR \approx 20$ is the signal to noise ratio (defined as a ratio between EIT resonance amplitude and the standard deviation in each frequency bin), and $n \approx 90$ is the number of data points within the linewidth of a recorded resonance. This corresponds to a minimum detectable electric field of $E_{min} \approx 0.02$ V/cm, which matches our more thorough statistical analysis with simulated data of similar SNR. The precision of the reconstructed electric field value improves for higher electric field, because of the non-linear Stark shift dependence on applied field, and at field values around 0.1 V/cm the precision is < 0.01 V/cm. We note that to achieve this precision, it is crucial to link resonance shifts via the Stark splitting model (rather than fitting them independently) and to keep fixed widths and amplitudes of contributing resonances.

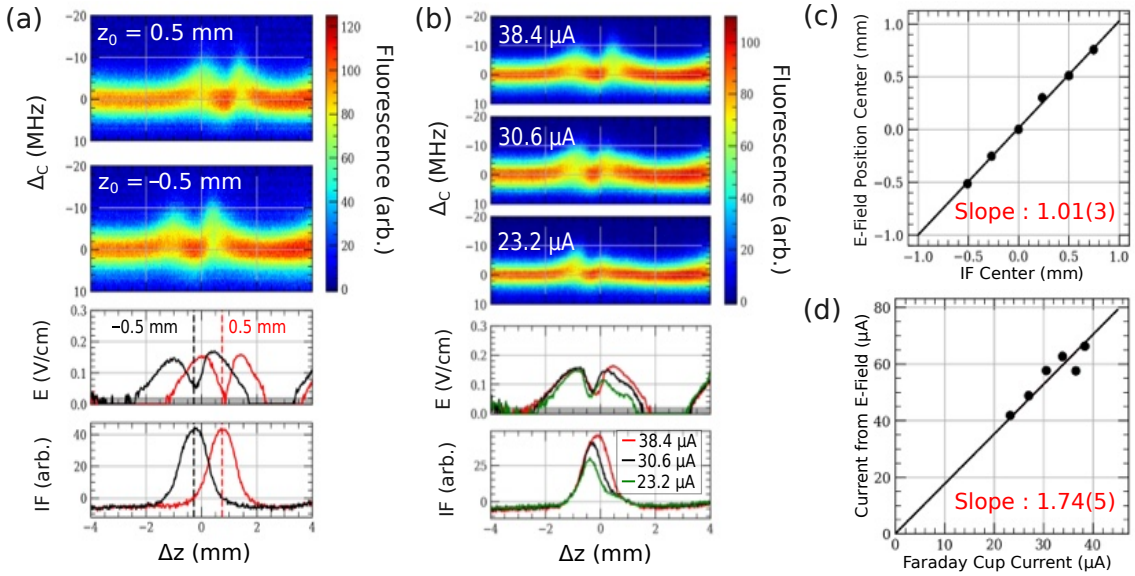

Figure 4.6: E-beam diagnostics for position and current. (a) and (b) are the same style of plots shown in Fig. 4.5 (b)-(d). (a) Heat maps for two different e-beam positions in the cell. The dashed lines in the plots show the beam center. (b) Plots of heat maps for increasing e-beam current. Current values recorded from the Faraday cup. (c) Diagnostic of e-beam position in the Rb chamber. Error bars on the plot are derived from uncertainty of the fit and smaller than the points on the graph. (d) Fit of recovered Rydberg current vs. Faraday cup current. Error bars on the plot are derived from uncertainty of the fit and smaller than the points on the graph.

Since our current approach is only sensitive to the absolute value of the electric field, our current fit model does not take into account the direction of the electric field, and its influence on the shifts and transition amplitudes of the different $|m_j|$ levels of the Rydberg state. We also note that magnetic fields can distort the EIT resonance [55], but we have shielding for ambient magnetic fields and the magnetic field produced by the e-beam is small compared to what is needed to modify the resonance [95]. In addition, presence of the background electric field can produce additional systematic error in beam reconstruction due to its unknown direction. More accurate current measurements requires improvement of the Rb vapor chamber design to further reduce the parasitic charging.

4.5 Summary

To summarize this Chapter, we apply Rydberg fluorescence-based detection to measure spatially varying dc electric fields produced by an e-beam and to reconstruct the center-of-mass beam position to within 8 μm, determine the beam width to within 100 μm, and measure the beam current in a simultaneous measurement. We expect this technique to be useful for diagnostics of charged particle beams of any energy, and for diagnostics of charged particles in general, such as in low-density plasmas [49, 68, 71, 105–107, 113]. Further diagnostics such as full beam cross-sectional profiling can be achieved using sheet laser beams [103, 110], especially if the full electric field vector is reconstructed [57, 58]. The detection speed can be improved by using a faster higher dynamic range camera or an array of spatially separated Rydberg atom clusters to study the temporal dynamics of electron beams [114].

Chapter 5

Transmission-based electron beam measurements

5.1 Introduction

Spatial field reconstruction can be efficiently performed by imaging the EIT-induced changes with fluorescence as discussed in the previous Chapter. However, fluorescence requires additional optical access for measurements and has a limited detection speed imposed by the camera. In this Chapter we explore an alternative approach for a two dimensional spatial electric field mapping technique that is based on transmission of light through the Rb chamber for a non-collinear EIT geometry. The general concept of the detection principle is the same as before where the electric field produced by the electron beam generates a Stark shift of the energy of a targeted Rydberg state.

In this experiment instead of using traditional counter-propagating optical fields, we introduced a small angle between them to reduce the electric field sensing volume which is constrained by the beam overlapping region. A drawback of this method is increased Doppler broadening of EIT resonances [87] leading to lower electric field sensitivity. Nevertheless, by rastering the two dimensional detection space, we are able to reconstruct the profile of the e-beam with sub-mm precision. The work presented in this Chapter high-

lights work that lead up to the fluorescence based measurements and the text is adapted from a previously published conference proceeding [115].

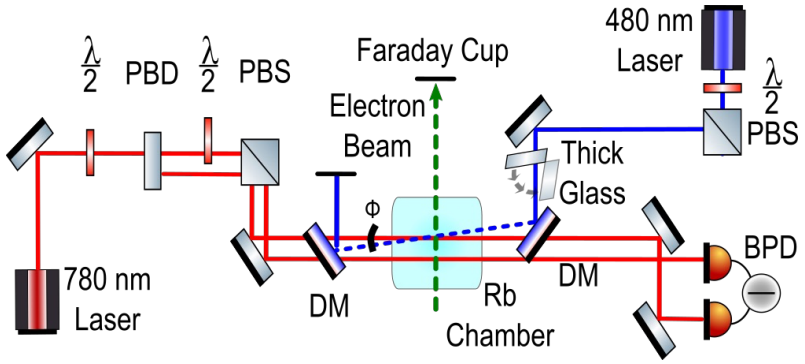

Figure 5.1: Simplified optical setup. The blue laser is at an angle ϕ with respect to the red laser. In this balanced detection scheme there are two red laser paths to cancel any changes of atomic density in the chamber. Where the blue laser crosses the red laser, this is the only region where there is EIT signal therefore creating a localized electric field measurement. The thick glass in the setup displaces the blue laser and this interaction region, so it can move along the red laser path in the Rb chamber.

5.2 Transmission based detection scheme

The general idea of the transmission based detection scheme is illustrated in Fig. 5.1. Here we have two parallel red laser beams that serve as a sensing beam and a Doppler background subtracting beam, respectively. In the sensing beam we introduce a blue laser at an angle to allow for a small region of overlap within the Rb chamber. Looking at the EIT signal, the only atoms that contribute to the measured signal are those in the overlapped beam region, therefore we can gain spatial information along the sensing volume by moving this overlap region within the chamber.

For the specifics of our sensing apparatus, we have a blue laser whose power is fixed at 60 mW and has a beam FWHM size of $\approx$ 0.2 mm. The 780 nm red laser is tuned and locked to the ^{85}Rb $5S_{1/2}$ (F=3) $\rightarrow$ $5P_{3/2}$ (F'=2,3 crossover) resonance using a saturation absorption spectroscopy reference. The red laser power is fixed at 60 μW and is split with a polarizing beam displacer into two identically polarized beams both with a FWHM of $\approx$

0.2 mm.

In the Rb chamber, the red and blue beams are crossed at an angle $\phi \approx 7°$, creating a sensing region of ≈ 5 mm. The size of this region in z- and y- dimensions is set by the laser beam cross-section. While better spatial resolution may be achieved with a larger angle between the beams ϕ, we here are limited by the opening size in the copper plates placed within the Rb chamber (see Fig. 3.6 (c)). Also, larger ϕ causes rapid broadening of EIT peaks [87], and we wanted to keep the EIT resonance width to below 100 MHz to remain sensitive to small electric fields.

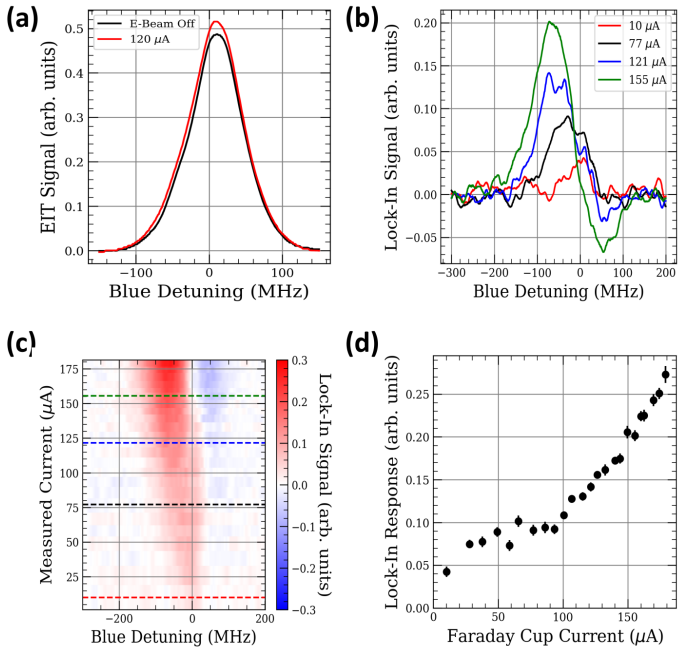

Figure 5.2: (a) EIT spectra for the case of the e-beam off and on with 120 μA total current. (b) Lock-in signal due to pulsing of the e-beam for different currents. (c) The heat map is the lock-in signal strength vs the blue laser detuning and the e-beam current. Dashed lines corresponds to the location of the lock-in curves shown (b). (d) Lock-in signal maximum value vs the e-beam current.

To measure the EIT spectra we lock the red laser and sweep the frequency of the blue laser around the 58D Rydberg resonance. Fig. 5.2 (a) shows an example of our recorded EIT spectra in to the presence of the e-beam. To overlap the e-beam and the lasers, we use polarization rotation methods to align the red laser with the e-beam as discussed in Chapter 3.2.2, and then move the blue laser until the spectra difference is maximized

between e-beam on and off cases. The frequency axis is calibrated with a separate EIT reference cell by observing a known hyperfine splitting of the $58D_{5/2}$ and $58D_{3/2}$ sublevels [4]. As shown Fig. 5.2 (a), the EIT spectra have FWHM of about 100 MHz due to the laser beams crossing at non zero angle ϕ. The electric field produced by the e-beam is inhomogeneous in the sensing region and not strong enough to visibly split the 100 MHz wide spectral line, like in the fluorescence measurement experiment. Consequently, the e-beam produces some reshaping of the EIT spectrum, shown for comparison for the e-beam on and off in Fig. 5.2 (a). For small e-beam current this reshaping is hardly noticeable, and can be further distorted by parasitic electric fields inside the chamber.

To get a signal that is only dependent on the presence of the e-beam, the solution is to pulse the e-beam on and off at 5 kHz modulation frequency and performed lock-in detection. We found that this pulse speed allowed for minimal charging of the chamber and strong response from the e-beam discussed in Appendix D. This distills and amplifies the electron contribution. Fig. 5.2 (b) shows a much higher contrast of the lock-in signal with more easily resolvable features within the EIT linewidth. Fig. 5.2 (c) shows a heat map of such signals as a function of the e-beam current (y-axis) and the blue laser detuning (x-axis). There is a clear growth of maximum lock-in signal with the e-beam current. We can see the location of the lock-in signal maximum shifts to the negative blue detuning as the electron current, and correspondingly its electric field, increases, in good agreement with the theoretical expectation of the negative Stark shift for $m_J = 5/2$ level. We plot the maximum value of the lock-in signal as a function of the e-beam current in Fig. 5.2 (d). This dependence is monotonic, even if not strictly linear, and it can be used as a calibration curve for the value of the current. Thus, our scheme provides a non invasive way to measure the e-beam current.

To gain spatial information about e-beam profile, we raster the relative position of the e-beam and the sensing region in $x - y$ plane perpendicular to the e-beam propagation direction (z). To change vertical (along y) relative position, we deflect the e-beam relative to the lasers with the pulser e-beam steering controls, see Fig. 5.3 (a). This is not ideal,

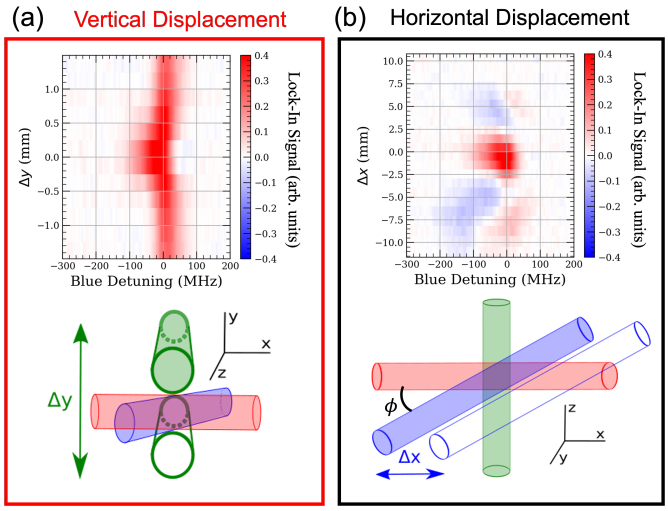

Figure 5.3: Results (top row) and geometrical arrangements (bottom row) of the electric field measurements in the horizontal and vertical directions. In both plots the red/blue cylinders represent corresponding laser beams, and the green cylinder is the e-beam. (a) The measured Stark shifts of the EIT resonances as the electron beam is moved vertically through the crossed laser beam region. (b) The lock-in signal modifications as the the blue laser beam is moved horizontally with a thick plastic plate. The central strong red spot corresponds to the location of the electron beam. The e-beam current was set to 108 μA.

since motion of the e-beam could change the electric field environment in the chamber due to stray charge deposition. But this is easier, since we do not have to translate two laser beams with respect to each other in sync. The heat map of lock-in signals in Fig. 5.3 (a) shows the presence of the feature at ± 0.5 mm range around 0 displacement. Since the spatial resolution is defined by the convolution of the laser beams and the e-beam diameters, in the y-direction it is limited by the e-beam diameter of 1 mm which matches the size of the spectral feature. For large y-displacements, we would expect the lock-in signal to be zero, but the largest displacements of ± 1.5 mm are not large enough to move the e-beam outside of the EIT sensing region. Nevertheless the lock-in signal drops with the increase of displacement.

Since the sensing region size along x is about 5 mm and we need to raster at least factor of two larger range, we cannot use the e-beam steering controls in this direction. Otherwise the e-beam would be clipped by its entrance aperture of about 8 mm diameter. Thus we change the x (horizontal) relative position Δx by translation of the blue beam

with a tilt of a thick acrylic plastic plate (see Fig. 5.1d). The tilt angle θ is geometrically connected to the beam translation d and Δx by the following equations

$$d = t[\tan\theta - \tan(\arcsin[\frac{\sin\theta}{n_p}])]\cos\theta \tag{5.1a}$$

$$\Delta x = d/\sin\phi. \tag{5.1b}$$

Where $t = 1.2$ cm is the thickness of the plastic plate, $n_p = 1.5$ is the index of refraction of the plate, and $\phi \approx 7^\circ$ is the angle of intersection between the red and blue lasers. Fig. 5.3 (b) shows the resulting lock-in signal heat map vs the horizontal motion. From its asymmetric shape with respect to zero displacement location and non vanishing signal at large displacements, it is apparent that there is an electric field gradient generated by the pulsing e-beam within the Rb chamber. This can be attributed to the modulation of charges on the glass optical window ports via Rb ionization or any number of charging effects that we do not have the infrastructure to mitigate in our Rb chamber. However, there is a strong feature near zero displacement that is due to the e-beam itself.

5.3 Electric field measurements

To confirm that we are sensitive to the x direction motion of the e-beam, we displace the e-beam horizontally with the pulser deflection controls and observed that the lock-in spectra maximum also moves in sync with the horizontal position sweep (see Fig. 5.4). Fig. 5.4 (a) is the lock-in spectra heat map vs the blue laser horizontal (x-direction) position scan and it shows that the maximum of the signal is moving proportionally to the e-beam displacement. We show the spectra center position vs the e-beam displacement in Fig. 5.4 (c), there is a clear linear relationship but we see that the measured beam center position does not follow one to one relationship. We attribute it to the charging effects in the chamber which skew the relationship. However, in a real setup it can be calibrated in advance and still provides a useful e-beam position monitor.

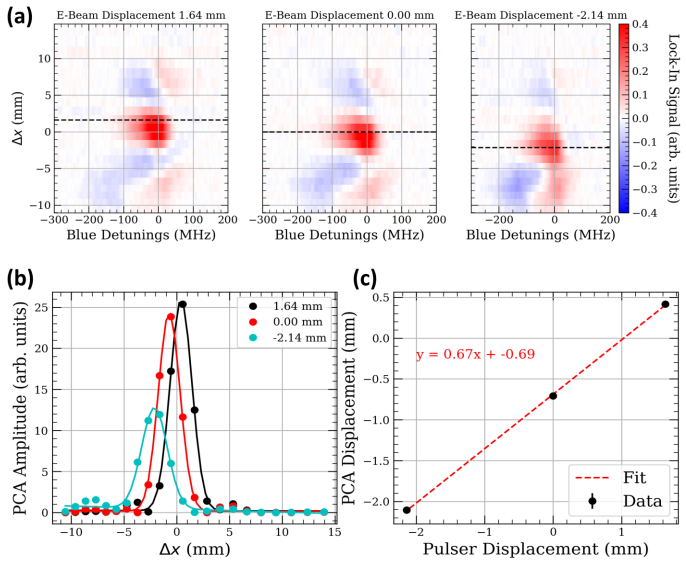

Figure 5.4: Measurements of the e-beam motion along x direction. (a) Heat maps of lock-in signal spectra vs the horizontal blue laser raster displacement Δx for different horizontal positions of the e-beam. The black dashed lines show the expected centers of the electron beam provided by the pulser deflection. (b) Calculated PCA amplitudes of the heat maps in (a) vs the horizontal laser beam displacement and their fits with a Gaussian shape. (c) The Gaussian center location of fits in (b) vs the pulser dialed displacement. The red dashed line is a linear fit line showing relationship between measured and dialed e-beam positions. For this dataset the e-beam current was set to 108 μA.

5.3.1 Principal Component Analysis (PCA)

Since every raster point in $x-y$-plane acquires the lock-in signal spectrum, we need to perform data reduction to generate a metric related to the e-beam strength at this position. We chose to use principle component analysis (PCA) to extract a physically relevant parameter. The PCA extracts characteristic patterns (principal components) which describe the experimental data [116] (i.e. the lock-in signal spectra vs the blue laser detuning). Theoretically the number of needed patterns is equal to number of collected spectra, but PCA sorts the patterns in the order of their contribution. Typically only a couple of first patterns are required to provide a good description for the data (see Fig. 5.5 where only two patterns were used). The contribution of the other patterns monotonically drops and they could be thought as describing the noise in the data or its outliers. Consequently, every lock-in spectrum $S_i \approx w_{1_i} \times \mathrm{PC}_1 + w_{2_i} \times \mathrm{PC}_2$, where i is

index of the measured spectrum, PC_i is the shape of the principal component, and $w_{1,2_i}$ is the weight (contribution) of corresponding component. We chose to use the amplitude $A_i = \sqrt{w_{1_i}^2 + w_{2_i}^2}$ as a metric describing the e-beam strength at the given raster point (we refer to it as the PCA amplitude).

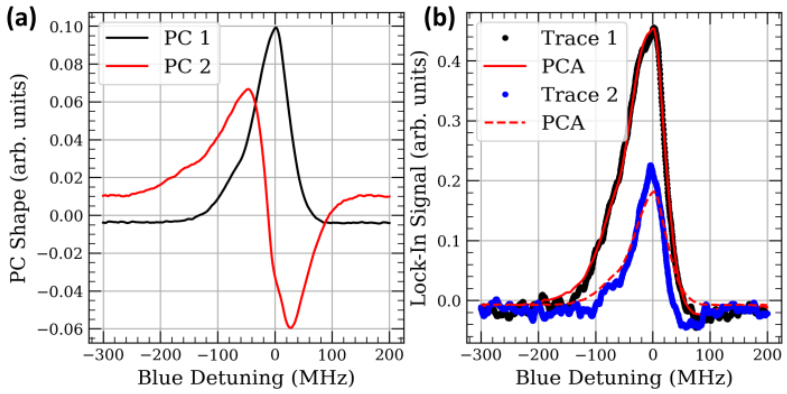

Figure 5.5: PCA analysis of the experimental data. (a) First two principle components (PC) or shapes that describe the data. (b) Example of two lock-in spectrum traces and their approximation with the weighted sum of these two principal components.

5.4 Extraction of the e-beam parameters

We measured the e-beam $x - y$ raster (profile) and show resulting heat map of the PCA amplitude as a function of displacement relative to the e-beam in Fig. 5.6 and Fig. 5.7 (a). The e-beam appears stretched along x-direction but this is to be expected since the spatial response is determined by the largest size from the actual e-beam cross sections and the laser beam overlapping region. For the x-direction we estimated the laser beam overlap size as 5 mm. The FWHM size in this direction is about 2.3 mm which is smaller than the overlap size, but a more precise estimate would require calculation of the beams shapes and the EIT power response convolution, which is smaller than our simple estimate. The vertical (y-direction) FWHM of 0.9 mm is limited by the e-beam size, size since it is limited by the width of the lasers.

We found that the maximum PCA amplitude in rastered 2D profiles has linear depen-

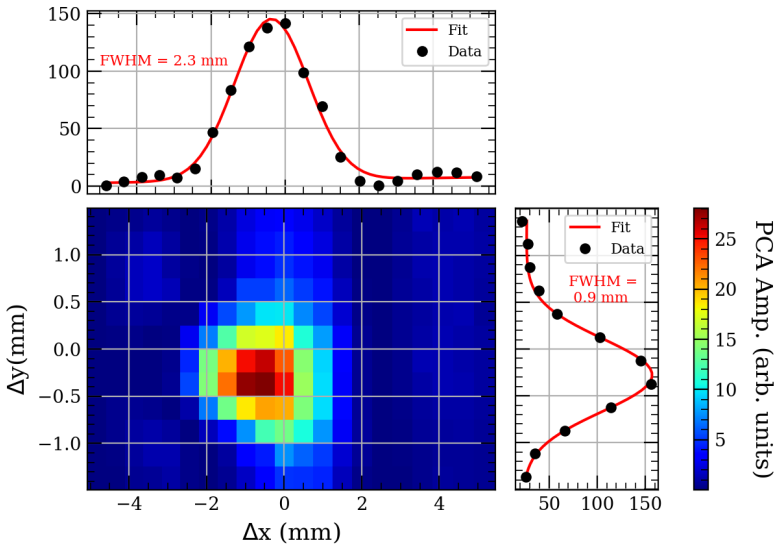

Figure 5.6: The PCA amplitude raster map of the e-beam raster. The e-beam current was set to 108 μA.

dence on the e-beam current as shown Fig. 5.7 (b). This dependence can be used as a calibration curve in a non-invasive e-beam current monitors.

5.5 Summary

This Chapter shows how one can use Rydberg atoms as non-invasive sensors to generate a 2D profile of an e-beam to deduce its size, position, and current using only optical transmission measurements. This technique can easily be extended for a 3D profiling. The resolution of the profile is limited by the largest limiting dimension of the overlap between the laser beams and the e-beam. In contrast to the Rydberg fluorescence profiling [103, 104], the presented laser beam crossing techniques can be used where an extra optical port is unavailable or in environments which are too harsh to collect images on a camera due to presence of, e.g., X-rays or ionizing radiation. The presented method is not limited to only e-beam detection but can be used for characterization any spatial distribution of the electric fields, for example generated near plasma boundaries.

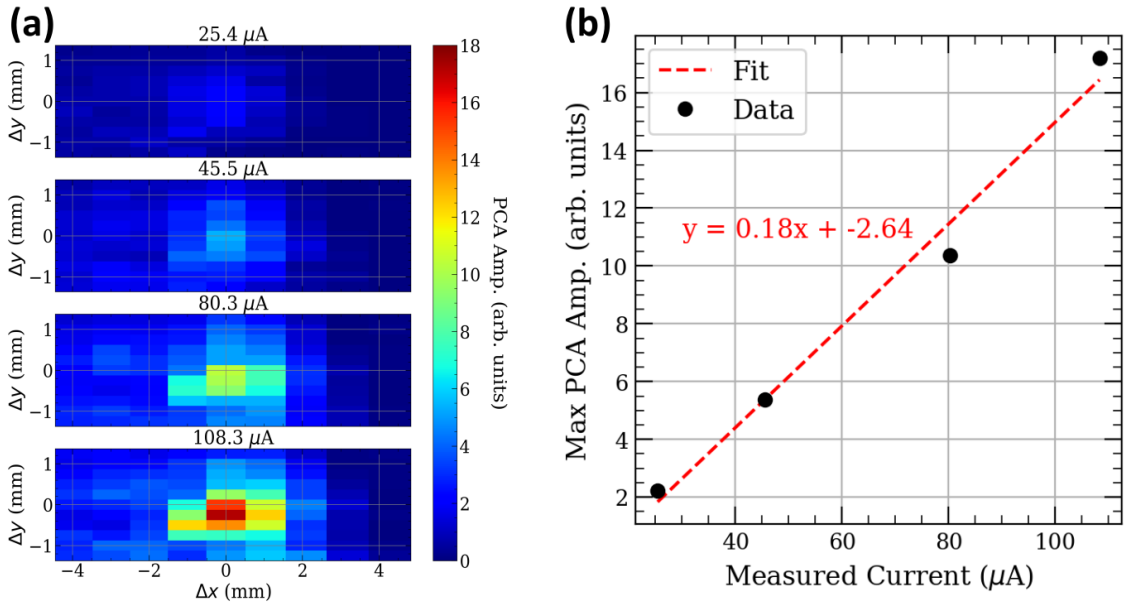

Figure 5.7: (a) The PCA amplitude raster maps for different e-beam currents. The displacement steps are not as fine as those in Fig. 5.6. (b) Dependence of the PCA amplitude maximum in the raster map vs the e-beam current for rasters in (a). The dashed red line is a linear fit.

Chapter 6

Polarization-based electric field direction measurements

6.1 Introduction

As discussed in Chapter 2, the quadratic nature of the Stark shift makes Rydberg electric field measurements sensitive to the magnitude of external dc-electric fields, but direction is more difficult. In this Chapter, we discuss efforts to reconstruct a dc electric field vector by recording both the frequencies and relative strengths of EIT two-photon resonances for different sub-levels of a Rydberg state. This approach relies on the polarization dependence of the transition probabilities between various Zeeman sub-levels, and has been explored previously to determine the direction of magnetic fields [69, 117, 118] and rf fields [57, 119]. In our experiments we demonstrate that we can determine the orientation of the electric field inside a vacuum chamber filled with Rb atoms by rotating the laser polarization and tracking changes in amplitudes and areas of Stark-split EIT peaks. Detection of EIT-induced fluorescence dips allows us to obtain spatial information about the inhomogeneous electric field, and reconstruct changes in its magnitude and orientation. We also present a semi-analytical atomic model that qualitatively agrees with our experimental data. This work was adapted from previously published work [120].

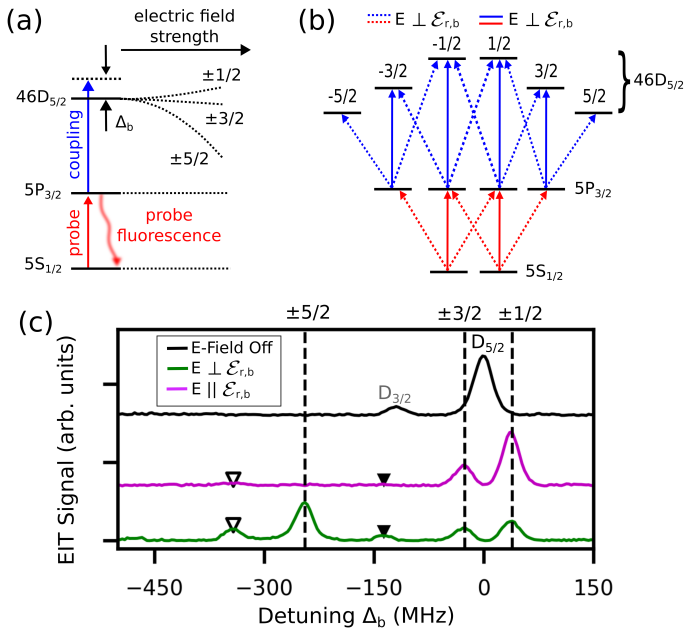

Figure 6.1: (a) Simplified energy level configuration of ^{85}Rb used to observe two-photon EIT resonances. The 780 nm probe laser is on resonance with the $5S_{1/2} \rightarrow 5P_{3/2}$ transition. The 480 nm coupling laser is scanned across the $5P_{3/2} \rightarrow nD_{5/2}$ transition with frequency detuning Δ_b. Dashed lines depict Stark splitting of the Rydberg $46D_{5/2}$ level into $|m_J| = 1/2, 3/2, 5/2$ sublevels as the static electric field strength increases. (b) Allowed transitions for optical field polarized parallel (solid) or perpendicular (dashed) to the dc electric field for a simplified fine structure of involved atomic levels. (c) Examples of EIT spectra in the absence of electric field (black), with electric field **E** applied perpendicular (magenta) and parallel (green) to both laser polarizations ($\mathcal{E}$). Dashed lines indicate the Stark shifts for $m_{J=5/2} = \pm 1/2, \pm 3/2, \pm 5/2$ sublevels of the $D_{5/2}$ level. Solid and hollow triangles show the locations of the EIT resonances associated with transitions to Stark-shifted sublevels of the $D_{3/2}$ level $|m_J| = 1/2$ and $|m_J| = 3/2$, respectively (since these peaks are much weaker, we do not use them in the analysis).

6.2 Basic sensing scheme

In this Chapter, we employ the same ladder-type EIT scheme to excite Rb atoms to the 46D Rydberg levels using two counter-propagating lasers at 780 nm and 480 nm, as all other previous experimental Chapters, shown in Fig. 6.1(a). As discussed in Chapter 2, the Stark effect lifts the degeneracy of the fine structure Rydberg states splitting the $(J = 5/2)$ into three and $(J = 3/2)$ into two. We use this splitting to determine the strength of the applied electric field.

The relative orientation of the electric field with respect to the light field propagation

direction and polarization does not affect the frequency positions of the EIT resonances, thanks to the quadratic nature of the Stark shift (at least for relatively low electric field amplitudes that do not produce Rydberg state mixing). However, the coupling strength to individual Zeeman sublevels of either fine (m_J) or hyperfine (m_F) component of the Rydberg state is polarization sensitive. Selection rules dictate that the laser polarization ($\mathcal{E}$) component parallel to the electric field (π-polarization) can only excite transitions with $\Delta m = 0$, while the circularly polarized components ($\sigma_\pm$) are responsible correspondingly for $\Delta m = \pm 1$ transitions. As a result, the populations of the various Rydberg sublevels, and thus the amplitudes of the associated EIT resonances for a given electric field orientation are determined by the choice of both polarizations for the red ($\mathcal{E}_r$) and blue ($\mathcal{E}_b$) lasers.

A simplified interaction scheme ignoring the hyperfine structure [shown in Fig. 6.1(b)] provides a simple intuitive understanding of this polarization dependence. While this over-simplified approach is too crude to accurately describe the experimental results, it helps to qualitatively understand the experimental EIT spectra shown in Fig. 6.1(c). For these measurements, both laser fields have identical linear polarizations, directed either perpendicular or parallel to the constant electric field. When the laser polarizations are perpendicular to the electric field, we observe all three Stark-shifted EIT peaks within the ($J = 5/2$) Rydberg transition. Indeed, in this case only optical transitions with $\Delta m_J = \pm 1$ are active, as shown by the dashed lines in Fig. 6.1(b). In this situation, the $m_J = \pm 5/2$ EIT peak has the highest amplitude due to the largest transition matrix elements involved, as previously reported [109]. At the same time the amplitude of $m_J = \pm 1/2$ EIT peak is relatively low. However, when the lasers are polarized along the electric field, the $m_J = \pm 5/2$ EIT peak completely disappears, since only $\Delta m_J = 0$ transitions are allowed, and there is no excitation path to reach states with $m_J = \pm 5/2$. Thus, we expect that by rotating the polarization and tracking the amplitudes of Rydberg EIT resonances, we should be able to determine the relative contributions of different transitions and thus extract the information about the electric field orientation.

6.3 Transverse uniform electric field measurements

Our experimental setup, Fig. 6.2(a), consists of a vacuum chamber filled with Rb vapor at room temperature that also contains built-in capacitor plates (24 mm separation) to produce a nearly homogeneous electric field in the x-direction. To test the effect of polarization on a constant field, the bottom plate is grounded and the top plate is held at a constant $V_0 = 5$ V. A 780 nm probe (500 μW power and $\approx$ 0.3 mm wide) laser drives the $5S_{1/2}, F = 3$ ground state of ^{85}Rb to an intermediate $5P_{3/2}, F = 4$ excited state, while a 480 nm coupling (50 mW power and $\approx$ 0.3 mm wide) laser drives the transition from the intermediate state to a Rydberg state. To calibrate the frequency axis we use the known splitting between the $46D_{5/2}$ and $46D_{3/2}$ Rydberg states as calculated using the Alkali Rydberg calculator (ARC) [4] and match it with the spectra measured within a reference Rb cell. The probe and coupling laser fields counter-propagate through the vacuum chamber and the reference cell, partially canceling the Doppler shift of each atom [26, 87]. We employ two complementary measurement approaches to detect EIT resonances (and corresponding Stark shifts of the $D_{5/2}$ Rydberg energy levels) as we scan the frequency of the coupling laser. First, we measure the 780 nm probe laser transmission and identify the centroid frequencies and areas under the EIT peaks. This method provides total contribution of all Rb atoms along the laser beam and is better suited for measuring the uniform electric field produced by the capacitor plates. Second, we record the changes in the 780 nm fluorescence along the probe laser beam, as discussed in Chapter 4, to obtain the local electric field information.

Fig. 6.2(b) experimentally demonstrates the dependence of the three $J = 5/2$ EIT peaks' strengths on the polarization orientations of both red (ϕ_r) and blue (ϕ_b) lasers. These measurements report EIT peak areas rather than peak amplitudes. For simplicity, we use the product of the amplitude and the full-width at half maximum proportional to the peak area, using the values obtained from a Gaussian fit. This helps mitigate broadening due to local electric field gradients. The general peak behavior is consistent with

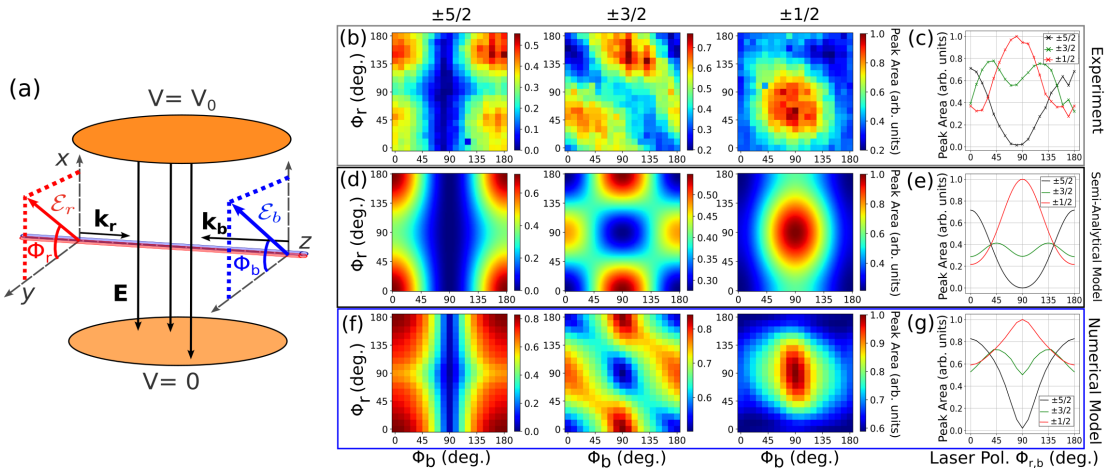

Figure 6.2: (a) Experimental arrangement for uniform electric field measurements. The electric field **E** points along the x-axis when a voltage V_0 is applied to the top capacitor plate. The laser beams counter-propagate along the z-axis, and their polarization orientations are defined by angles ϕ_r and ϕ_b, formed between the laser polarization vectors $\mathcal{E}_r$ and $\mathcal{E}_b$ with the $\hat{y}$ axis. (b) Experimentally measured peak areas of $|m_J|$ EIT peaks as functions of independently varying laser polarizations. (c) Experimentally measured dependence of all three peak areas on the angle between the electric field and the laser polarization when $\mathcal{E}_r$ and $\mathcal{E}_b$ are matched, i.e. $\phi_r = \phi_b$ ($\phi_{r,b}$). (d-g) Corresponding theoretical EIT area values calculated using the semi-analytical atomic model (d,e) or by numerically the solving the exact interaction Hamiltonian (f,g).

the expectations for the semi-analytic interaction model [Fig.6.1(b)]: the $m_{\pm 5/2}$ resonance is highest for ϕ_b and ϕ_r equal to either 0° or 180° (aligned with $\hat{y}$-axis) when the laser polarizations are perpendicular to the electric field in the $\hat{x}$-direction, and they disappear for $\phi_b \approx \phi_r \approx 90°$ when the laser polarizations and electric field vectors are aligned. The $m_{\pm 1/2}$ resonance displays the opposite behavior, increasing when the two laser polarizations are parallel to the electric field, and reducing (but not disappearing) when they are orthogonal.

6.4 Models of polarization dependence of Zeeman structure

To accurately calculate the amplitudes of Stark-shifted EIT peaks we need to take into account the hyperfine structure. The exact solution, however, is computationally expensive, due to the large number of states involved. While for the ground and intermediate states we may choose particular hyperfine levels F_1 and F_2 with the laser frequency, the hyper-

fine structure of the Rydberg state is unresolvable, and interactions with all the states $F_3 = 1 \ldots 4$ have to be considered. Also, since the Stark shift depends only on the electron total angular momentum, we must track which of the two-photon resonances contribute to which EIT peak based on the electron total angular momentum quantum numbers J_3, m_{J_3} of each Rydberg state hyperfine Zeeman sublevel.

We developed a simplified semi-analytical model, inspired by previous studies of Zeeman-resolved Autler-Townes measurements of Rydberg states [55]. In this model we consider all allowed two-photon transitions contributing independently into the final EIT transmission spectrum with the weight proportional to its interaction strength. For the probe laser $\vec{\mathcal{E}}_r$ we directly calculate the interaction dipole moments $d_{m_{F_1} \to m_{F_2}}$ between the hyperfine m_F states of the ground $5S_{1/2}$, $F_1 = 3$ and intermediate excited $5P_{3/2}$, $F_2 = 4$ states. The Stark shifts for these states are negligible. We then further simplify the description of the control laser $\vec{\mathcal{E}}_b$ interactions by calculating effective dipole moments between the intermediate state Zeeman manifold and the fine-structure m_{J_3} states – $d_{m_{F_2} \to m_{J_3}}$ – by summing the transition strengths of all m_{F_3} hyperfine sublevels, contributing to each m_{J_3} state. This approach accurately accounts for the strength of various atomic transitions for any directions of polarization and electric field vectors, but treats any possible ladder scheme independently and does not account for their interactions. In this case the total EIT transmission spectra $S(\Delta_b)$ is a sum of individual contributions:

$$S(\Delta_b) = \sum_{m_{J_3}} S_{m_{J_3}} \exp\left(-\frac{[\Delta_b - \Delta f_{|m_J|}(E)]^2}{2\gamma_{EIT}^2}\right), \tag{6.1}$$

where Δ_b is the frequency detuning of the blue laser, $\Delta f_{|m_J|}(E)$ is the Stark shifted frequency of each $|m_J|$ peak interpolated from a Stark map numerically solved using ARC [4], γ_{EIT} is the width of the EIT resonance, and $S_{m_{J_3}}$ is the total probability of all allowed

two-photon transitions contributing to each $|m_J|$ peak:

$$S_{m_{J_3}} = \sum_{m_{F_1}} \sum_{m_{F_2}} d^2_{m_{F_1} \to m_{F_2}} d^2_{m_{F_2} \to m_{J_3}}. \tag{6.2}$$

The dipole moment of a transition between any two hyperfine Zeeman sublevels depend on both the initial and final state quantum numbers and on the relative orientation of the laser polarization $\vec{\mathcal{E}}$ and applied electric field $\vec{E}$. For example, to calculate the transition strength induced by the probe laser field $\vec{\mathcal{E}_r}$ between the ground and intermediate state Zeeman manifolds, we need to consider both the selection rules and the relative strength of the laser polarization components:

$$\begin{aligned} & d_{m_{F_1} \to m_{F_2}} = \\ & \langle n_1, L_1, J_1, F_1, m_{F_1}| - e\vec{r} \cdot \frac{\vec{\mathcal{E}_r}}{|\mathcal{E}_r|} |n_2, L_2, J_2, F_2, m_{F_2}\rangle = \\ & \sum_{q=0,\pm 1} A^q_r \langle n_1, L_1, J_1, F_1, m_{F_1}| - e r_q |n_2, L_2, J_2, F_2, m_{F_2}\rangle. \end{aligned} \tag{6.3}$$

Here we choose the quantization z axis along the electric field direction, and we use the standard spectroscopic notation for atomic states (n is the principal quantum number, L is the total orbital angular momentum, J is the total angular momentum, F is the total atomic angular momentum, m_F is the azimuthal component of the total angular momentum). A^q_r and r_q describe the components of the probe laser polarization $\vec{\mathcal{E}_r}$ and the radius vector in the spherical tensor basis of π and $\sigma_\pm$ polarizations ($q = 0, \pm 1$), correspondingly. The dipole matrix elements between different hyperfine m_F states of the intermediate and the Rydberg states $d_{m_{F_2} \to m_{F_3}}$ are calculated the same way, but for the control laser polarization vector $\vec{\mathcal{E}_b}$.

To find the effective dipole moments $d_{m_{F_2} \to m_{J_3}}$ for the transitions between the intermediate and Rydberg states, we sum the dipole matrix elements of the transitions between m_{F_2} and all Rydberg hyperfine sublevels with the same m_{J_3} value. the given use the same approach for calculating the weights. However there is an extra complication of connecting

the hyperfine structure m_{F_2} states to the fine structure m_{J_3} states [55]:

$$d_{m_{F_2}\to m_{J_3}} \equiv \sum_{F_3'=1}^{4} \sum_{m_{F_3'}=-F_3'}^{F_3'} \sum_{m_I=-I}^{I} C_{Im_I J_3 m_{J_3}}^{F_3' m_{F_3'}} d_{m_{F_2}\to m_{F_3'}} \tag{6.4}$$

where $C_{Im_{I'}J_3m_{J_3}}^{F_3'm_{F_3'}}$ are Clebsch-Gordan coefficients, and $I = 5/2$ and m_I being the total nuclear spin angular momentum and its azimuthal component, respectively.

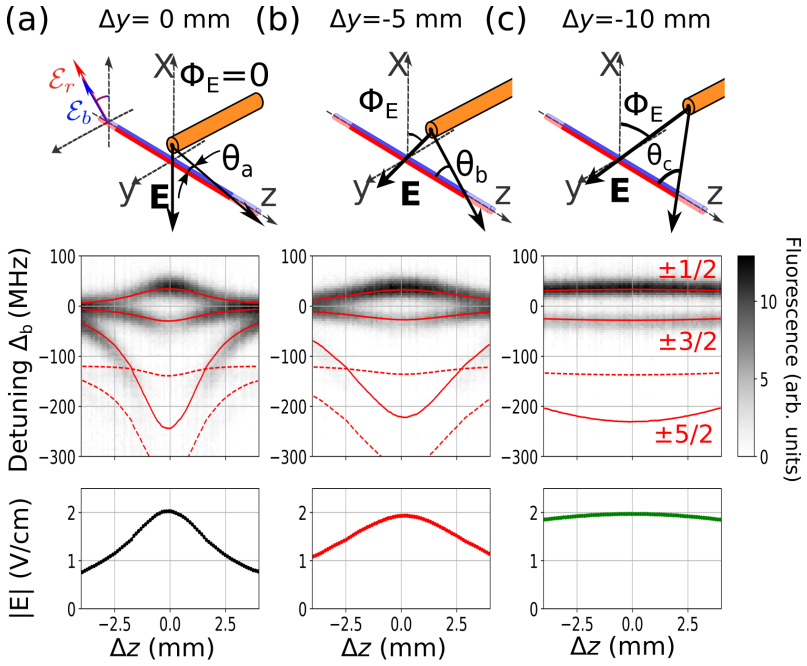

Figure 6.3: Fluorescence based electric field magnitude measurements. (a-c) Electric field magnitude reconstruction as the wire is displaced a distance Δy from the lasers. A retractable wire in our Rb vacuum chamber creates a spatially varying electric field when a voltage V_0 is applied. In the diagram of the wire with respect to the lasers, the darker red and blue lines indicate the laser fluorescence region monitored by the camera, $\theta_E = \theta_{a,b,c}$ denote the electric field variation with respect to the z-axis in each position of the probe and ϕ_E indicate angles with respect to the x-axis. Underneath these diagrams, the gray-scale maps are recorded fluorescence spectra for laser polarization orientation where the $m_J = \pm 5/2$ peak is minimized. Solid lines show reconstructed peak positions of the $46D_{5/2}$ $|m_J| = 5/2$, $3/2$ and $1/2$ and dashed red lines are the peak positions of the $46D_{3/2}$ levels. Finally, at the bottom we show the spatially reconstructed electric field magnitude for each position of the wire with respect to the lasers.

Fig. 6.2(d) shows the predictions of the semi-analytical atomic model for each EIT peak for the spectrum of probe and coupling laser polarization directions. We observe a clear similarity between these calculations and the experimental data. For the $m_J =$

$\pm 5/2$ resonance both the model and experiment show the highest peak amplitudes for nearly-parallel laser polarizations that are perpendicular to the electric field, while for the $m_J = \pm 1/2$ peak this arrangement minimizes the resonance amplitude. There is a small discrepancy between predicted and measured polarization configurations to maximize the $m_J = \pm 1/2$ peak amplitude. We speculate it is caused by some residual ellipticity of the laser fields and some spatial inhomogeneity of the electric field. The model is less successful in capturing the behavior of the $m_J = \pm 3/2$ peak. This peak has the most complicated composition of optical transitions, so it is not surprising that it is most strongly affected by the limitation of the model that neglects quantum interference between different excitation paths and population redistribution due to optical pumping. For that reason, in the later analysis we rely primarily on the $m_J = \pm 5/2$ and $m_J = \pm 1/2$ resonances when using the semi-analytical model.

We also carry out exact numerical calculations of the optical transmission using a density matrix approach with the full interaction Hamiltonian and the complete hyperfine structure of all three atomic levels (details in Chapter 2). The resulting heights of Stark-shifted EIT resonances, shown in Fig. 6.2(f), match well with the experimental results, and notably more accurately reproduce the angular dependence for the $m_J = \pm 3/2$ peak. For the other two resonances the predictions of the exact numerical calculations and semi-analytical theoretical models are in reasonable agreement. Because the exact numerical calculations are computationally expensive (owing to the large manifold of atomic states and Doppler broadening), this gives us additional confidence in using the semi-analytical model in further analysis.

The EIT "maps" in Fig. 6.2 suggest that to determine the direction of the electric field, it makes sense to align two laser polarizations and rotate them together. Figs. 6.2(c,e,g) show variations in EIT strengths for all three resonances for parallel polarizations: experimentally measured (c), calculated using our semi-analytical model (e) and exact numerical model (g). It is clear that such an arrangement provides maximal change in contrast in signals for the $m_J = \pm 1/2$ and $m_J = \pm 5/2$ EIT peaks as the laser polarizations are ro-

tated. It is also convenient that the polarization dependencies of the $m_J = \pm 5/2$ and $m_J = \pm 1/2$ peak areas are opposite to each other, e.g., the maximum of one corresponds to the minimum of the other and vice versa. This provides a robust tool to identify the direction of the azimuthal component of the electric field vector by finding the polarization orientation corresponding to the extrema in the EIT peak strengths. Importantly, since we observe very good agreement between results from experimental data and both the semi-analytical and full numerical models, we can, with a fair degree of confidence, use the semi-analytical EIT model for analysis of the $m_J = \pm 5/2$ and $m_J = \pm 1/2$ EIT peaks' polarization dependence.

6.5 Longitudinally varying electric field measurements

To test our method in a more realistic situation, we apply it to characterize a spatially inhomogeneous electric field generated by a piece of thin wire (1.4 cm length and 0.8 mm diameter) placed inside the Rb chamber (the plane electrodes are grounded for these measurements and have little effect). Applying a voltage V_0 to the wire induces electric charge accumulation at the rim of the wire cylinder tip, as confirmed by numerical solution of the Poisson equation for our experiment geometry. We also confirmed that we can neglect the wire thickness and approximate the charge distribution as a point charge q_0 at distances exceeding ≈ 1 mm from the wire. With this simplification, the electric field at any point is directed along the line connecting the tip of the wire and the observation point $\Delta\vec{r} = (d_x, \Delta y, \Delta z)$:

$$\vec{E} = -\frac{1}{4\pi\epsilon_0}\frac{q_0}{d_x^2 + \Delta y^2 + \Delta z^2}\Delta\hat{r}, \tag{6.5}$$

where ϵ_0 is the vacuum permittivity constant, and $d_x = 2$ mm is the vertical displacement of the laser beam from the wire.

Capturing spatial variations in the electric field vector requires fluorescence-based EIT detection [103, 104], where we image the fluorescence of the probe transition along a section of the laser beams near the wire and record EIT spectra for each camera pixel. We then fit

these fluorescence data using the Stark shift information from the ARC database [103, 104] for each z-position to get the magnitude of the spatially varying electric field. Fig. 6.3 shows an example of EIT fluorescence spectra and the reconstructed electric field strength at three positions of the wire: when the laser beams are directly below the wire tip $\Delta y = 0$ (a), when the wire is retracted by $\Delta y = 5$ mm (b) and $\Delta y = 10$ mm (c). To achieve roughly the same maximum electric field magnitude between the measurements, we adjust the applied voltage V_0 for each position. As expected we see the strongest electric field magnitude variation along the laser beams (z direction) near the wire tip, where it rapidly falls off with distance Δz. As the wire is pulled farther away we observe a smaller change in the electric field over the imaging region.

Since the laser beams have finite size, we integrate the the recorded signal across their transverse cross-section (along x and y dimensions of the interaction volume). If the gradient of the electric field across this region is sufficiently strong, it causes inhomogeneous broadening of EIT resonances. This broadening is particularly noticeable for the $m_J = \pm 5/2$ resonance that has the largest polarizability and, therefore, is the most affected by the field gradients. As a result, for some of the following analysis we mostly rely on the $m_J = \pm 1/2$ resonance measurements. We note, however, that the $m_J = \pm 5/2$ resonance becomes more attractive for Rydberg EIT measurements at lower n Rydberg states [121].

To characterize the electric field direction we use two angles: longitudinal θ_E (defined as an angle between the electric field and the laser propagation direction), and azimuthal ϕ_E (defined as an angle between the transverse $x - y$ component of the electric field and x-axis), as shown in the diagrams of the field generated by the wire in Fig.6.3. For example, in the earlier measurements the vertical electric field was perpendicular to the laser beam propagation: $\theta_E = 90°$ and $\phi_E = 0°$. Using Eq.(6.5), we can estimate values for both

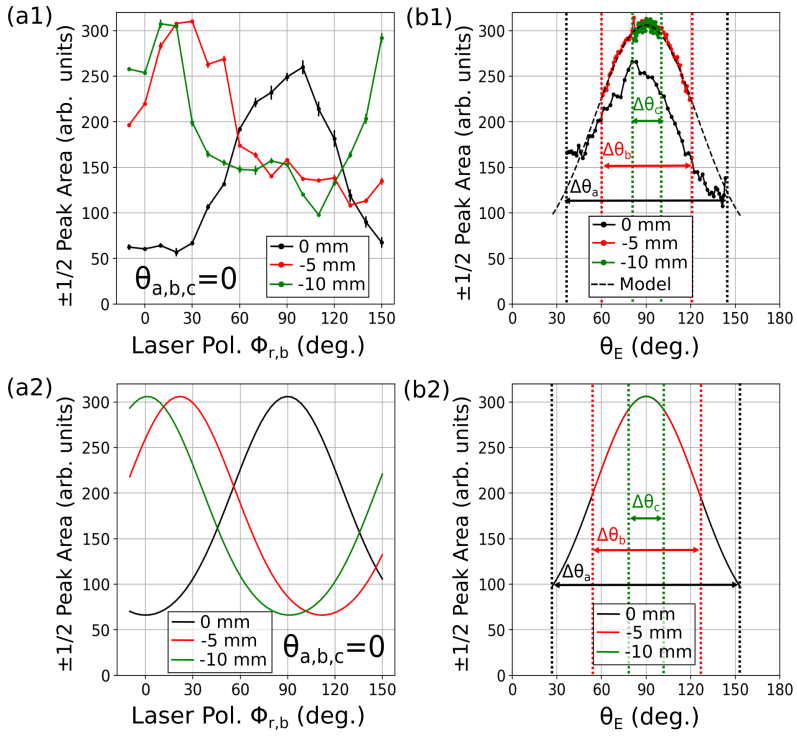

Figure 6.4: Variation of θ_E and ϕ_E for different Δy wire displacements. The different $\Delta\theta_{a,b,c}$ correspond to the different angular variations we show in Fig. 6.3. (a1) Experimental $m_{\pm 1/2}$ peak area for different wire Δy-positions, monitored with fluorescence at $\Delta z = 0$ mm. Error bars are an average of pixels from the center ±0.25 mm. (b1) Experimental $m_{\pm 1/2}$ peak area for different wire Δy-positions with a fixed polarization when $m_{\pm 5/2}$ peak is minimum. (a2) Modeled $m_{\pm 1/2}$ peak area for different wire Δy-positions. (b2) Modeled $m_{\pm 1/2}$ peak area for different wire Δy-positions with a fixed polarization when the $m_{\pm 5/2}$ peak is at a minimum.

angles:

$$\cos(\phi_E) = \frac{\Delta y}{\sqrt{d_x^2 + \Delta y^2}}, \tag{6.6}$$

$$\cos(\theta_E) = \frac{\Delta z}{\sqrt{d_x^2 + \Delta y^2 + \Delta z^2}}. \tag{6.7}$$

The value of the azimuthal angle ϕ_E depends primarily on the distance between the wire and the laser beam, and does not depend on the position along the laser beam. In the experiment we can find the azimuthal angle ϕ_E at each location by synchronously rotating the laser polarizations $\mathcal{E}_{r,b}$ and finding the angle at which the amplitude of the $m_J = \pm 1/2$ fluorescence peak is maximized. Fig. 6.4(a1) shows examples of such measured dependence

for three different distances Δy of the wire away from the laser beam, measured at the center $\Delta z = 0$ mm. We observe that when the wire is directly above the lasers ($\Delta y = 0$ mm), the area of the $m_J = \pm 1/2$ EIT peak is maximized when the laser polarizations are nearly vertical ($\phi_b = \phi_r = 90°$). As the wire is retracted, this maximum shifts toward horizontal polarizations ($\phi_b = \phi_r \to 0°$), indicating the expected change in ϕ_E. For comparison, in Fig. 6.4(a2) we plot the $m_J = \pm 1/2$ amplitudes calculated using our semi-analytic model and assuming an electric field distribution given by Eq.(6.5), which then agree well with experiment.

When we track the change in electric field direction along the laser beam, it primarily occurs in the longitudinal direction, as given by Eq.(6.7). Note that this variation depends on the horizontal distance Δy between the wire and the laser beam and we investigate three different wire positions in Fig.6.3. Since we monitor the same absolute z-range for each wire position, we expect to sample a smaller θ_E variation when the wire is farther away from the lasers. At the same time, measurement of θ_E is more challenging since the longitudinal component of the electric field does not fundamentally change the interaction symmetry and, consequently, the polarization dependence of the EIT peaks. Instead, reducing the angle between the electric field and the laser beams makes the polarization dependence less pronounced, reducing the span of azimuthal variations and eventually eliminating any polarization dependence as $\theta_E \to 0°$. For our experimental arrangement we thus expect to find the $m_J = \pm 1/2$ EIT peak to be the strongest for $\theta_E = 90°$ and then become smaller as θ_E decreases.

Fig.6.4(b1) shows the experimental dependence of the $m_J = \pm 1/2$ EIT peak area along the laser beam on the angle θ_E, calculated using Eq.(6.7). For each wire position, we adjust the laser polarizations to maximize the EIT contrast. The corresponding semi-analytic model calculations are shown in Fig.6.4(b2). As expected, we observe that the experimental EIT data generally follow the expected behavior: the measured resonance peak areas are largest at the position corresponding $\theta_E \approx 90°$, and they all have similar shapes but cover different range of angles. Specifically, the data for $\Delta y = -5$ mm and

$\Delta y = -10$ mm positions match the semi-analytic theory predictions extremely well. There is some deviation in overall resonance strength for $\Delta y = 0$ (most likely caused by some known imperfection in the wire and the effect of stronger field gradients, or our assumption that the wire acts as a point charge breaks down this close to the wire), but it still closely follows the expected dependence. This gives us some confidence that with better calibration it should be possible to use the EIT resonance analysis to reconstruct full vector information of inhomogeneous electric fields.

It is important to note that our method intrinsically does not allow us to distinguish between ϕ_E and $\phi_E + 180°$ as well as between θ_E and $180° - \theta_E$, as these angles result in identical interaction schemes. To uniquely identify the electric field direction we may need another degree of freedom. For example, introducing an additional magnetic field to set a clear quantization axis [55, 119]. However, this approach requires creating a more robust model to describe the interplay of Stark and Zeeman effects and will be a subject of future studies. Another challenge is that in our current experimental setup we cannot directly vary the orientation of the electric field, and thus it is impossible to experimentally verify the effect θ_E has on EIT resonances independently. Instead, we have to rely on the semi-analytical model for this information.

6.6 Summary

In this Chapter, we demonstrated that the strong dependence of various Stark-split m_J EIT resonances on the polarizations of optical fields can be useful for vector electric field measurements. Moreover, we showed that these changes are accurately described by a semi-analytic atomic model for the $m_J = \pm 5/2, \pm 1/2$ Rydberg states, but a more complete model and additional experimental verification are needed to describe the full EIT spectrum more accurately. Using the data available in this study, we estimate the uncertainty of electric field orientation to 0.5° for θ_E and ϕ_E. This is in the range of angles and polarization with maximum variation of amplitude response. In orientations of the

electric field and polarization where the $m_J = \pm 1/2$ peak does not vary in amplitude the sensitivity is worse, but laser polarization can be optimized to achieve sub-degree angular resolution. The reported results suggest a viable approach for vector electric field measurements that will enable accurate reconstruction of electric charge distributions for, e.g., electron beam characterization [104] and plasma diagnostics [121–123].

Chapter 7

Reducing EIT linewidth with optical Ramsey Interrogation

7.1 Introduction

This Chapter describes a novel detection scheme designed to further enhance the sensitivity of Rydberg atomic sensors. We extend the three-level interaction model discussed in Chapter 2 to describe Raman-Ramsey resonances in both temporally and spatially separated interaction schemes. Preliminary experimental efforts are also presented, together with an analysis of the practical challenges associated with realizing these resonances.

For practical applications, moderate power broadening of EIT resonances can be advantageous, as increased laser power improves coherence preparation and enhances EIT amplitude. Ultimately, the sensitivity of room-temperature Rydberg sensors is limited by power broadening and thermal atomic motion.

To mitigate these limitations, we propose a Raman-Ramsey interrogation scheme consisting of two laser interactions separated by a dark evolution time [124], as shown in Fig. 7.1. The main idea is that the atoms are initially prepared in a coherent superposition of the ground and Rydberg state with an optical pulse of two laser fields (EIT). The atomic coherence is then left to evolve in the dark in the absence of the light fields. During this

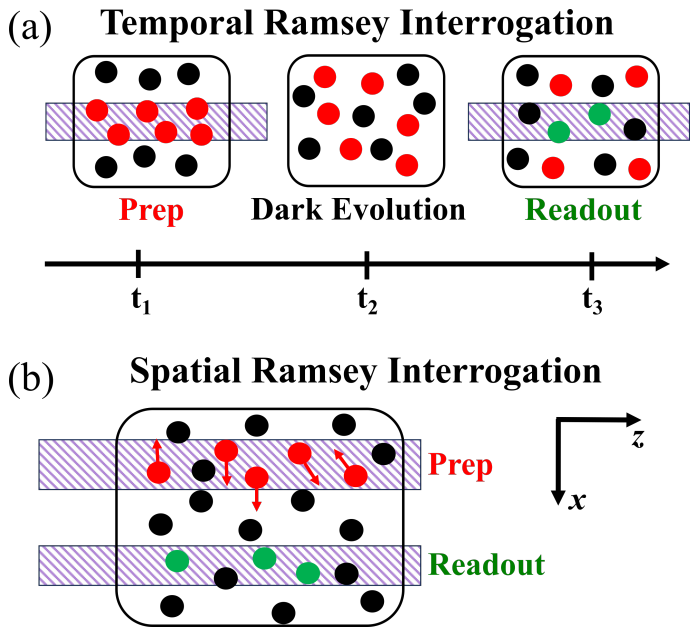

Figure 7.1: (a) *Temporal R^3 resonances:* Atoms are prepared in the coherent superposition with two EIT laser fields (red) during time t_1, and then allowed to evolve in the dark for time t_2, while laser fields are turned off. Any changes in the atomic coherence are read out with a second light pulse (containing both EIT laser fields) of duration t_3. Only the initially prepared atoms remaining in the interaction volume (green) contribute to the R^3 resonance. (b) *Spatial R^3 resonances:* Atoms are prepared in the coherent superposition with two EIT laser fields (red) in a prep interaction region, and move ballistically toward the readout region (also containing two EIT laser fields), crossing the dark region in between. Only the atoms reaching the readout region (green) contribute to the R^3 resonance formation.

dark evolution time, the phase of the atomic coherences change. The accumulated phase difference can be read out using a second (detection) pulse, whose duration and intensity are optimized to maximize the signal-to-noise ratio. Because the majority of the phase evolution occurs in the dark, power broadening is significantly suppressed, even when strong fields are used during the preparation and detection stages.

We consider two possible scenarios: temporal separation, which uses two bi-chromatic optical pulses to first prepare and then read out atomic coherence between the ground and Rydberg states, as shown in Fig. 7.1(a); spatial separation, where moving atoms encounter two separate interaction regions of continuous optical fields, shown in Fig .7.1(b).

Numerical modeling shows that both approaches produce a narrow Rydberg Raman-Ramsey (R^3) spectral feature in addition to the conventional Doppler-broadened Rydberg

EIT resonance. Because only slow atoms contribute constructively to the R^3 signal, the effective Doppler broadening is substantially reduced. Temporal Raman-Ramsey interrogation schemes have been successfully implemented for improving the performance of the atomic clocks based on Λ-based EIT systems [125, 126], and a spatial Ramsey interrogation has been demonstrated [127]; however, neither approach has yet been implemented in Rydberg atom-based sensors. Text and figures from this Chapter are adapted from previously published work [128].

7.2 Time evolution of density matrix elements model

We now describe how to numerically model this optical Ramsey interrogation. Fig. 7.2(a) shows the temporal Ramsey interrogation sequence. Using the density matrix formalism introduced in Chapter 2, we solve the Lindblad master equation

$$\frac{\partial \rho(t)}{\partial t} = \frac{-i}{\hbar}[H, \rho(t)] + \sum_i \mathcal{L}, (\rho, \sigma_i), \tag{7.1}$$

to solve for the atomic coherences as they evolve in time.

For an initial state preparation time t_1, the lasers for EIT prepare the atoms in a coherent superposition of the ground and Rydberg state. The preparation time t_1 is assumed to be sufficiently long enough for the system to reach the steady state for the given laser parameters.

Following the preparation pulse, the laser fields are quickly turned off, and the long-lived coherence between the ground and Rydberg states ρ_{gr} is allowed to evolve in the dark for time $1/\Gamma_r \geq t_2 \geq 1/\Gamma_e$, where Γ_e and Γ_r are the state lifetimes of the excited and Rydberg states, respectively.

For the dark evolution time $t_2 \gg 1/\Gamma_e$, the population of the intermediate excited state and the coherence between the ground state and intermediate excited state quickly vanish. The population of the Rydberg state ρ_{rr} and the coherence between ground and

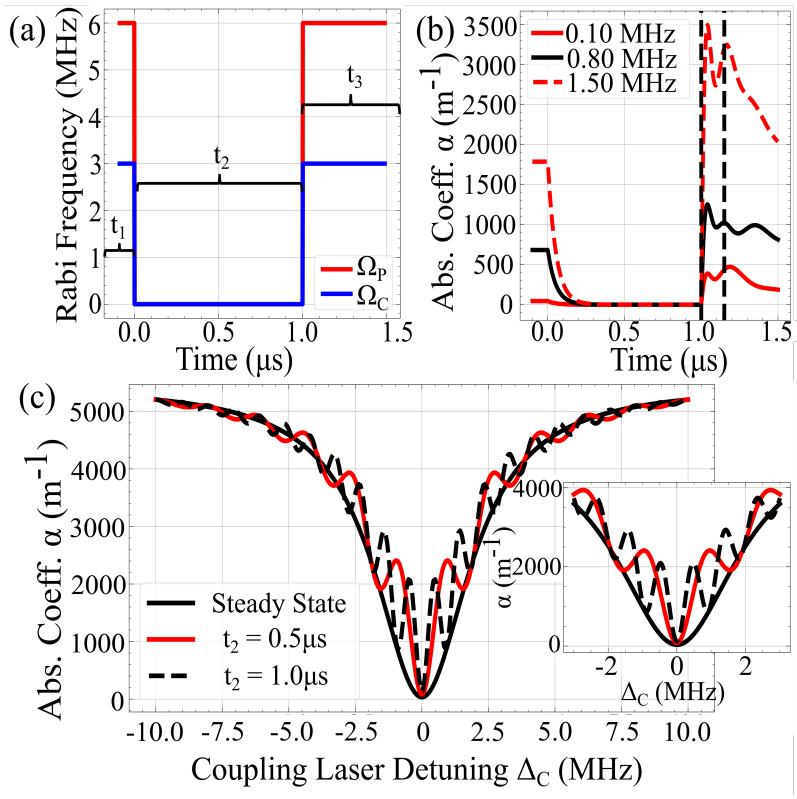

Figure 7.2: (a) Time sequence of temporal Ramsey interrogation for stationary atoms. (b) Theoretically predicted R^3 optical response for stationary atoms for different two-photon detunings δ_R. Black dashed lines indicate the 150 ns integration region used to reconstruct Ramsey fringes. (c) R^3 resonances as a function of the coupling laser detuning for different evolution in the dark time t_2. The model parameters are $\Delta_P = 0$, $\Gamma_e = 6$ MHz $\times\ 2\pi$, $\Gamma_r = 3$kHz $\times\ 2\pi$, $\Omega_C = 0.5\Gamma_e$, $\Omega_P = \Gamma_e$, $\mathcal{N} = 1.7 \times 10^{11}$ cm^{-3}, $\mathbf{d}_{ge} = 1.46\times 10^{-29}$ C·m.

Rydberg states ρ_{gr} survive, as they decay much slower, and we can take advantage of this consideration to simplify the model by replacing the exact numerical simulations for all atomic parameters at the end of the dark evolution with simple analytical solutions for non-vanishing coherences:

$$\rho_{rr} = \rho_{rr,ss} e^{-t_2\Gamma_r} \tag{7.2a}$$

$$\rho_{gg} = 1 - \rho_{rr} \tag{7.2b}$$

$$\rho_{gr} = \rho_{gr,ss} e^{-\frac{\Gamma_r}{2}t_2} e^{-i(\Delta_C+\Delta_P)t_2}. \tag{7.2c}$$

Here, $\rho_{rr,ss}$ and $\rho_{gr,ss}$ refer to the steady state solution of the density matrix elements before the dark time. In cases of non-zero two-photon detuning $\delta_R = \Delta_C + \Delta_P \neq 0$, ρ_{gr} acquires a phase $e^{i\delta_R t_2}$.

The density matrix, containing only ρ_{gg}, ρ_{rr}, and ρ_{gr}, is then used as the initial condition in the Lindblad master equation (Eq. 7.1) for numerical time evolution during the detection pulse of a fixed duration t_3. Fig. 7.2(b) shows simulated time responses of different coupling laser detunings. Dotted vertical black lines indicate the 150 ns integration window used to reconstruct the R^3 resonance.

If this time is shorter than the time required to re-establish the steady-state EIT, the probe laser transmission is largely determined by the accumulated phase of ρ_{gr}, and displays a clear interference-like fringe pattern, as shown in Fig. 7.2(c) with the frequency inversely proportional to the dark evolution time. Thus, in this case of stationary atoms that experience this interaction scheme, we can theoretically achieve the spectral resolution limited only by the Rydberg state decoherence time.

7.3 One-dimensional atomic motion in time evolution model

Atomic motion in thermal atomic vapor greatly affects the characteristics of two-photon optical resonances. For temporal Raman-Ramsey excitation, we only consider atomic motion in the laser propagation direction (z). This longitudinal motion of atoms produces two generally undesirable effects on the R^3 fringe formation, both related to the large frequency mismatch between the two optical fields. The first one is the spatial phase variation between the probe and coupling fields, and the other is the differential Doppler shift for atoms with different longitudinal velocities.

We first consider the contributions due to the Doppler effect, as it equally affects R^3 and steady-state EIT resonances, and has been identified as one of the main limiting factors for Rydberg EIT-based sensor sensitivity. An atom with longitudinal velocity v_z along the laser beam experiences a Doppler shift $\omega v_z/c$. Even for counter-propagating

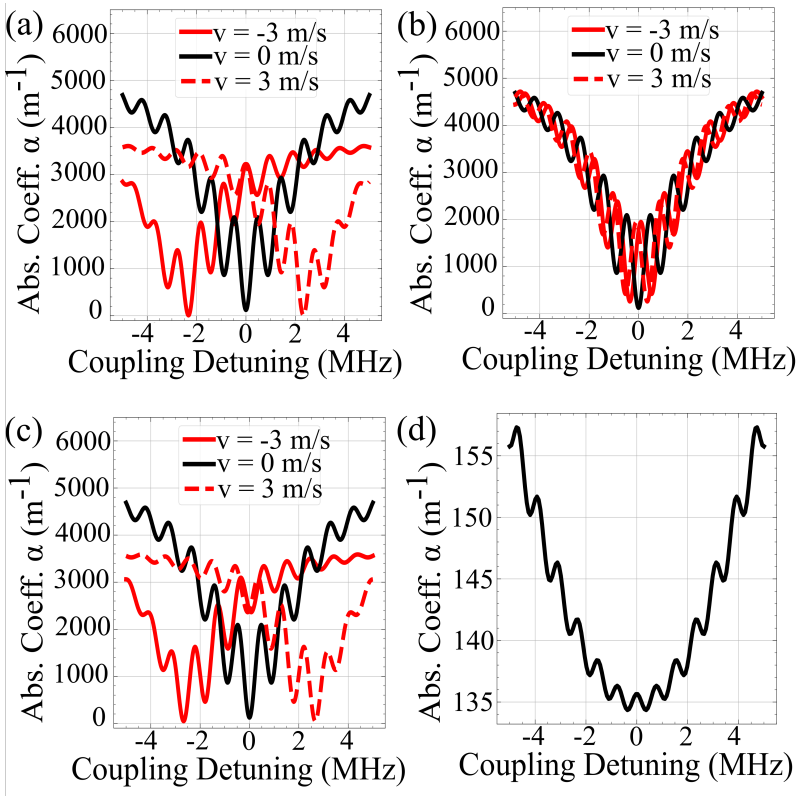

Figure 7.3: Examples of Ramsey fringe modifications for longitudinal motion of atoms ($\hat{z}$). For (a) - (c), it is assumed that all atoms move with the given velocities v_z to illustrate the effects of phase and Doppler mismatch. (a) Effect of Doppler mismatch of detunings. (b) Effect of spatial phase variations. (c) Effect of both Doppler and phase variations. (d) Fringes resulting from dark time $t_2 = 1$ μs and $t_3 = 150$ ns for a range of velocities integrated over a thermal 1D distribution corresponding to 300 K; note the different scale for α.

beams, residual wave-vector mismatch produces a velocity-dependent two-photon detuning $\delta_R(v_z) = (\Delta_C + \Delta_P - \omega_{rg}) + (k_P - k_C)v_z$. Even when the lasers are tuned precisely to the two-photon resonance, only atoms with small longitudinal velocities contribute significantly to EIT formation. The residual Doppler mismatch broadens the observable EIT linewidth to a few MHz.

In the case of Raman-Ramsey excitation, such a Doppler mismatch makes the phase acquired during the dark evolution dependent on atomic velocity. This results in a relative shift of the Ramsey fringes for each velocity group, as shown in Fig. 7.3(a). When integrated over all velocity classes, this effect alone can substantially suppress fringe contrast.

We also need to take into account the spatial variation of the relative phase of the two optical fields along the beam path. The initial phase of ρ_{gr} is set by the relative phase of Ω_C and Ω_P. Because the two fields possess different wave vectors, this phase depends on position along the beam path. When an atom moves between the preparation and detection steps, the accumulated coherence phase reflects the spatial phase difference between those two positions.

This effect almost exclusively affects R^3 fringe formation, rather than steady-state EIT, since in the latter case the coherence phase adiabatically adjusts as atoms move along the laser beams. However, in the Raman-Ramsey process, moving atoms, detected at $z = 0$, have been prepared at the location $-v_z t_2$, and thus their coherent state carries an additional phase $-(k_P - k_C)v_z t_2$ (for the counter-propagating optical fields). Again, the contributions of different velocity groups destructively interfere, in principle limiting the fraction of atoms that can contribute to the observation of R^3 resonance. Fig. 7.3(b) shows the fringe shifts due to the spatial phase mismatch for different v_z. However, when considered together, these two phase shifts partially compensate each other. Fig. 7.3(c) shows that the Doppler effect and relative displacement effects work together to bring the fringes back to constructive interference and preserve narrow fringes. Thus, R^3 fringes "survive" the integration of the 1D Maxwell-Boltzmann velocity distribution of atoms in the z-direction, as shown in Fig. 7.3(d) for a single t_2 dark time, albeit with reduced amplitude compared to the cold atom case due to fewer participating atoms.

This analysis gives a somewhat optimistic outlook on the possibility of observing narrower Rydberg EIT features using Raman-Ramsey excitation. However, from the practical point of view, such temporal interrogation may introduce some technical complications, such as the need for excellent pulse synchronization, fast pulse turn-on/turn-off, and a low detection duty cycle.

7.4 Two-dimensional atomic motion in time evolution model

An alternative approach to realizing Raman-Ramsey interrogation with continuous-wave lasers is to spatially separate the preparation and detection regions. In this configuration, the dark interval arises naturally as atoms propagate between the two interaction regions.

To model the spatial implementation of the R^3 resonance, we consider two parallel interaction regions separated by a distance d, as illustrated in Fig. 7.1 (b). Each region contains a counter-propagating probe and coupling beams. To increase the number of participating atoms, both regions are extended along the direction perpendicular to atomic motion. Under these assumptions, the relevant dynamics can be reduced to two-dimensional atomic motion between the regions, as shown in Fig. 7.4 (a).

Atoms are assumed to reach a steady state in the preparation region before exiting with transverse velocity v_x. Those with nonzero v_x traverse the separation distance d and subsequently enter the detection region, thereby recreating the temporal sequence analyzed in the previous section. For a given transverse velocity, the effective dark time is $t_2 = d/v_x$. Different transverse velocity classes correspond to different effective dark times and therefore produce Ramsey fringes with different periods, as shown in Fig. 7.4 (b).

To fully account for thermal motion, the resulting signal is integrated not only over the transverse velocity distribution but also over the longitudinal velocity distribution in the z-direction. The z-motion captures phase shifts associated with Doppler and spatial displacement effects discussed previously. After integration over both velocity components, a narrow central R^3 fringe remains.

Fig. 7.5(a) shows a theoretically predicted R^3 resonance, calculated using the same atomic parameters as Fig. 7.2 with a beam separation of $d = 1$ mm and a second interaction region of width $w = 50$ μm. Here we integrate the contributions to the optical susceptibility from each longitudinal velocity class for a given dark time t_2, and then integrate these results over all possible dark times $t_2 = d/v_x$.

Because of the mutually destructive contributions of atoms with different velocities,

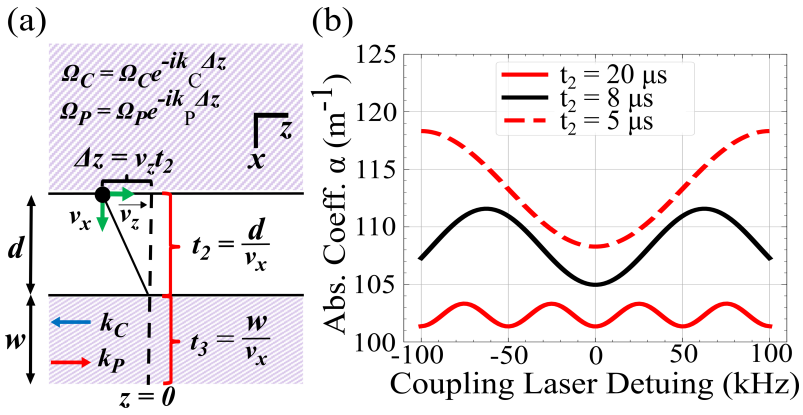

Figure 7.4: (a) Spatially separated geometry model. Each interaction region (purple) contains counter-propagating probe and coupling beams. The preparation region (top) is assumed sufficiently wide, and separated by a distance d from the detection region that has a finite width w. (b) Examples of Ramsey fringes for atoms with different transverse velocities v_x (resulting in different effective dark times t_2) integrated over the longitudinal velocities v_z.

we carefully optimized the number of velocity classes included in the simulations. For the longitudinal integration, the simulated density matrix element reaches a stable point at an integration range of -6μm $\leq \Delta z \leq$ 6μm with 75 included velocity classes. For the transverse integration range, we use $0 \leq v_x \leq 400$ m/s with 50 velocity classes. These limits not only help manage simulation run time but also show that the integrated signal is not a product of numerical instability.

The resulting optical absorption in Fig. 7.5(a) clearly shows two spectral features of different widths. The broader resonance is a "standard" Doppler-broadened EIT resonance due to atoms interacting with light only in the detection region. However, the second interaction for slower atoms produces an additional narrow feature on top of the broad EIT resonance - the R^3 resonance. The details of these narrow spectral features are best shown in Fig. 7.5(b). The full-width half maximum (FWHM) of the resulting resonance is quite narrow, near 120 kHz, which is almost two orders of magnitude narrower than the broad EIT feature, even though its amplitude is much smaller as well. What is remarkable is that this narrow linewidth is fairly immune to the finite laser linewidth. For example, if we calculate the width of the R^3 resonance assuming that the probe and coupling lasers have zero, 100 kHz, and 500 kHz linewidth, the FWHM of the narrow feature increases

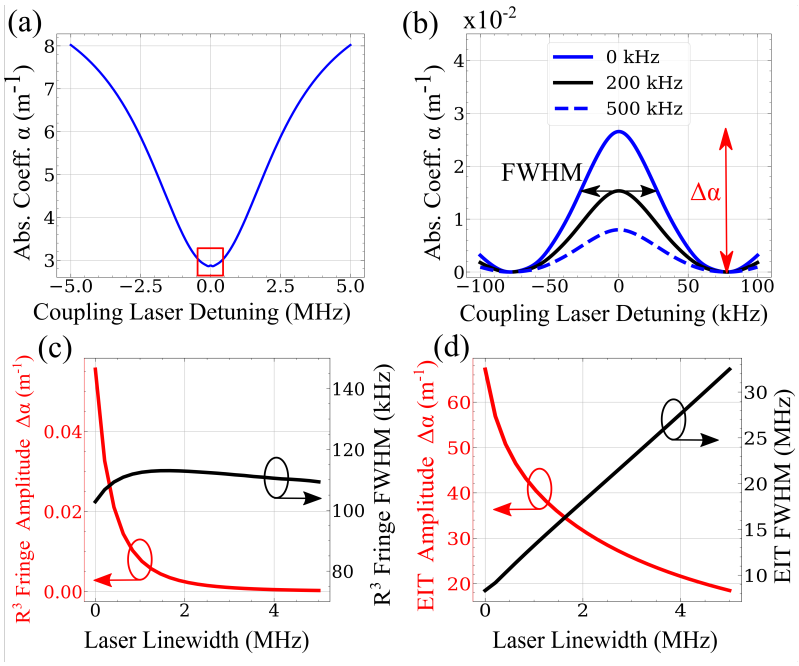

Figure 7.5: (a) Predicted R^3 absorption resonance as a function of coupling laser detuning for $d = 1$ mm and $w = 50$ μm. The red box is the zoomed scale for the traces in (b). (b) The narrow R^3 feature for laser linewidths of the probe and coupling lasers at 0 kHz, 200 kHz, and 500 kHz. (c) Amplitude and FWHM of the R^3 feature for increasing laser linewidths. (d) Amplitude and FWHM of standard Doppler-broadened EIT for increasing laser linewidths.

from 116 kHz to 121 kHz and 125 kHz, correspondingly. Fig. 7.5(c) gives a more complete picture of the effect of the laser linewidths on the R^3 resonance. For this simulation, the laser linewidths γ_C and γ_P are considered equal for simplicity. The FWHM of the fringe remains relatively constant, but its amplitude drops as the laser linewidth increases. This is not unexpected: only a fraction of atoms with intact coherence contribute to the detection of the Raman-Ramsey feature, while additional dephasing reduces the fraction of atoms participating in R^3 resonance formation. In contrast, the linewidth of the standard EIT resonance increases linearly with the laser detuning, as shown in Fig. 7.5(d).

Fig. 7.6 shows the impact of interaction channel separation distance d on the FWHM and amplitude of this central fringe. Fig. 7.6(a) demonstrates the evolution of the fringe as the separation distance d increases. Fig. 7.6(b) shows the same analysis of the amplitude and FWHM as done for Fig. 7.5 but now as a function of separation distance d. As

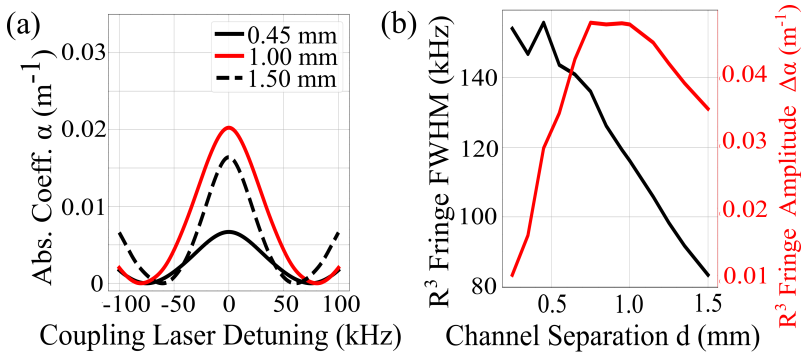

Figure 7.6: Simulated central R^3 spatial fringes for varying measurement parameters. (a) R^3 fringe for various channel separation distances d. (b) Values for FWHM and height of the R^3 fringe vs. d.

expected, we observe a reduction of resonance amplitude for larger channel separation; the height of the peak reaches its maximum value near $d = 1$ mm and then starts to decay, as fewer coherently prepared atoms survive the crossing between the two regions.

7.5 Theoretical comparison of different interrogation schemes

To compare the potential advantage of a narrow R^3 resonance over standard single-interaction steady-state EIT, we have to choose a figure of merit for spectral resolution (or sensitivity). A small frequency variation Δf from the EIT peak due to an incident electric field produces a change in the probe transmission proportional to the first derivative of the spectral response vs. coupling laser frequency. Assuming shot-noise limited measurements, we can then calculate the minimum detectable frequency change Δf_{min}:

$$\Delta f_{min} = \left[2L \frac{\partial \alpha}{\partial \Delta_C} \sqrt{\frac{P}{\hbar \omega}} \sqrt{\Delta t} \right]^{-1}, \tag{7.3}$$

were $L = 2.5$ cm is the interaction region length, P is the power of the probe laser for a given Ω_P, and Δt is the duration of the measurements. Fig. 7.7 shows the dependence of Δf_{min} for the different interrogation schemes for Δt =1 s. It is clear that the time-separated R^3 fringe should provide significantly higher sensitivity. However, such a straightforward comparison gives it an unfair advantage for the temporally separated Ramsey case, since

in reality only a small fraction (first 100 ns of the read-out pulse) of the time sequence is devoted to the data collection, since it takes $t_1 \approx 1$ μs to reach the steady-state EIT regime. Thus, assuming the dark time $t_2 = 1$ μs, the useful signal is collected only during 1/50 of the whole cycle. Thus, to properly compare the three different methods, we also include the sensitivity trace for the temporally separated Ramsey fringe case with Δt =0.02 s.

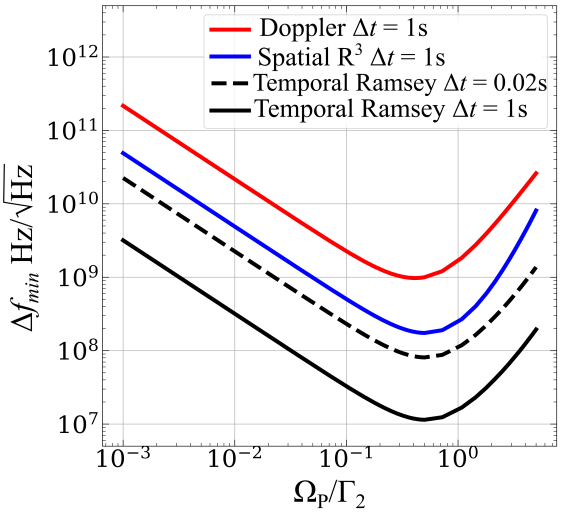

Figure 7.7: Comparison of the minimum detectable frequency shift between standard Doppler-broadened EIT, spatially separated R^3, and temporally separated Ramsey measurements. Δf_{min} is calculated as described in Eq (7.3). Here, the temporal Ramsey case is calculated with a different Δt detection time to account for the short integration time to produce the signal.

A comparison of the Δf_{min} as a function of the probe Rabi frequency is shown in Fig. 7.7. Both Ramsey-style measurements predict a smaller detectable frequency shift than the standard Doppler-broadened case. Thus, at least in the idealized case considered here, the method of spatially and temporally separated Ramsey fringes can lead to a more sensitive measurement.

7.6 Spatially separated measurements

Here we present some preliminary experimental investigations of the spatially separated beam geometry using a two-channel detection scheme as shown in Fig. 7.8 (a). In these measurements, the coupling laser is tuned to resonance with the $5P_{3/2} \rightarrow 56D_{5/2}$ transition.

Channels A and B refer to two spatially separated optical interrogation regions, each containing one or both of the 780 nm probe or 480 nm coupling light propagating along the z-direction. For these experiments, we did not have the ability to control the relative phases of the optical fields in the two channels. Therefore, the measurements focused on phase-independent Rydberg population transfer, monitored via changes in the probe absorption in each channel separately.

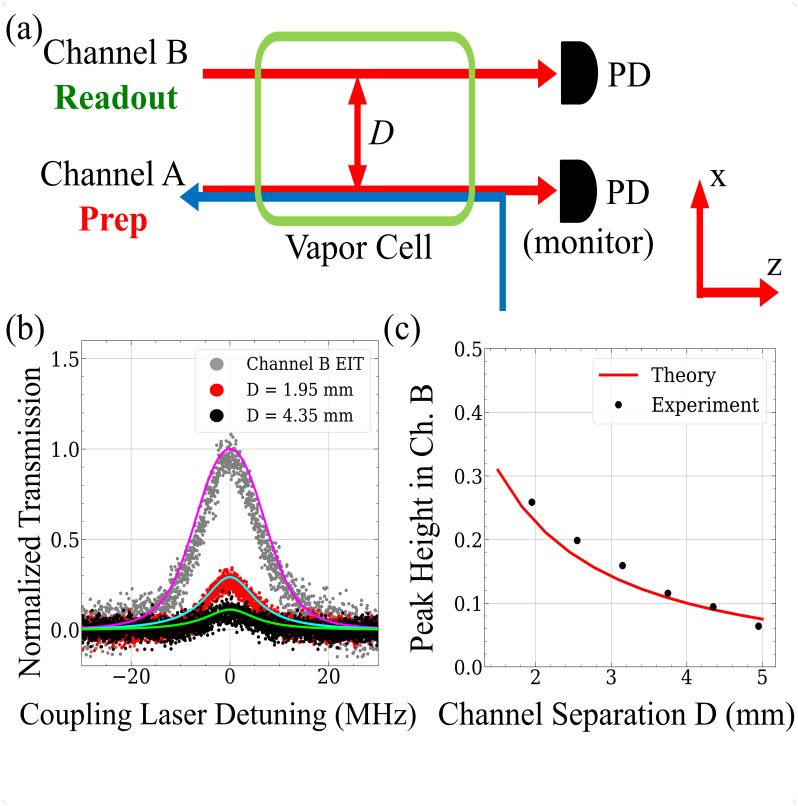

Figure 7.8: (a) Experimental setup for spatially separated beam geometry. (b) The transmission of infrared light in channel B for a given beam separation D. Reported transmission is normalized to the peak steady-state EIT transmission experimentally observed using only the infrared and blue beams of channel B (channel A blocked), shown on the grey curve. Channel A and Channel B EIT signals are similar when both red and blue lasers are present. Solid curves correspond to simulated spectra for the same parameters. (c) The experimentally measured EIT peak height as a function of beam separation, as compared with the results predicted by our theoretical model with no free parameters.

The laser beams in both channels were oval-shaped and identical in size. The probe beam diameters were 100 μm in the x-direction, and 8 mm in the y-direction, while the

coupling beam diameters were 100 μm in x, and 6 mm in y. The separation distance D between the two channels was adjusted to investigate its effect on probe transmission.

To eliminate optical crosstalk between channels, we maintained sufficient channel separation. Residual interference between beams of the same wavelength was observed for separations below $D \approx 0.5$ mm, as verified using a beam profiler placed at the location of the vapor cell. All measurements were therefore performed at separations exceeding this threshold. We confirmed negligible stray probe light from channel A reaching the channel B detector (and vice versa). The absence of an EIT signal arising from overlap between channel A coupling light and the channel B probe verified negligible cross-interaction between these fields.

Using this setup, we clearly observed the effects of the Rydberg atoms moving between the two interaction regions. For these measurements, only atoms in Channel A were excited to the steady-state Rydberg EIT state via the two-photon transition, while Channel B contained only the 780 nm probe laser. Nevertheless, if the frequency of the 480 nm laser was varied in Channel A across the EIT transmission peak, matching variation in the nominal probe absorption was detected, as shown in Fig. 7.8(b), indicating the presence of atoms prepared in a Rydberg-dressed dark state from Channel A. In Fig. 7.8(c), we show that as the channels are moved further apart, the detected EIT peak in channel B decreases in amplitude. This result is supported by the numerical model and is qualitatively explained by the correlation of larger values of D with higher average transverse speed v_x of the detected Rydberg atom population. Because the readout channel has a fixed width, a higher transverse speed results in a reduced readout interrogation time and a decrease in signal amplitude.

While this observation of the flight of room-temperature Rydberg-dressed atoms between two channels is a necessary first step for spatially-separated Ramsey interrogation, the setup is not yet optimized to achieve a sufficient signal-to-noise ratio to observe a Ramsey fringe experimentally. Additionally, laser frequency and optical path-length stabilization concerns must be addressed in order to stabilize the anticipated Ramsey phase.

7.7 Temporally separated measurements

For the temporally separated measurements, the 780 nm laser was locked to the ^{85}Rb Doppler-free saturation spectroscopy F= 2 co 3 peak, and the 480 nm laser was locked to the n = 45 $D_{5/2}$ EIT peak. The vapor cell was encased in magnetic shielding and heated to 50^{o}C.

Both lasers were pulsed simultaneously using two synchronized acousto-optic modulators (AOMs) driven by a 10 kHz square-wave signal with a variable duty cycle, allowing control of the dark time t_2. The coupling and probe powers were 35 mW and 250 μW, respectively.

Fig. 7.9 (a) shows the balanced detection scheme implemented in these measurements. One channel is overlapped with the coupling laser, and the other is not, so we are sensitive to only changes in EIT absorption. The balanced photodiode output exhibited transient artifacts during the first 200 ns of the pulse rise and fall times, which obscured potential Ramsey dynamics. To mitigate this effect, time traces were recorded both with and without the coupling beam present, and the resulting signals were subtracted to isolate the EIT-related contribution.

The first test in this setup was measuring the effective coherence lifetime under pulsed excitation. The 10 kHz square pulse simultaneously switched both AOMs, preparing the atoms in the steady-state EIT dark state. After a variable t_2, only the probe beam was reintroduced to determine whether Rydberg coherence persisted.

Fig. 7.9 (b) shows that although the intrinsic lifetime of the $45D_{5_2}$ state is 50 μs, the detectable coherence decayed on a much shorter timescale of approximately 3 μs. This discrepancy is attributed primarily to the motion of thermal atoms leaving the interaction region. The measured coherence decay time, therefore, establishes an upper bound on experimentally useful dark times. While also not directly related to the Ramsey interrogation scheme, this also shows the maximum time that atoms spend in the Rydberg interaction region, so it is useful for other experiments utlizing Rydberg atoms.

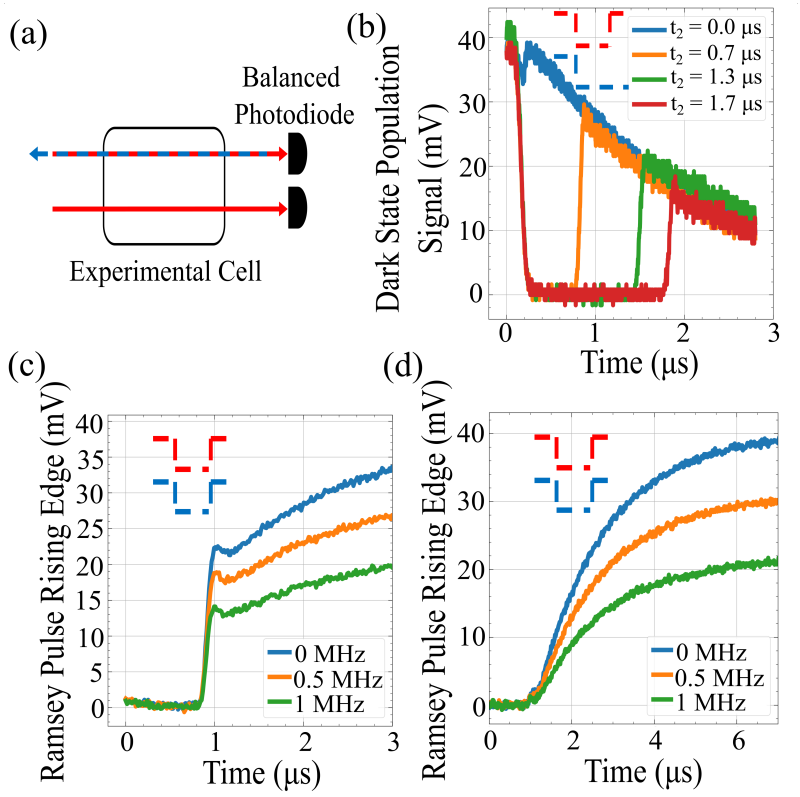

Figure 7.9: Experimental time pulsed signal data: (a) Balanced detection scheme used in experiment. (b) Probing dark state coherence in time. While the lifetime of the state is 53μs, the state decays in about 3 μs, most likely due to atoms leaving the interaction region. (c) Ramsey style pulse as an attempt to see changes based on detuning of the laser fields for a short dark time (t_2 = 1μs). (d) Ramsey style pulse as an attempt to see changes based on detuning of the laser fields for a long dark time (t_2 = 17μs). Since all the atomic coherence decays for this long dark time, this shows the standard rise of the EIT signal.

After this initial test, we attempted to reproduce the detuning-dependent temporal response predicted in Fig. 7.2 (b). For a fixed t_2, the model predicts that the transient response after reintroducing the optical fields should depend on two-photon detuning. To vary the detuning, both laser fields remain frequency-locked as before, and the probe detuning was adjusted by varying an rf-drive frequency supplied to the AOM. In practice, this method introduced many technical challenges. Changes in the rf-frequency produced slight beam displacement as we did not double-pass the AOM, and there were also some power fluctuations. To compensate, the probe power before the vapor cell was actively readjusted for each detuning value, and the balance between the detection channels was

changed after the beam displacer.

Fig. 7.9 (c-d) shows a representative plot of the time-domain EIT signals for two dark times. Fig. 7.9 (c) is the atomic response for $t_2 = 1\mu$s. With this short dark time, the coherence is still present in the interaction channel, apparent by the sharp rise in the signal when the light fields are turned back on. This is the same as Fig. 7.2 (b), where the optical fields re-establish the coherence, but instead of monitoring the decay from the excited state after this initial rise, now the presence of the blue laser continues to re-establish the overall level of EIT. However, unlike the expected response of the atoms from the numerical modeling, all the responses look nearly identical with no notable fringe pattern in the signal.

Fig. 7.9 (d) is another example of changing the detuning of the laser field now with the dark time $t_2 = 17\mu$s. Here this is long enough that all the atomic coherence has decayed as indicated from all the traces starting from the 0 mV level. Again, while not useful for Ramsey fringe measurements, we can see the characteristic time it takes to establish the EIT conditions ~ 6 μs.

To improve signal detuning stability and enhance sensitivity to transient features, a boxcar integrator was used to reproduce fringes in the numerical results of Fig. 7.3 (d). The working principle of a boxcar integrator is that it averages a lot of samples in time for a set time frame. For example, Fig. 7.10 (a) shows a 20 ns integration window indicated by narrow pulses in the blue, orange and green curves. The dark blue curve indicates the pulse of the blue light in the Ramsey time sequence. The boxcar integrator is able to average signals in that fixed time of the laser pulse so we can have a running average of values as we sweep the blue laser detuning.

With this piece of equipment, we try to reproduce curves for the temporal Ramsey sequence as shown in Fig. 7.3 (d). We do this boxar integration at three temporal regions along the pulse sequence to observe dynamics for (1) the steady-state region, to verify consistent EIT peak amplitude across measurements, (2) the initial rise following pulse turn-on, where Ramsey-type interference is expected, and (3) a later time point, to probe

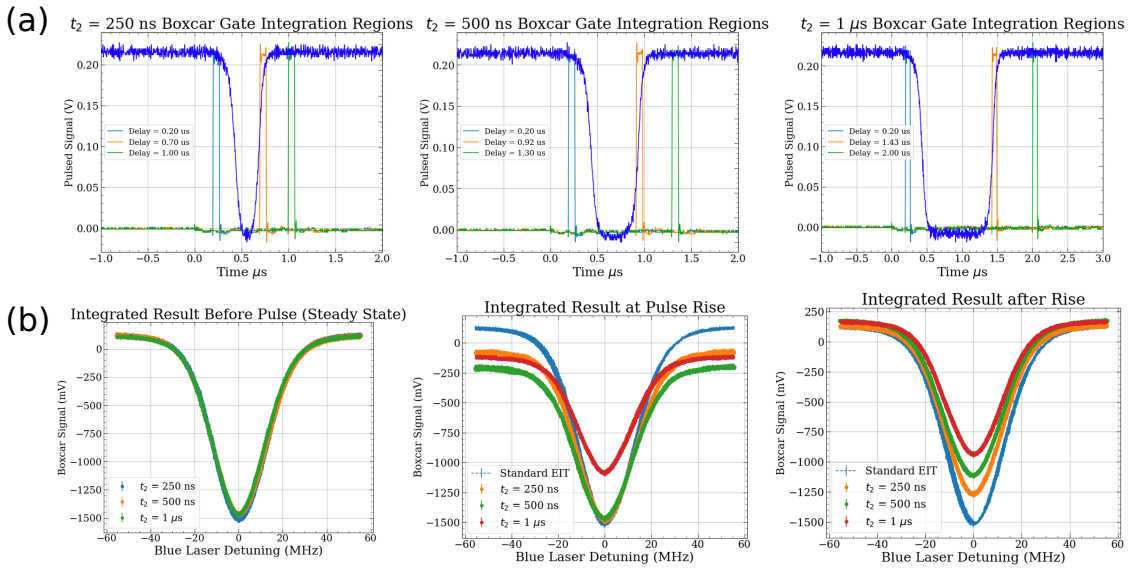

Figure 7.10: Time pulse fringe recreation: a.) Boxcar signal integration region of interest. The regions probed in each are the steady state regime, the rise of the pulse turn on, and a time shortly after the rise time of the laser. b.) Boxcar averaged signal. In the steady state region, along the rise, and at the last position for each graph.

possible delayed dynamics. Fig. 7.10 (b) shows the resulting integration signals. For the stead state integration window, all the curves lie on top of one another, showing that for all pulse durations, we return to the steady state EIT condition before the laser is turned off. In the integration at the pulse rise, we see that all the curves come back, but now they are offset based on the dark time t_2, mot likely due to the decay of the atomic coherence in the intermediate excited state. Finally, if we integrate these signals for some time after the blue laser is reestablished, we see that there EIT peak comes back, but all the traces come back to a different level. While this is exciting on its own because it shows some dynamics of atoms decaying and being probed for various decay times, there are no fringes in the recreated boxcar traces.

Several experimental limitations likely suppress the observable Ramsey signal. First, the AOM rise and fall times (150 ns) deviate significantly from the ideal square pulses assumed in the model, effectively smoothing the temporal phase evolution and reducing fringe contrast. Second, uncontrolled optical phase variations between pulses may wash

out the coherent phase accumulation necessary for fringe formation. Third, the predicted effect is intrinsically weak, and the residual technical noise may obscure small modulation signals. Finally, the available coupling-laser power limits the achievable Rabi frequency. With access to a higher-powered blue laser, the stronger coupling fields would increase the prepared coherence and potentially enhance the Ramsey contrast.

Although Ramsey fringes were not observed in this preliminary experiment, these measurements establish the relevant coherence timescales and identify the principal technical constraints that must be addressed in future experiments.

7.8 Summary

In this Chapter we developed a model for Rydberg Raman-Ramsey (R^3) EIT resonances by calculating the atomic response due to the repeated interactions with two optical fields in two-photon Raman resonances. We focused on the effect of the atomic motion on the resulting narrow spectral feature for both spatially and temporally separated interaction regions.

We predict that even for thermal atoms, it should be possible to observe R^3 resonances in the temporal and spatially separated cases, even with the inclusion of decoherence mechanisms due to laser linewidths. However, preliminary experimental arrangements prove that these resonances are either too small for detection, or do not appear because of other phase and timing instabilities.

Chapter 8

Conclusion and future work

The primary focus of this work is the non-invasive diagnostics of an electron beam. To achieve this, we developed two spatial mapping protocols based on probe-laser transmission and fluorescence. With the fluorescence technique we were able to reconstruct the center-of-mass beam position to within 8 μm, determine the beam width to within 100 μm, and measure the beam current in a simultaneous measurement. For the transmission measurement we performed similar diagnostics with more coarse precision, but were able to reconstruct a two-dimensional beam profile.

Developed in collaboration with NIST, the fluorescence based detection protocol has already proven valuable for rf-field sensing applications and cell charging studies [56, 103, 110, 129]. Our lab continues to improve fluorescence imaging and has recently demonstrated its use for non-invasive plasma diagnostics [121]. Ongoing work aims to extend this technique to magnetic-field imaging. In the future, this approach may enable a variety of spatially resolved field measurements, including traceable laser-intensity profiling.

Transmission-based measurements of spatially varying fields were also a major effort described in this dissertation. Although these results are more challenging to interpret than the fluorescence measurements, the technique offers advantages for studying the time dynamics of spatially varying charges and can be implemented in environments where cameras are impractical.

On the more fundamental side of Rydberg measurements, we explored a new detection protocol based on Ramsey interrogation. While our initial implementation did not yield the desired results of observed narrow fringes, Ramsey interrogation of Rydberg atoms has been realized using rf puled fields [130]. Our work is not cited in this study, but success gives hope that future Ramsey interrogation schemes may still be feasible.

Finally, we started work towards dc electric-field vector electrometry. While the concept itself is not new, we demonstrated that tracking state populations through the contrast of different EIT fringes can reveal the orientation of an electric field. This remains an active area of current research in the lab, and we are extending these efforts by incorporating external magnetic fields to gain further insight into field direction like other groups are doing for rf fields [119].

We have covered a lot of ground in starting the Rydberg sensing program at William & Mary, and while my time here is coming to a close, there is always another five papers worth of ideas and applications of the work presented here looming around the corner.

Appendix A

Frequency mismatch scaling

One consequence of the large wavelength difference between the probe and coupling laser fields for EIT excitation is that the observed atomic resonance spacing must be scaled depending on which laser is frequency scanned. The most common way this presents itself in our experiments is through the frequency spacing of the fine structure EIT peaks ($n\mathrm{D}_{5/2}$ and $n\mathrm{D}_{3/2}$).

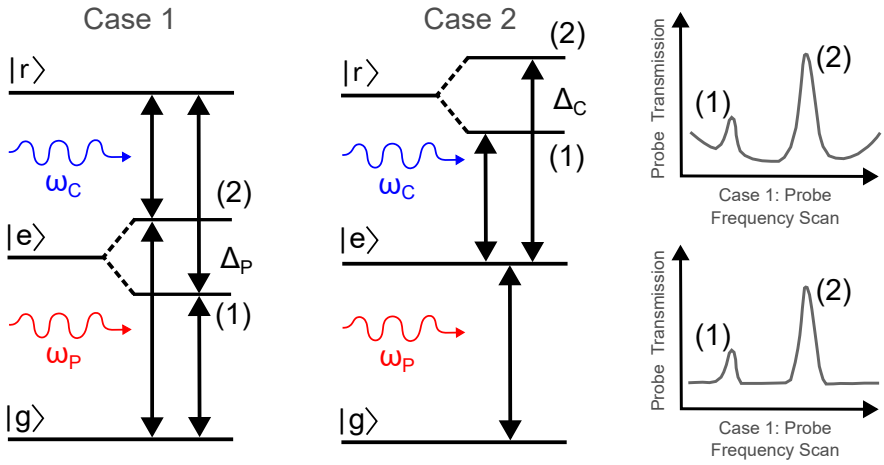

Figure A.1: Cases for scanning different laser fields for excitation to the Rydberg state in a two-photon excitation scheme. Case 1: The probe laser frequency is scanned for a fixed coupling laser detuning. The fine structure states of an nD Rydberg energy level sit on top of the Doppler broadened background, and the frequency spacing between these energy levels must be calibrated for scanning the probe laser. Case 2: The coupling laser frequency is scanned for a fixed probe laser detuning. Here, the fine structure level spacing does not have to be adjusted as the spacing is calculated with ARC.

Fig. A.1 shows the two possible cases of sweeping each laser field. In the case where the coupling laser detuning is held constant, and the probe laser field is scanned (Case 1), the fine structure EIT peaks are on the varying Doppler background, and for a known energy level spacing of the fine structure Rydberg states, the frequency axis should be scaled as

$$\Delta'_{Meas} = \Delta_{Meas}(1 - \frac{\lambda_C}{\lambda_P}), \tag{A.1}$$

where Δ_{Meas} is the measured frequency separation of the two peaks, and $\lambda_{P,C}$ are the wavelengths of the probe and coupling field, respectively [2].

Alternatively, in (Case 2) where the coupling laser is frequency scanned, there is no need to scale the frequency axis, as the splittings between the fine structure levels are known and calculated with ARC [4].

However, another way this has presented itself in our experiment is through measuring the transitions to the Rydberg state from other fine structure F states in ^{85}Rb. Fig. A.2 shows a typical measured EIT transmission curve sweeping the coupling laser detuning for the 36D state. Here, the two large peaks are the fine structure Rydberg states that have a known frequency separation of 256 MHz. There is another smaller peak near 100 MHz that was a mystery for a long time. The frequency separation between the $F = 4$ and $F = 3$ states of ^{85}Rb $5P_{3/2}$ is 120 MHz [131], so at the surface, this peak looks like it corresponds to nothing. However, if you account for the frequency scaling, for the intermediate excited state populations while sweeping the coupling laser,

$$\Delta'_{Meas} = \Delta_{Meas}(1 - \frac{\lambda_C}{\lambda_P}), \tag{A.2}$$

then the splitting of the $F = 4$ and $F = 3$ states is 75 MHz and lines up with this mysterious peak. So, through using this frequency scaling argument, we found this peak corresponds to driven Rydberg transitions from the $F = 3$ state of ^{85}Rb $5P_{3/2}$, when we usually drive it from the $F = 4$ state with larger contrast. Table A.1 shows how to adjust

spacing between states for different splittings in the ground, excited, and Rydberg states for different laser sweeps.

	Ground state splitting	Excited state splitting	Rydberg state splitting
Case 1 (probe scans, coupling fixed)	1	$1 - \frac{\lambda_C}{\lambda_P}$	$\frac{\lambda_C}{\lambda_P}$
Case 2 (probe fixed, coupling scans)	$\frac{\lambda_P}{\lambda_C}$	$1 - \frac{\lambda_P}{\lambda_C}$	1

Table A.1: Frequency scaling factors for mismatched ladder system adapted from [2].

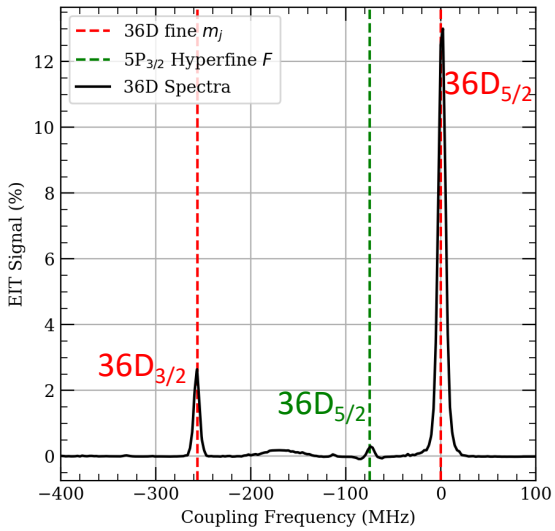

Figure A.2: Example EIT transmission spectra sweeping the coupling laser field. The black line is the recorded spectra for the 36D Rydberg state. The two large peaks are the fine structure states with a known frequency separation of 256 MHz. The small peak corresponds to the $36D_{5/2}$ Rydberg transition from the $F = 3$ state of ^{85}Rb $5P_{3/2}$. Here, because we scan the coupling laser, the frequency difference between the different F states must be scaled to know the frequency spacing between the two $D_{5/2}$ states.

Appendix B

Electron beam operation procedure

To preserve the cathode filament, there is a procedure to turn the electron gun apparatus on and off.

To turn the electron beam on the procedure is :

1. Monitor the pressure readings. This should be below $5 \times 10^{-}6$ Torr.
2. Increase the filament current to 1 A in 30 seconds.
3. Increase the voltage to 5 keV in 20 seconds.
4. Increase the filament current to 1.5 A in 30 seconds.
5. Increase the voltage to 10 keV in 20 seconds.
6. Increase the filament current to 2 A in 30 seconds.
7. Increase the voltage to 15 keV in 20 seconds.
8. Increase the filament current to 2.5 A in 60 seconds.
9. Increase the voltage to 20 keV in 30 seconds.
10. Monitor the pressure and it should be near the original pressure.
11. Increase the current to 2.8 A in an interval of 30 seconds in steps of 0.1 A.
12. Increase the current to 3 A in an interval of 30 seconds in steps of 0.1 A.
13. The Faraday cup and emission current should read between 50 μA to 100 μA.

14. After achieving 3 A the steps should be in the 0.05 A.

Notes:

Above 3.3 A current reduces the filament lifetime, and this Faraday cup can't handle that much current.

The pressure readings will change for current above 3 A, but it shouldn't exceed $5 \times 10^{-}6$ Torr, unless you are filling with some injected gas.

Turning Off:

1. Reduce the current to 0 A, no need to take your time with this.
2. Reduce the voltage, no need to take your time with this.

When trying to focus the beam, this is a difficult procedure as all the parameters contribute to beam shape. As a baseline of operating parameters set by the factory, the manual for our source shows:

Energy [kV]	Filament Current [A]	Focus [div.]	Grid [div]	Emission Current [μA]
10.0	3.25	2.18	2.60	1
			2.46	10
			2.12	100
			1.34	500
20.0	3.25	3.70	4.24	1
			4.08	10
			3.60	100
			2.24	500
			1.32	1000
30.0	3.25	5.0	5.68	1
			5.48	10
			4.80	100
			2.78	500
			1.60	1000

Table B.1: Power supply settings for focused beam

Appendix C

Electron beam pulser alignment procedure

Terminology:

E-Beam Deflection Coils: x and y control from e-gun controller

Pulser Deflection Coils: x and y control on pulser controller

Focus: Focus of electron gun on e-gun controller

Grid: Electron acceleration control on e-gun controller

Diagnostic Tools:

Optical Transition Radiation (OTR) Screen: Copper imaging plane in vacuum system

Ethernet Camera: USB camera leads to poor hot pixels and inconsistent background

Procedure that worked:

1.) Insert OTR screen in vacuum chamber after pulser aperture. This is on a rotation mount with the black knob under the pressure gauge on the Rydberg QET setup. The copper screen will block the beam path through the vacuum system. Set up an imaging system at the viewing port looking at this plate. Set the e-beam deflection coils and pulser deflection coils to 5.0 on the x and y potentiometers, and the Focus and Grid settings to the STAIB recommended values.

2.) With a friend or viewing the OTR screen on the camera monitor, use the E-Beam

Deflection coils to maximize the signal on the OTR screen (by eye this signal looks like a tiny white spot on the copper plate).

3.) Once a good signal is achieved on the OTR screen, adjust the focus and grid parameters with the E-Beam deflection coils X and Y locked, monitoring the beam size with the imaging system.

4.) Move the OTR screen out of the way so it is no longer blocking the beam, and check the Faraday cup signal using the Pulser Deflection coils to maximize the signal.

5.) Once the Faraday cup signal is maximized, keep checking the signal on the OTR screen to make sure it is not moving a lot, and you can still image the beam spot with the imaging system.

6.) After maximizing the OTR signal and Faraday cup, move the imaging system to image the electron beam with the Rubidium Fluorescence.

7.) Fluorescence images done for this work were done with the heater/cell temperature at 50C, and 30 s exposure time with an average of 10 frames.

8.) To see fluorescence, you have to take a background image and subtract the signal image (roughly 10 counts/ 100 uA emission current).

Appendix D

Pulsing electron beam temporal dynamics

Early transmission measurements required a robust understanding to distinguish the primary e-beam signal from parasitic charging in the Rb chamber. We controlled two primary parameters to isolate these components, the pulse duty cycle and the pulse repetition rate.

While this was about a year of work and many methods were tried to de-convolve these charging systems, in this Appendix we only give a brief overview of some of the main findings. However, in addition to this optimization of e-beam pulse settings, we also tried to study temporal dynamics (i.e. characteristic timescales of the e-beam and chamber charging dynamics). However, these measurements never really gave any insight into these characteristics due to reproducibility issues, and therefore should be the center of studies moving forward with this apparatus.

Initially, we implemented the pulser to minimize the e-beam's presence in the chamber, thereby suppressing spurious charging and isolating the e-beam induced signal. As shown in Fig. D.1 (a 1-3), reducing the duty cycle directly limits the time the chamber is exposed to the e-beam. For these plots, when the signal is non-zero, this is when the beam is in the chamber for a set pulse length duration. For measurement of the electron beam, Fig. D.1 (b 1-3) shows a horizontal cross section of the e-beam using transmission-based

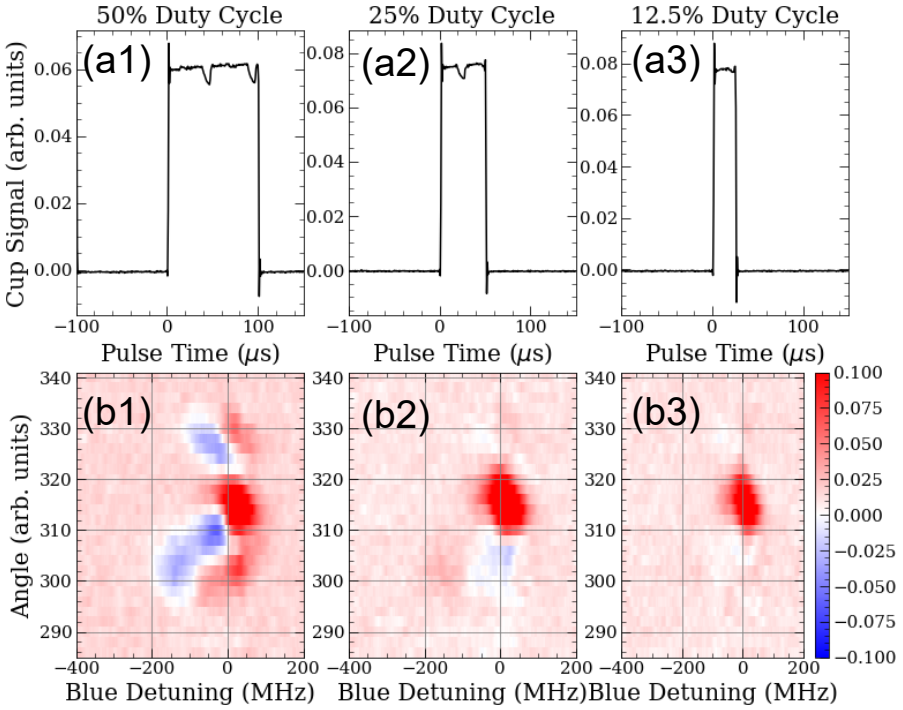

Figure D.1: Effect of duty cycle on measured e-beam position measurements. (a 1-3) Signal at the Faraday cup for different duty cycles to show the electron beam is present in the chamber for less time with reducing duty cycle. (b 1-3) Corresponding signal of e-beam cross section for changing horizontal displacement of laser beams. As the duty cycle decreases, the blue part of the graph goes away, which is attributable to less charging in the chamber.

measurements for varied duty cycles. The (a) and (b) labels correspond to the different (1-3) cases of reduced duty cycle. In this cross section, the central red dot, the center of the electron beam, is present in all three cases. This means that for the lower duty cycle, we are isolating the e-beam signal from parasitic charging effects, the blue signal in the 50 % duty cycle measurement.

While this was a promising step, it is difficult to prove that this signal is truly due to the electron beam, because it could be the case that we are just no longer integrating long enough to see the background signal, and it is still there. As such, for all tests, we just use the 50 % duty cycle when pulsing the e-beam and know that there is residual charging in the chamber.

The duty cycle changes the strength of the varied signal, but the pulse repetition rate

also plays a crucial role in charge mitigation. Fig D.2 shows measured e-beam cross sections for varying pulse repetition rates. If the pulse speed is too low, the beam will appear to be CW to the chamber where it is fully charged, and if the pulse speed is too fast, then the beam is also CW to the chamber because it never has a chance to turn off. In Fig D.2, as the pulse speed increases, so does the strength of the signal. More importantly, notice that the central e-beam signal increases, but the background charge signal increases as well.

Again, a more detailed study on the time dynamics is necessary to fully understand what is charging, how fast the atoms respond to the presence of the electron beam, and many other factors that go into what the recorded lock-in signal is influenced by, however, we found that pulsing the e-beam at 5 kHz gives us a good balance between charging and data acquisition time. These were the considerations we used in choosing a pulse speed, and data acquisition protocol.

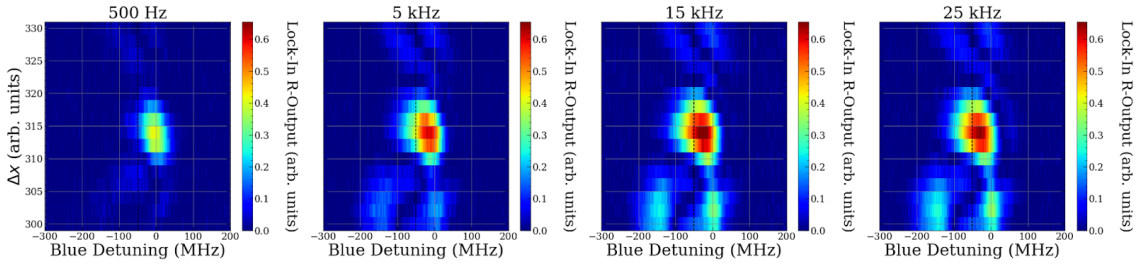

Figure D.2: Effect of pulse repetition rate on measured e-beam cross sections. As the pulse speed increases, the signal grows stronger. This might be due to charging the chamber, where now the signal is modulated on top of a constant background the more the e-beam behaves as a CW source.

References

[1] T. F. Gallagher, *Rydberg Atoms*, Cambridge Monographs on Atomic, Molecular and Chemical Physics (Cambridge University Press, 1994).

[2] L. Ma, *Electromagnetic Field Sensing with Rydberg Atoms in Vapor Cells*, Ph.D. thesis, University of Michigan (2021).

[3] A. Duspayev, *Precision Measurements and Quantum Sensing Using Cold Atoms*, Ph.D. thesis, University of Michigan (2024).

[4] N. Šibalić, J. Pritchard, C. Adams, and K. Weatherill, Arc: An open-source library for calculating properties of alkali rydberg atoms, Computer Physics Communications **220**, 319 (2017).

[5] V. Teotia, S. Malhotra, P. Ukarde, K. Singh, J. Itteera, P. Kumar, A. K. Sinha, S. K. Gupta, Y. K. Taly, and P. Singh, Rf cavity design and qualification for proton accelerator, in *2014 International Symposium on Discharges and Electrical Insulation in Vacuum (ISDEIV)* (2014) pp. 641–643.

[6] V. Teotia, S. Malhotra, P. Kumar, E. Mishra, S. Meshram, and R. Chimurkar, 11–20 mev alvarez drift tube linac for low energy proton accelerator, Journal of Instrumentation **18** (06), P06020.

[7] R. C. Davidson and Q. Hong, *Physics of intense charged particle beams in high energy accelerators* (World Scientific, 2001).

[8] M. Reiser, *Theory and design of charged particle beams* (John Wiley & Sons, 2008).

[9] J. Goree, Charging of particles in a plasma, Plasma Sources Science and Technology **3**, 400 (1994).

[10] R. Bingham, J. Mendonca, and P. K. Shukla, Plasma based charged-particle accelerators, Plasma physics and controlled fusion **46**, R1 (2004).

[11] M. Jana, A. Sen, and P. Kaw, Collective effects due to charge-fluctuation dynamics in a dusty plasma, physical review E **48**, 3930 (1993).

[12] Y. Xu, A general comparison between tokamak and stellarator plasmas, Matter and Radiation at Extremes **1**, 192 (2016).

[13] J. Harris, Small to mid-sized stellarator experiments: topology, confinement and turbulence, Plasma physics and controlled fusion **46**, B77 (2004).

[14] R. L. Stenzel, A new probe for measuring small electric fields in plasmas, Review of Scientific Instruments **62**, 130 (1991).

[15] N. Jelić, K.-U. Riemann, T. Gyergyek, S. Kuhn, M. Stanojević, and J. Duhovnik, Fluid and kinetic parameters near the plasma-sheath boundary for finite debye lengths, Physics of Plasmas **14**, 103506 (2007).

[16] Y. Gao and I. Wolff, Miniature electric near-field probes for measuring 3-d fields in planar microwave circuits, IEEE Transactions on microwave theory and techniques **46**, 907 (1998).

[17] D. Scheller, F. Hrunski, J. Schwarberg, W. Knolle, Ö. Soykal, P. Udvarhelyi, P. Narang, H. Weber, M. Hollendonner, and R. Nagy, Quantum-enhanced electric field mapping within semiconductor devices, Physical Review Applied **24**, 014036 (2025).

[18] Z. Han, F. Xue, J. Hu, and J. He, Micro electric field sensors: Principles and applications, IEEE Industrial Electronics Magazine **15**, 35 (2021).

[19] J. D. Jackson, *Classical Electrodynamics* (Wiley, 1998).

[20] L. Cui, Z. Zhang, N. Gao, Z. Meng, and Z. Li, Radio frequency identification and sensing techniques and their applications—a review of the state-of-the-art, Sensors **19**, 4012 (2019).

[21] C. Occhiuzzi, S. Caizzone, and G. Marrocco, Passive uhf rfid antennas for sensing applications: Principles, methods, and classifcations, IEEE Antennas and Propagation Magazine **55**, 14 (2013).

[22] A. Rüfenacht, N. E. Flowers-Jacobs, and S. P. Benz, Impact of the latest generation of josephson voltage standards in ac and dc electric metrology, Metrologia **55**, S152 (2018).

[23] A. Röfenacht, A. E. Fox, R. L. Johnson-Wilke, B. T. Scheck, P. D. Dresselhaus, and S. P. Benz, Dual-frequency-bias programmable josephson voltage standard circuit, IEEE Transactions on Instrumentation and Measurement (2025).

[24] H. B. Dang, A. C. Maloof, and M. V. Romalis, Ultrahigh sensitivity magnetic field and magnetization measurements with an atomic magnetometer, Applied Physics Letters **97**, 151110 (2010).

[25] B. Liu, L. Zhang, Z. Liu, Z. Deng, D. Ding, B. Shi, and G. Guo, Electric field measurement and application based on rydberg atoms, Electromagnetic Science **1**, 1 (2023).

[26] R. Finkelstein, S. Bali, O. Firstenberg, and I. Novikova, A practical guide to electromagnetically induced transparency in atomic vapor, New Journal of Physics **25**, 035001 (2023).

[27] N. Schlossberger, N. Prajapati, S. Berweger, A. P. Rotunno, A. B. Artusio-Glimpse, M. T. Simons, A. A. Sheikh, E. B. Norrgard, S. P. Eckel, and C. L. Holloway, Rydberg states of alkali atoms in atomic vapour as si-traceable field probes and communications receivers, Nature Reviews Physics **6**, 606 (2024).

[28] M. T. Simons, A. B. Artusio-Glimpse, A. K. Robinson, N. Prajapati, and C. L. Holloway, Rydberg atom-based sensors for radio-frequency electric field metrology, sensing, and communications, Measurement: Sensors **18**, 100273 (2021).

[29] M. T. Simons, J. A. Gordon, and C. L. Holloway, Fiber-coupled vapor cell for a portable rydberg atom-based radio frequency electric field sensor, Appl. Opt. **57**, 6456 (2018).

[30] P. K. Elgee, J. C. Hill, K.-J. E. LeBlanc, G. D. Ko, P. D. Kunz, D. H. Meyer, and K. C. Cox, Satellite radio detection via dual-microwave rydberg spectroscopy, Applied Physics Letters **123**, 084001 (2023).

[31] C. T. Fancher, D. R. Scherer, M. C. S. John, and B. L. S. Marlow, Rydberg atom electric field sensors for communications and sensing, IEEE Transactions on Quantum Engineering **2**, 1 (2021).

[32] H. Fan, S. Kumar, J. Sedlacek, H. Kübler, S. Karimkashi, and J. P. Shaffer, Atom based rf electric field sensing, Journal of Physics B: Atomic, Molecular and Optical Physics **48**, 202001 (2015).

[33] N. Thaicharoen, K. R. Moore, D. A. Anderson, R. C. Powel, E. Peterson, and G. Raithel, Electromagnetically induced transparency, absorption, and microwave-field sensing in a rb vapor cell with a three-color all-infrared laser system, Phys. Rev. A **100**, 063427 (2019).

[34] J. A. Gordon, M. T. Simons, A. H. Haddab, and C. L. Holloway, Weak electric-field

detection with sub-1 hz resolution at radio frequencies using a rydberg atom-based mixer, AIP Advances **9**, 045030 (2019).

[35] Y.-Y. Jau and T. Carter, Vapor-cell-based atomic electrometry for detection frequencies below 1 khz, Phys. Rev. Appl. **13**, 054034 (2020).

[36] M. T. Simons, J. A. Gordon, C. L. Holloway, D. A. Anderson, S. A. Miller, and G. Raithel, Using frequency detuning to improve the sensitivity of electric field measurements via electromagnetically induced transparency and autler-townes splitting in rydberg atoms, Applied Physics Letters **108**, 174101 (2016).

[37] C. L. Holloway, M. T. Simons, J. A. Gordon, A. Dienstfrey, D. A. Anderson, and G. Raithel, Electric field metrology for si traceability: Systematic measurement uncertainties in electromagnetically induced transparency in atomic vapor, Journal of Applied Physics **121**, 233106 (2017).

[38] C. L. Holloway, J. A. Gordon, A. Schwarzkopf, D. A. Anderson, S. A. Miller, N. Thaicharoen, and G. Raithel, Sub-wavelength imaging and field mapping via electromagnetically induced transparency and autler-townes splitting in rydberg atoms, Applied Physics Letters **104**, 244102 (2014).

[39] N. Schlossberger, N. Prajapati, S. Berweger, A. P. Rotunno, A. B. Artusio-Glimpse, M. T. Simons, A. A. Sheikh, E. B. Norrgard, S. P. Eckel, and C. L. Holloway, Rydberg states of alkali atoms in atomic vapour as si-traceable field probes and communications receivers, Nature Reviews Physics , 1 (2024).

[40] L. Ma, M. A. Viray, D. A. Anderson, and G. Raithel, Measurement of dc and ac electric fields inside an atomic vapor cell with wall-integrated electrodes, Phys. Rev. Appl. **18**, 024001 (2022).

[41] J. Ramette, J. Sinclair, Z. Vendeiro, A. Rudelis, M. Cetina, and V. Vuletić, Any-

to-any connected cavity-mediated architecture for quantum computing with trapped ions or rydberg arrays, PRX Quantum **3**, 010344 (2022).

[42] M. Saffman, Quantum computing with atomic qubits and rydberg interactions: progress and challenges, Journal of Physics B: Atomic, Molecular and Optical Physics **49**, 202001 (2016).

[43] Y. Liu, Y. Sun, Z. Fu, P. Xu, X. Wang, X. He, J. Wang, and M. Zhan, Infidelity induced by ground-rydberg decoherence of the control qubit in a two-qubit rydberg-blockade gate, Phys. Rev. Appl. **15**, 054020 (2021).

[44] X. Wu, X. Liang, Y. Tian, F. Yang, C. Chen, Y.-C. Liu, M. K. Tey, and L. You, A concise review of rydberg atom based quantum computation and quantum simulation*, Chinese Physics B **30**, 020305 (2021).

[45] L. Li and A. Kuzmich, Quantum memory with strong and controllable rydberg-level interactions, Nature Communications **7**, 13618 (2016).

[46] S. Shi, B. Xu, K. Zhang, G.-S. Ye, D.-S. Xiang, Y. Liu, J. Wang, D. Su, and L. Li, High-fidelity photonic quantum logic gate based on near-optimal rydberg single-photon source, Nature Communications **13**, 4454 (2022).

[47] N. Schlossberger, A. P. Rotunno, S. P. Eckel, E. B. Norrgard, D. Manchaiah, N. Prajapati, A. B. Artusio-Glimpse, S. Berweger, M. T. Simons, D. Shylla, W. J. Watterson, C. Patrick, A. Meraki, R. Talashila, A. Younes, D. S. La Mantia, and C. L. Holloway, Primary quantum thermometry of mm-wave blackbody radiation via induced state transfer in rydberg states of cold atoms, Phys. Rev. Res. **7**, L012020 (2025).

[48] X. Lu, Y. Sun, and H. Metcalf, Rydberg atom spectroscopy enabled by blackbody radiation ionization, Phys. Rev. A **84**, 033402 (2011).

[49] W. An, Z. Wang, A. Weisenburger, and G. Mueller, Laser-induced fluorescence-dip spectroscopy of rydberg states of xenon for electric field measurement in plasma, Review of Scientific Instruments **93**, 023503 (2022).

[50] C. H. Ching, J. E. Bailey, P. W. Lake, A. B. Filuk, R. G. Adams, and J. McKenney, Absorption spectroscopy characterization measurements of a laser-produced na atomic beam, Review of Scientific Instruments **68**, 354 (1997).

[51] B. A. Knyazev, W. An, and H. Bluhm, Stark spectroscopy of a probe lithium beam excited with two dye lasers as a technique to study a high-power ion-beam diode, Review of Scientific Instruments **83**, 033101 (2012).

[52] L. Li, Y. Jiao, J. Hu, H. Li, M. Shi, J. Zhao, and S. Jia, Super low-frequency electric field measurement based on rydberg atoms, Opt. Express **31**, 29228 (2023).

[53] L. Ma, E. Paradis, and G. Raithel, Dc electric fields in electrode-free glass vapor cell by photoillumination, Opt. Express **28**, 3676 (2020).

[54] A. Duspayev, R. Cardman, D. A. Anderson, and G. Raithel, High-angular-momentum rydberg states in a room-temperature vapor cell for dc electric-field sensing, Phys. Rev. Res. **6**, 023138 (2024).

[55] N. Schlossberger, A. P. Rotunno, A. B. Artusio-Glimpse, N. Prajapati, S. Berweger, D. Shylla, M. T. Simons, and C. L. Holloway, Zeeman-resolved autler-townes splitting in rydberg atoms with tunable resonances and a single transition dipole moment, Phys. Rev. A **109**, L021702 (2024).

[56] L. Patrick, N. Schlossberger, D. F. Hammerland, N. Prajapati, T. McDonald, S. Berweger, R. Talashila, A. B. Artusio-Glimpse, and C. L. Holloway, Imaging of induced surface charge distribution effects in glass vapor cells used for rydberg atom-based sensors, AVS Quantum Science **7**, 024401 (2025).

[57] J. A. Sedlacek, A. Schwettmann, H. Kübler, and J. P. Shaffer, Atom-based vector microwave electrometry using rubidium rydberg atoms in a vapor cell, Phys. Rev. Lett. **111**, 063001 (2013).

[58] P. K. Elgee, K. C. Cox, J. C. Hill, P. D. Kunz, and D. H. Meyer, Complete three-dimensional vector polarimetry with a rydberg-atom rf electrometer, Phys. Rev. Appl. **22**, 064012 (2024).

[59] R. Mao, Y. Lin, Y. qi Fu, Y. Ma, and K. Yang, Digital beamforming and receiving array research based on rydberg field probes, IEEE Transactions on Antennas and Propagation **72**, 2025 (2024).

[60] A. Gill, A. Buikema, S. Sirisky, and H. Clevenson, Microwave phase mapping and angle-of-arrival detection using rydberg atom-based electrometry (2025), arXiv:2503.22864 [physics.atom-ph] .

[61] C. G. Wade, N. Šibalić, N. R. De Melo, J. M. Kondo, C. S. Adams, and K. J. Weatherill, Real-time near-field terahertz imaging with atomic optical fluorescence, Nature Photonics **11**, 40 (2017).

[62] L. A. Downes, L. Torralbo-Campo, and K. J. Weatherill, A practical guide to terahertz imaging using thermal atomic vapour, New Journal of Physics **25**, 035002 (2023).

[63] L. A. Downes, A. R. MacKellar, D. J. Whiting, C. Bourgenot, C. S. Adams, and K. J. Weatherill, Full-field terahertz imaging at kilohertz frame rates using atomic vapor, Phys. Rev. X **10**, 011027 (2020).

[64] C. L. Holloway, M. T. Simons, A. H. Haddab, C. J. Williams, and M. W. Holloway, A "real-time" guitar recording using rydberg atoms and electromagnetically induced transparency: Quantum physics meets music, AIP Advances **9**, 065110 (2019).

[65] N. Prajapati, A. P. Rotunno, S. Berweger, M. T. Simons, A. B. Artusio-Glimpse, S. D. Voran, and C. L. Holloway, Tv and video game streaming with a quantum receiver: A study on a rydberg atom-based receiver's bandwidth and reception clarity, AVS Quantum Science **4**, 035001 (2022).

[66] N. Schlossberger, T. McDonald, N. Prajapati, and C. L. Holloway, Rydberg atom reception of a handheld uhf frequency-modulated two-way radio, Phys. Rev. Appl. **25**, 024031 (2026).

[67] M. Lei, J. Zhang, Q. Luo, Z. Zhang, M. Wang, and M. Shi, Satellite signal detection via rydberg-atom receiver (2025), arXiv:2506.15439 [quant-ph] .

[68] D. A. Anderson, G. Raithel, M. Simons, and C. L. Holloway, Quantum-optical spectroscopy for plasma electric field measurements and diagnostics (2017), arXiv:1712.08717 [physics.atom-ph] .

[69] K. Cox, V. I. Yudin, A. V. Taichenachev, I. Novikova, and E. E. Mikhailov, Measurements of the magnetic field vector using multiple electromagnetically induced transparency resonances in Rb vapor, Phys. Rev. A **83**, 015801 (2011), arXiv:1011.0503 [physics.atom-ph] .

[70] I. Novikova, O. Rollins, and E. Mikhailov, Magnetic field direction detection using Electromagnetically Induced Transparency with vector vortex beam (2025).

[71] U. Czarnetzki, D. Luggenhölscher, and H. F. Döbele, Sensitive electric field measurement by fluorescence-dip spectroscopy of rydberg states of atomic hydrogen, Phys. Rev. Lett. **81**, 4592 (1998).

[72] P. B. Weichman, Doppler sensitivity and resonant tuning of rydberg atom-based antennas, Journal of Physics B: Atomic, Molecular and Optical Physics **57**, 165501 (2024).

[73] S. M. Bohaichuk, F. Ripka, V. Venu, F. Christaller, C. Liu, M. Schmidt, H. Kübler, and J. P. Shaffer, Three-photon rydberg-atom-based radio-frequency sensing scheme with narrow linewidth, Phys. Rev. Appl. **20**, L061004 (2023).

[74] J. Glick, B. E. Anderson, T. N. Nunley, J. Bingaman, J. J. Liu, D. H. Meyer, and P. Kunz, Doppler-free rydberg spectroscopy in a warm vapor, Phys. Rev. A **112**, 063726 (2025).

[75] N. Prajapati, S. Berweger, A. P. Rotunno, A. B. Artusio-Glimpse, N. Schlossberger, D. Shylla, W. J. Watterson, M. T. Simons, D. LaMantia, E. B. Norrgard, S. P. Eckel, and C. L. Holloway, Investigation of fluorescence versus transmission readout for three-photon rydberg excitation used in electrometry, AVS Quantum Science **6**, 034401 (2024).

[76] J. R. Johansson, P. D. Nation, and F. Noriac, Qutip 2: A python framework for the dynamics of open quantum systems, Computer Physics Communications **184**, 1234 (2013).

[77] B. N. Miller, D. H. Meyer, C. A. Montag, O. Nagib, T. Virtanen, P. K. Elgee, and K. C. Cox, Rydiqule version 2: Enhancing graph-based modeling of rydberg atoms, arXiv preprint arXiv:2510.21628 (2025).

[78] A. P. Rotunno, A. K. Robinson, N. Prajapati, S. Berweger, M. T. Simons, A. B. Artusio-Glimpse, and C. L. Holloway, Inverse transform sampling for efficient Doppler-averaged spectroscopy simulations, AIP Advances **13**, 075218 (2023).

[79] H. Fan, *Microwave Electrometry with Rydberg Eletromagnetically Induced Transparency in Vapor Cells*, Ph.D. thesis, University of Oklahoma (2016).

[80] M. Tanasittikosol, *Rydberg Dark States in External Fields*, Ph.D. thesis, Durham University (2011).

[81] M. JAMIESON *et al.*, *Optimizing a Rydberg atom-based terahertz imaging system*, Ph.D. thesis, Durham University (2023).

[82] H.-J. Su, J.-Y. Liou, I.-C. Lin, and Y.-H. Chen, Optimizing the rydberg eit spectrum in a thermal vapor, Opt. Express **30**, 1499 (2022).

[83] M. O. Scully and M. S. Zubairy, *Quantum Optics* (Cambridge University Press, 2001).

[84] M. L. Zimmerman, M. G. Littman, M. M. Kash, and D. Kleppner, Stark structure of the rydberg states of alkali-metal atoms, Phys. Rev. A **20**, 2251 (1979).

[85] N. Prajapati, *Development of Quantum Information Tools Based on Multi-Photon Raman Processes in Rb Vapor*, Ph.D. thesis, The College of William and Mary (2020).

[86] Z. Niu, *Development of Quantum Information and Sensing Tools Based on Four-Wave Mixing in Hot Rubidium Vapor*, Ph.D. thesis, The College of William and Mary (2025).

[87] K. Su, R. Behary, S. Aubin, E. E. Mikhailov, and I. Novikova, Two-photon rydberg eit resonances in non-collinear beam configurations, J. Opt. Soc. Am. B **42**, 757 (2025).

[88] N. Schlossberger, N. Prajapati, A. B. Artusio-Glimpse, S. Berweger, and C. L. Holloway, Fundamental linewidth limit of electromagnetically induced transparency in a thermal rydberg ladder (2026), arXiv:2603.04596 [physics.atom-ph] .

[89] M. Ohring, 11 - electrical properties of metals, insulators, and dielectrics, in *Engineering Materials Science*, edited by M. Ohring (Academic Press, San Diego, 1995) pp. 559–610.

[90] D. Rule, Transition radiation diagnostics for intense charged particle beams, Nuclear Instruments and Methods in Physics Research Section B: Beam Interactions with Materials and Atoms **24-25**, 901 (1987).

[91] R. Singh, T. Reichert, and B. Walasek-Hoehne, Optical transition radiation based transverse beam diagnostics for nonrelativistic ion beams, Phys. Rev. Accel. Beams **25**, 072801 (2022).

[92] A. Salehilashkajani, H. D. Zhang, M. Ady, N. Chritin, P. Forck, J. Glutting, O. R. Jones, R. Kersevan, N. Kumar, T. Lefevre, T. Marriott-Dodington, S. Mazzoni, I. Papazoglou, A. Rossi, G. Schneider, O. Sedlacek, S. Udrea, R. Veness, and C. P. Welsch, A gas curtain beam profile monitor using beam induced fluorescence for high intensity charged particle beams, Applied Physics Letters **120**, 174101 (2022).

[93] D. P. Sandoval, R. C. Garcia, J. D. Gilpatrick, M. A. Shinas, R. Wright, V. Yuan, and M. E. Zander, Fluorescence-based video profile beam diagnostics: Theory and experience, AIP Conf. Proc. **319**, 273 (1994).

[94] C.-V. Meister, P-v.l. ginzburg, v.n. tsytovich: Transition radiation and transition scattering. adam hilger, bristol and new york, 1990, xii+433 s. preis: 70.00 gpf. isbn 0-85274-003-4, Astronomische Nachrichten **316**, 367 (1995), https://onlinelibrary.wiley.com/doi/pdf/10.1002/asna.2103160512 .

[95] N. DeStefano, S. Pegahan, A. Ramaswamy, S. Aubin, T. Averett, A. Camsonne, S. Malinovskaya, E. E. Mikhailov, G. Park, S. Zhang, and I. Novikova, Electron beam characterization via quantum coherent optical magnetometry, Applied Physics Letters **125**, 264001 (2024).

[96] G. Fernqvist, *The historical evolution of the DC Current Transformer (DCCT)*, Tech. Rep. (CERN, 2024).

[97] A. Hofmann, Electron and proton beam diagnostics with synchrotron radiation, IEEE Transactions on Nuclear Science **28**, 2131 (1981).

[98] L. Ponce, R. Jung, and F. Meot, *LHC proton beam diagnostics using synchrotron radiation*, Tech. Rep. (CERN, 2004).

[99] K. Chouffani, F. Harmon, D. Wells, J. Jones, and G. Lancaster, Laser-compton scattering as a tool for electron beam diagnostics, Laser and Particle Beams **24**, 411 (2006).

[100] G. Blair, Laser based beam diagnostics, EUROTeV-Report-2008-027 (2008).

[101] V. Tzoganis, H. D. Zhang, A. Jeff, and C. P. Welsch, Design and first operation of a supersonic gas jet based beam profile monitor, Phys. Rev. Accel. Beams **20**, 062801 (2017).

[102] C. Castro Sequeiro, M. Ady, G. Bregliozzi, N. Chatzigeorgiou, A. R. Churchman, R. Kersevan, T. Lefevre, S. Mazzoni, G. Pigny, A. Rossi, M. Sameed, G. Schneider, O. Sedlacek, K. Sidorowski, C. Vazquez Pelaez, R. Veness, L. Zygaropoulos, O. Stringer, A. Webber-Date, C. P. Welsch, H. Zhang, P. Forck, and S. Udrea, Beam gas curtain monitor: Vacuum studies for lhc integration and operation, Phys. Rev. Accel. Beams **27**, 043201 (2024).

[103] N. Schlossberger, T. McDonald, K. Su, R. Talashila, R. Behary, C. L. Patrick, D. Hammerland, E. E. Mikhailov, S. Aubin, I. Novikova, C. L. Holloway, and N. Prajapati, Two-dimensional imaging of electromagnetic fields via light-sheetfluorescence imaging with rydberg atoms, Opt. Lett. **50**, 7312 (2025).

[104] R. Behary, K. Su, N. DeStefano, M. Vorobiov, T. Averett, A. Camsonne, S. Zhang, C. T. Fancher, N. Malvania, E. E. Mikhailov, S. Aubin, and I. Novikova, Electron beam characterization via quantum coherent electric field imaging, Phys. Rev. Res. **7**, L042042 (2025).

[105] E. Wagenaars, G. M. W. Kroesen, and M. D. Bowden, Investigations of stark effects in xenon rydberg states by laser-induced fluorescence-dip spectroscopy, Phys. Rev. A **74**, 033409 (2006).

[106] E. V. Barnat and G. A. Hebner, Electric fields in a sheath near a metal–dielectric interface, Applied Physics Letters **85**, 3393 (2004).

[107] U. Czarnetzki, D. Luggenhölscher, and H. Döbele, Space and time resolved electric field measurements inhelium and hydrogen rf-discharges, Plasma Sources Science and Technology **8**, 230 (1999).

[108] A. K. Mohapatra, T. R. Jackson, and C. S. Adams, Coherent optical detection of highly excited rydberg states using electromagnetically induced transparency, Phys. Rev. Lett. **98**, 113003 (2007).

[109] L. Ma, E. Paradis, and G. Raithel, Dc electric fields in electrode-free glass vapor cell by photoillumination, Opt. Express **28**, 3676 (2020).

[110] N. Schlossberger, R. Talashila, N. Prajapati, and C. L. Holloway, Angle-of-arrival detection of radio-frequency waves via rydberg-atom fluorescence imaging of standing waves in a glass vapor cell, Phys. Rev. Appl. **24**, 024056 (2025).

[111] A. G. Marshall and F. R. Verdun, *Fourier transforms in NMR, optical, and mass spectrometry, a user's handbook* (Elsevier, 1990).

[112] E. E. Mikhailov, I. Novikova, M. D. Havey, and F. A. Narducci, Magnetic field imaging with atomic rb vapor, Opt. Lett. **34**, 3529 (2009).

[113] S. Mordjick, I. Novikova, E. Mikhailov, and S. Aubin, Optical quantum sensing diagnostic development for non-invasive measurements of electric and magnetic fields in plasmas (2024), DOE BRN Workshop on Measurement Innovation, Washington, D.C., Jan. 9, 2024.

[114] A. Kawasaki, Tracking a nonrelativistic charge with an array of rydberg atoms, Phys. Rev. Res. **5**, 043178 (2023).

[115] R. Behary, K. Su, N. DeStefano, J. Tsai, T. Averett, A. Camsonne, S. Zhang, C. T. Fancher, N. Malvania, S. Aubin, E. E. Mikhailov, and I. Novikova, Electron beam

profiling via rydberg electromagnetically induced transparency in rubidium vapor with crossed laser beams (2026), arXiv:2601.02549 [physics.atom-ph] .

[116] S. L. Brunton and J. N. Kutz, *Data-driven science and engineering: Machine learning, dynamical systems, and control* (Cambridge University Press, 2022).

[117] V. I. Yudin, A. V. Taichenachev, Y. O. Dudin, V. L. Velichansky, A. S. Zibrov, and S. A. Zibrov, Vector magnetometry based on electromagnetically induced transparency in linearly polarized light, Phys. Rev. A **82**, 033807 (2010).

[118] M. G. Maldonado, O. Rollins, A. Toyryla, J. A. McKelvy, A. Matsko, I. Fan, Y. Li, Y.-J. Wang, J. Kitching, I. Novikova, and E. E. Mikhailov, Sensitivity of a vector atomic magnetometer based on electromagnetically induced transparency, Opt. Express **32**, 25062 (2024).

[119] Y. Chen, C. Yuen, D. Arumugam, C. M. S. See, M. Debbah, and L. Hanzo, Polarization-aware doa detection relying on a single rydberg atomic receiver (2025), arXiv:2508.17179 [cs.IT] .

[120] R. Behary, W. Torg, M. Vorobiov, N. DeStefano, A. Vernon, C. T. Fancher, N. Malvania, E. E. Mikhailov, S. Aubin, and I. Novikova, Static dc electric field orientation effects on two-photon rydberg eit (2026), arXiv:2601.09676 [physics.atom-ph] .

[121] M. Vorobiov, R. Behary, W. Torg, N. DeStefano, S. Mordijck, E. T. Jr., S. C. Thakur, C. T. Fancher, N. Malvania, S. Aubin, E. E. Mikhailov, and I. Novikova, Non-perturbative 2d spatial measurements of electric fields within a plasma sheath (2025), arXiv:2511.12322 [physics.plasm-ph] .

[122] V. P. Gavrilenko, H. J. Kim, T. Ikutake, J. B. Kim, M. D. Bowden, and K. Muraoka, Method to measure the electric field vector in an argon glow discharge using laser polarization spectroscopy, Phys. Rev. E **63**, 047401 (2001).

[123] B. Dash, X. Xiang, D. Feng, E. Paradis, and G. Raithel, Electric field diagnostics in a continuous rf plasma using rydberg-eit (2025), arXiv:2512.16867 [physics.atom-ph] .

[124] N. F. Ramsey, A molecular beam resonance method with separated oscillating fields, Phys. Rev. **78**, 695 (1950).

[125] T. Zanon, S. Guerandel, E. de Clercq, D. Holleville, N. Dimarcq, and A. Clairon, High contrast ramsey fringes with coherent-population-trapping pulses in a double lambda atomic system, Phys. Rev. Lett. **94**, 193002 (2005).

[126] M. Abdel Hafiz, G. Coget, P. Yun, S. Guérandel, E. de Clercq, and R. Boudot, A high-performance Raman-Ramsey Cs vapor cell atomic clock, Journal of Applied Physics **121**, 10.1063/1.4977955 (2017), 104903.

[127] R. M. Jenkins, E. E. Mikhailov, and I. Novikova, Transit ramsey eit resonances in a rb vacuum cell, J. Opt. Soc. Am. B **36**, 890 (2019).

[128] R. Behary, A. Gill, A. Buikema, E. E. Mikhailov, and I. Novikova, Rydberg-raman-ramsey resonances in atomic vapor, Phys. Rev. A **109**, 053706 (2024).

[129] G. Pati, D. Mechael, F. K. Fatemi, and R. Tripathi, Millimeter wave imaging using autler-townes splitting induced fluorescence from rydberg atoms in rubidium vapor (2025), arXiv:2510.11918 [physics.atom-ph] .

[130] M. V. Romalis, J. Wiedemann, S. Zhang, and N. Dural, Vapor cell rydberg atom electrometry with time-separated fields (2024), arXiv:2406.05106 [physics.atom-ph] .

[131] D. A. Steck, Rubidium 87 d line data (2001).